Addis Ababa University
አዲስ አበባ ዩኒቨርሲቲ
SEEK WISDOM, ELEVATE YOUR INTELLECT AND SERVE HUMANITY !

ADDIS ABABA UNIVERSITY
COLLEGE OF NATURAL AND COMPUTATIONAL SCIENCES
SCHOOL OF EARTH SCIENCES

MAPPING EFFECTS OF URBAN BLUE-GREEN LANDSCAPES ON LAND SURFACE TEMPERATURE USING GEO-SPATIAL TECHNIQUES: THE CASE OF ADDIS ABABA, ETHIOPIA

By:
Neway Kifle ID: GSR/3066/2012
Advisor:
Binyam Tesfaw Hailu (Ph.D.)

Addis Ababa, Ethiopia
June, 2021

ADDIS ABABA UNIVERSITY

COLLEGE OF NATURAL AND COMPUTATIONAL SCIENCES

SCHOOL OF EARTH SCIENCES

MAPPING EFFECTS OF URBAN BLUE-GREEN LANDSCAPES ON LAND SURFACE TEMPERATURE USING GEO-SPATIAL TECHNIQUES: THE CASE OF ADDIS ABABA, ETHIOPIA

A THESIS SUBMITTED TO THE SCHOOL OF GRADUATE STUDIES OF ADDIS ABABA UNIVERSITY IN PARTIAL FULFILLMENT OF THE REQUIREMENTS FOR THE DEGREE OF MASTERS OF SCIENCE IN REMOTE SENSING AND GEO-INFORMATICS

By:

Neway Kifle

ID: GSR/3066/2012

Advisor:

Binyam Tesfaw Hailu (Ph.D.)

Addis Ababa, Ethiopia
June, 2021

Addis Ababa University

School of Graduate Studies

Thesis Approval Form

This is to certify the thesis prepared by **Neway Kifle Bekele** entitled "***mapping effects of urban blue-green landscapes on land surface temperature using geo-spatial techniques. The case of Addis Ababa, Ethiopia***" is submitted in partial fulfillment of the requirements for the Degree of Master of Science in Remote Sensing and Geo-informatics compiles with the regulations of the university and meets the accepted standards to originality and quality.

Neway Kifle	_____	_____/_____/_____
Candidate	Signature	Date
Signed by the Examining Committee:		
Dr. Binyam Tesfaw	_____	_____/_____/_____
Adviser	Signature	Date
Dr. Dagnachew Legesse	_____	_____/_____/_____
Examiner	Signature	Date
Dr. Tibebu Kassawmar	_____	_____/_____/_____
Examiner	Signature	Date
Dr. K.V. Suryabhagavan	_____	_____/_____/_____
Chairman	Signature	Date
Dr. Balemwal Atnafu	_____	_____/_____/_____
Head, Department of Earth Sciences	Signature	Date

DECLARATION

I hereby declare that the dissertation entitled "***mapping effects of urban blue-green landscapes on land surface temperature using geo-spatial techniques. The case of Addis Ababa, Ethiopia***" has been carried out by me under the supervision of **Dr. Binyam Tesfaw Hailu**, Assistance professor of Remote Sensing and Geo-Informatics, School of Earth Sciences, Addis Ababa University during the year 2019-2021 as a part of Master of Science programme in Remote Sensing and Geo-informatics. I further declare that this work has not been submitted to any other university or institution for the award of any degree or diploma.

Addis Ababa, Ethiopia

Date: June, 2021

Neway Kifle

Acknowledgments

First and for most, praised be to “Almighty God” for his will and help in the whole part of my life.

I am extremely indebted to my advisor Binyam Tesfaw Hailu (Ph.D.), Assistance Professor of Remote Sensing and Geo-Informatics, School of Earth Sciences, Addis Ababa University for his patient, valuable, constructive, and progressive comments and advice, and criticism throughout this work.

I am also grateful to the Central Statistical Agency (CSA) of Ethiopia for sponsoring me to pursue my post-graduate study in remote sensing and geo-informatics Stream, under the college of natural and computational sciences at Addis Ababa University.

I would like to extend my gratitude to Balemwal Atnafu (Ph.D.), Head, School of Earth Sciences, Addis Ababa University for frequently writing letters of support for various data providers; and the School of Earth Sciences, Addis Ababa University, for letting us access Remote Sensing and GIS Lab facilities.

My heartfelt gratitude further goes to Regional Centre for Mapping of Resources for Development/ Global Monitoring for Environment and Security (RCMRD/GMES), and Africa project for covering my tuition fees, and research costs which helped me for the successful completion of this thesis.

I am also grateful to my friend Gizachew Kabite Wedajo (Ph.D.), Associate Researcher II at Department of Remote Sensing Research and Development, Ethiopian Space Science and Technology Institute for reading and giving feedbacks on earlier drafts of this document; and for all my Remote Sensing and Geo-Informatics stream classmates for their contribution of ideas and encouragement during the study and this research work.

Table of Contents

List of figures

List of Tables

List of Appendices

List of acronyms

AA	Addis Ababa
ASF	Alaska Satellite Facility
ASTER	Advanced Space borne Thermal Emission and Reflection Radiometer
AU	African Union
AVHRR	Advanced Very High-Resolution Radiometer
AZP	Addis Zoo Park
CSA	Central Statistical Agency
DEM	Digital Elevation Model
DNs	Digital Numbers
DOS	Dark Object Subtraction
ECA	Economic Commission for Africa
ENVI	Environment for Visualizing Images
EPRDF	Ethiopian People's Revolutionary Democratic Front
ERDAS	Earth Resource Data Analysis System
ESA	European Space Agency
ESRI	Environmental Systems Research Institute
ETM	Enhanced Thematic Mapper
GBG	Gulelle Botanic Garden
GLC	Green Legacy Campaign
GPS	Global Positioning System
IMW	Improved Mono-Window
ISODATA	Iterative Self Organizing Data Analysis
LRT	Light Rail Transit
LSE	Land Surface Emissivity
LST	Land Surface Temperature
LULC	Land Use/Land Cover
MNDWI	Modified Normalized Difference Water Index

MODIS	Moderate Resolution Imaging Spectro-radiometer
MoWR	Ministry of Water Resource
MRS	Multi-Resolution Segmentation
MTS	Multi-Threshold Segmentation
MWA	Mono-Window Algorithm
NDBI	Normalized Difference Built-up Index
NDVI	Normalized Difference Vegetation Index
NHS	National Health System
NIR	Near Infrared
NMA	National Meteorological Agency
NOAA	National Oceanic and Atmospheric Administration
OBIA	Object-Based Image Analysis
OLI /TIRS/	Operational Land Imager/ Thermal Infrared Sensor
RS and GIS	Remote Sensing and Geographic Information System
SC	Single-Channel
SCP	Semi-automatic Classification Plugin
SDS	Spectral Difference Segmentation
SLC	Scan-Line error Correction
SPOT	Satellite Pour l'Observation de la Terre
SST	Sea Surface Temperature
SWA	Split Window Algorithm
SWIR	Short Wave Infrared
TIR	Thermal Infrared
TM	Thematic Mapper
UHI	Urban Heat Island
UN	United Nations
USGS	United States Geological Survey
WHO	World Health Organization

Abstract

Uncontrolled, unplanned, and unprecedented urbanization characterizes most African cities. Drastic changes in the urban landscape can lead to irreversible changes to the urban thermal environment, including changes in the spatiotemporal pattern of the land surface temperature (LST). Studying these variations will help us take urban climate change mitigation and adaptation measures. This study is intended to map effects of urban blue-green landscapes on LST using geo-spatial techniques in Addis Ababa, Ethiopia from 2006 to 2021. Object-based image analysis (OBIA) method was applied for land use/land cover (LULC) classification using high-resolution imagery from SPOT 5 and Sentinel 2A satellites. Moreover, LST was retrieved from the thermal imageries of Landsat 7 ETM + (band 6) and Landsat 8 TIRS (band 10) using the Mono-Window Algorithm (MWA). Furthermore, linear regression analysis was used to determine the relationship of LST with normalized difference vegetation index (NDVI), normalized difference built-up index (NDBI), and modified normalized difference water index (MNWI). Five major LULC classes were identified namely, built-up, vegetation, urban farmland, bare land, and water. The result shows that the built-up area was the most dominant LULC in the city and has shown a drastic expanding trend with an annual growth rate of 4.4% at the expense of urban farmland, vegetation, and bare land in the last 15 years. The findings demonstrated 53.7% of urban farmland, 48.1% of vegetation, and 59.4% of bare land, was transformed into a built-up class from 2006 to 2021. The mean LST showed an increasing trend, from 25.8^{o}C in 2006 to 27.2^{o}C and 28.2^{o}C during 2016 and 2021 respectively. It was found that LST varied among LULC classes. The highest mean LST was observed at bare land having an average LST value of 26.9^{o}C, 28.7^{o}C, and 30.1^{o}C in 2006, 2016, and 2021 respectively. While the lowest mean LST was recorded at vegetation with average LST values of 24.3^{o}C in 2006 and 26.0^{o}C in 2021; and at water 25.5^{o}C in 2016. The regression analysis showed a strong negative correlation between NDVI and LST, a strong positive correlation between NDBI and LST, and a weak negative correlation between MNDWI and LST. The findings of this study have indicated that LULC alteration had contributed to the modification of LST in Addis Ababa during the period. The regression analysis results further revealed that built-up area and vegetation cover plays a decisive role in the variation of LST in the city compared to urban surface water and altitude. The findings of this study will be helpful for urban planners and decision-makers while planning and designing future urban blue-green innervations in the city.

Keywords: LULC, OBIA, LST, NDVI, NDBI, MNDWI

CHAPTER ONE

1. INTRODUCTION

1.1 Background

Urban blue-green landscapes, referring to all green and blue areas in the city (e.g., parks, private gardens, rivers, ponds, and riverbanks) and the ecological services they provide, such as clean water and air, food, fuel, hazards mitigation, and offers a favorable condition for human life (Lise et al, 2017; UN-HABITAT, 2017). These landscapes include either water (blue), vegetation (green), or both.

Urban blue-green landscapes are important for urban climate change mitigation and adaptation measures and have a host of wider benefits to people and wildlife. As one of the urban landscape elements, the green landscape is close to the natural environment in cities. It provides sunshade with various forms of efficiency such as reducing the temperature, humidifying the air, improving the partial microclimate, and hence positively affects the life quality of urban residents. Several studies had indicated the eco-environmental advantages of urban green landscapes mainly in releasing oxygen, consuming carbon dioxide, reducing the air and land surface temperature, lowering noise level, rising air moisture, and lowering dust concentration. Moreover, urban green landscapes protect biodiversity and lower air pollution through the process of photosynthesis, transpiration and evapotranspiration, absorption, and buffer function. Urban green landscapes are one of the best ways to improve the urban thermal environment (Su et. al, 2011). The presence of green landscapes in cities can reduce depression, enhance physical fitness, and improve the health and wellbeing of urban dwellers (University of Leeds, 2015). Likewise, urban blue landscapes have also a great potential to mitigate the urban surface heat island effect (Wu et al., 2019).

The pressure on urban blue-green landscapes will most likely increase with the growing urbanization. Fifty-four percent of the world's population were residing in urban areas in 2014 and it is estimated to reach 70 percent by 2050. Forecasts indicated that expansion of urbanization together with the world's overall population growth will possibly add additional 2.5 billion people to urban settings by 2050. Much of the world's urban population growth is expected to take place in countries of developing regions, particularly Africa (UN, 2014).

LULC dynamics intensified by natural and anthropogenic processes drive biogeochemistry of the ecology affecting the climate at regional as well as global levels. Radical changes in the LULC specifically, the shrinkage in water bodies and vegetation cover due to human activities increases the heat emission from atmospheric and land surface temperatures. Higher LST is predominantly because of an increase in concentrated anthropogenic activities, paved surfaces, or barren lands (Setturu et al., 2014).

Remote sensing particularly, thermal remote sensing is very significant in monitoring LST and studying the thermal properties of LULC types along with their relationships (Abel Balew and Tesfaye Korme, 2020). The basic idea is to retrieve LST from the thermal bands of satellite images and determine its relationship with LULC classes. This method helps to overcome the weaknesses associated with conventional methods by providing better spatial coverage and synchronicity (Naeem et al., 2018).

Plenty of related earlier studies had demonstrated a few approaches to determine the relationship between LST and urban green landscapes in the city. A few of them include: (i) examine the rate and extent of urban expansion in Addis Ababa and determine the urban heat island effect from 1994 to 2011 (Ermias Teferi and Hiwot Abreha,2017); (ii) assess the cooling effect of parks in mitigating urban heat island effect (UHI) in Addis Ababa from 1985 to 2015 (Samson Warkaye. et al., 2018); (iii) examine the pace, extent, and pattern of urbanization and its impact on green spaces in Bole sub-city of Addis Ababa from 1986 to 2000 (Mathias Tesfaye and Tebarek Lika, 2017) and (iv) a comparative analysis to determine the relationship between LST and the composition, configuration and spatial patterns of impervious surfaces and green spaces in Addis Ababa (Ethiopia), Lagos (Nigeria), Lusaka (Zambia) and Nairobi (Kenya), (Simwanda et al., 2019).

Given the small number of earlier studies conducted in the city, their limited spatial and/or temporal scale of analysis and type of methodology employed for LULC analysis (traditional pixel-based method) and materials used (coarse resolution satellite imagery), further studies are needed to develop adequate generalizations that are useful to map effects of urban blue-green landscapes on LST in the city. Moreover, previous researches focused only on vegetation indices to analyze the relationship between LST and land use land cover classes in the city. Furthermore, the potential effect of urban blue landscapes, i.e., urban surface water, on LST is not well understood in the city, although it lowers LST via evaporation (Wu et al., 2019).

1.2 Problem statement

Most African cities are under critical environmental and ecological threat due to uncontrolled unprecedented and unplanned urban expansion. Thus, many of the African cities have emerged as unplanned. As a result, environmental and ecological conditions in African cities are under constant threat (Simwanda and Murayama, 2018). One of the critical environmental threats of urbanization on urban residents is the UHI effect (Simwanda et al., 2019).

This unprecedented city growth is also evident in Addis Ababa and has reduced green landscapes to the level that there is an indication of increasing surface and air temperatures in the city. The problem is expected to get worse in the upcoming years due to the extensive construction of buildings, houses, and infrastructures and the little attention given to urban green landscapes (Mathias Tesfaye and Tebarek Lika, 2017).

In Addis Ababa, the built-up area continues to grow at a rate of 4.5 km^2 per year, at the expense of green landscapes while the remaining ecosystems get ever more polluted. The minimum threshold value of green landscapes per capita as defined by the World Health Organization (WHO) is 9 m^2. However, Addis Ababa scores between 0.4 and 0.9 m^2 per capita which is very poor. (UN-HABITAT, 2017).

A typical characteristic of Addis Ababa and its development is that the successive Ethiopian governments have used new urban projects, new priority areas, and shifting ideologies as material embodiments of political rupture. For instance, Emperor Menelik is known for building the first gravel road, the national palace, the national railway, and the marketplace which are all symbols of modernization. Emperor Menelik was also known for introducing the Eucalyptus tree, one of the most exotic species in Ethiopia. Emperor Haile Selassie's regime constructed an increased number of monuments that honor the Battle of Yekatit 12 and Adwa. The Holy Trinity Cathedral Church and the statue of Lion of Judah were also constructed during Emperor Haile Selassie's regime. The Derg restored Meskel Square for its troop parades and other ceremonial occasions. More recently, the Ethiopian people's revolutionary democratic front (EPRDF) introduced the first light rail transit (LRT) system in Sub-Saharan Africa. The EPRDF also introduced a housing practice called a condominium in the city. Most recently, Prime Minister Abiy Ahmed's administration has announced the Beautifying Sheger (56 km river buffer restoration mega project) and the construction of the 36-hectare luxury real estate complex at Lagahar (Biruk Terrefe, 2020).

The recent administration has also launched a new intervention called the Green Legacy Campaign (GLC) that focuses on green space development in the country in general in the city in particular. Hence, there exists a political shift in ideology and priority areas in the urban development of Addis Ababa.

Launched in 2019 by Ethiopia Prime Minister Abiy Ahmed, the Green Legacy Campaign (GLC) is part of the Government's plan to plant 20 billion seedlings by 2024. According to the World Agroforestry, (2020), Ethiopia planted 4 billion seedlings during the first GLC in 2019 and over 5 billion seedlings during the second GLC in 2020 organized across the country during the Ethiopian rainy season. Addis Ababa City Government River Basins and Green Areas report on July 2020 shows that, in Addis Ababa alone, 7.8 million seedlings are planted during the second GLC covering an area of 8,400 hectares.

The master plan of Addis Ababa city has developed strategies that integrate action plans for the implementation of its various components, more specifically blue-green infrastructure which includes formal parks, gardens, woodlands, rivers, river buffers, street plantations, and walkways. Beautifying Sheger mega project clearly shows the government's focus on blue-green infrastructure and its urgent need. This mega project is expected to raise the green coverage of the city from 0.3 sq.m/per capita to 7 sqm/per capita (Biruk Terrefe, 2020).

Immediately before the recent green interventions, there have been some attempts to develop green spaces in the city. For example, 30.5 hectares of green space is developed at the Nations and Nationalities square in the Nifas Silk-Lafto sub-city. Behind St. Estifanos church in Kirkos sub-city, 5.2 ha of the recreational park is developed. In the Lideta urban renewal site, 4.3 ha of recreational parks and 0.7 ha of recreational green space close to the Immigration office were developed in the Lideta sub-city (Herslund et al., 2017).

Therefore, this study is intended to map effects of urban blue-green landscapes on land surface temperature using geo-spatial techniques in Addis Ababa city of Ethiopia. This city is selected based on the following criteria: (i) because of the government's current urban blue-green space interventions: Green Legacy and Beautifying Sheger Project; (ii) being the capital and largest city in the country; (iii) being the main economic and commercial center of the country; and (iv) experiencing rapid urbanization with the highest urban population than other cities in the country.

1.3 Objectives of the study

1.3.1 Main objective

The main objective of this study is to map effects of urban blue-green landscapes on land surface temperature using geo-spatial techniques in the city of Addis Ababa, Ethiopia.

1.3.2 Specific objectives

- To estimate LST for Addis Ababa during the years 2006, 2016, and 2021;
- To map LULC using Object-Based Image Analysis (OBIA) and high-resolution images for the city of Addis Ababa;
- To analyze the spatiotemporal pattern of LST and its variation among land cover classes;
- To study the relationship of LST with vegetation, built-up, and water indices and altitude.

1.4 Research questions

In line with the research objectives, the study has the following research questions:

- What is the LST of the study area during the years 2006, 2016, and 2021?
- Were there any major changes in the LULC classes within the study period?
- What are the spatiotemporal patterns of LST and its variation among LULC classes of the study area?
- What is the correlation of LST with the land-use class indices (vegetation, built-up, and water) and altitude?

1.5 Significance of the study

The study results include maps showing the spatiotemporal variations of LST, LULC, NDVI, NDBI, and MNDWI in the city for the years 2006, 2016, and 2021. The result of this study also provides quantitative information on LULC dynamics and LST in the study period. Therefore, it is hoped that the study will serves as a benchmark for policymakers and urban planners to ensure accessible and adequate urban-blue green landscapes and implement sustainable LST mitigation strategies and create a conducive living environment in the rapidly urbanizing city of Addis Ababa and beyond. Moreover, the results of this study will be used as initial input for interested groups who will conduct future related studies in the area. It will also offer a better foundation on how remote sensing and GIS technologies are applied in evaluating the urban-blue green landscape effect on LST.

1.6 Delimitation of the study

The scope of this study is spatially delimited only to the administrative boundary of Addis Ababa city, Ethiopia. In its temporal extent, the study is limited in investigating the urban blue-green landscape effect on land surface temperature change using geospatial data for the last 15 years in the city. The years 2006, 2016, and 2021 are selected to analyze the spatiotemporal pattern of urban-blue green landscapes and their effect on LST. Moreover, theoretically, this study is restricted in studying the spatiotemporal pattern of LULC dynamics and the resulting change in LST, even though other factors are also affecting LST in the city.

1.7 Organization of the thesis

This thesis paper is organized into six chapters. Chapter one is devoted to the introductory part of the paper where the background of the study, statement of the problem, objectives of the study, research questions, significance, and delimitation of the study were described. A review of related literature is treated under chapter two. The third chapter deals with the study area description, the materials used and methods utilized in this study. In chapter four, results are presented and analyzed. The results are discussed in chapter five. Finally, chapter six provides conclusions drawn and the forwarded recommendations.

CHAPTER TWO

2. LITERATURE REVIEW

2.1 Urban green landscapes

Urban green landscape in the context of urban studies refers to several terms and definitions that include green space, open space, urban greenery, public gardens, green infrastructure, public space, and parks. Urban designers and planners, architects, landscape architects, and other professionals have used these terms interchangeably. Moreover, it can be discussed from different points of view such as design, policy, planning, management, and environmental psychology, and so on (Rakhshandehroo et al., 2017).

Urban Green landscapes refer to those LULC that are covered with man-made or natural vegetation in urban and other planning areas (Bilgili and Gökyer, 2012). These range from green on buildings such as green roofs, balconies, and green walls; to green near built structures, such as street median and side greening, railway banks, public square, playgrounds, house gardens, different types of parks, cemeteries, institutional green spaces, sports facilities, and community gardens and allotments; to more open kinds of green spaces like horticulture and farmland, shrublands and woodlands (Roy et al., 2012; Pauleit et al., 2017).

2.1.1 Benefits of urban green landscapes

Bilgili and Gökyer, (2012) reported that urban green landscapes have many health, ecological, economic, social, and aesthetic related benefits and functions which are vital to improving the quality of life in the cities. These areas can serve as a bridge between nature and people (who live in urban areas). Therefore, these areas are very important for the urban people and maintaining the ecological functions of the environment.

Ecological benefits

One of the crucial benefits of urban green landscapes is the ecological and environmental functions they provide. They can reduce environmental-related health risks associated with urban living by improving air and water quality, mitigating impacts from extreme events, and buffering noise pollution (WHO, 2017). Likewise, numerous studies have shown that urban green landscapes help in mitigating the urban heat island effect in urban areas, thereby decreasing the energy costs of cooling buildings. Urban green landscapes lower noise, air, and water pollution, and may balance greenhouse gas emissions through CO2 absorption. The urban green landscape also provides

stormwater attenuation, thereby acting as a measure for flood mitigation (Pataki et al., 2010; Young and Robert, 2010; Roy et al., 2012; Lee et al., 2015). Additional ecological benefits include a vital role they play in providing shelter for the natural life corridors and urban forests they create. Thus, urban green areas ensure the continuity of the species and the city's biodiversity by creating a habitat for the existence of natural plants and animals (Dunnett et al., 2002; De La Barrera et al., 2016).

Health benefits

From the viewpoint of health, urban green landscapes have health, physical, and psychological benefits through physical activities and green exercises. Walk-able green areas influence the longevity of urban senior citizens. Higher levels of greenness in urban areas have been positively related to reduced stroke mortality. Besides, it improves recovery times after periods of ill health. Moreover, it is also associated with a lower likelihood of being obese or overweight (Jose et al., 2018).

Economic and aesthetic benefits

From the viewpoint of the economy, numerous studies have reported that urban green landscapes have economic and aesthetic benefits. For instance, Arvanitidis et al., (2009) and Saraev and Vadim, (2012) reported good quality green landscapes can increase value to the nearby property, both residential and commercial. Consequently, helps to create a favorable image for a place, increase tax returns to local authorities, attract tourism and inward investment in the area encouraging employment, boost retail sales, and even exert pull-on skilled labor. Using green landscapes has been increasingly recognized as a cost-effective way of reducing the energy costs of cooling buildings in cities. Parts of the urban areas with adequate green landscapes are attractive and aesthetically pleasing to the urban dwellers, tourists, and investors (Haq, 2011).

Social benefits

From the viewpoint of social benefit as a whole, green landscapes reduce the burden on the National Health System (NHS) and absenteeism from work due to ill health by improving the health of the population (Jennings et al., 2019). People visit urban green landscapes mostly for enjoying various environmental elements such as fresh air, watching cascades, nature, flowers, trees, wildlife, passive walking, taking children to play, educational opportunities, social activities,

picnics, meet friends, social interaction, meeting people, getting away from it all, and sitting. Other reasons people visit urban green landscapes include walking a dog, hanging out, sitting either on grass or seats, watching sport, walking socially as part of a group, smoking, passive enjoyment, watching life go, photography, messing about on swings, readings, sunbathing, an informal pursuit such as flying kites, etc. (Jose et al., 2018).

2.1.2 Urban green landscapes as a foe

It is helpful to understand that few studies have reported that urban green landscapes can also negatively affect human populations. Concerning this, three major kinds of harm have been documented.

First, allergic reactions and pollen can damage human health, infectious disease spread, and accidental injury during outdoor green exercise or recreation. Second, green landscapes have been used to add the surrounding property values, but this can lead to a process called environmental gentrification where unlivable circumstances are created for communities with lower socioeconomic status (Jennings et al., 2019). Third, other likely harmful effects of urban green landscapes are related to fear of crime and animals (Snakes, insects, bats, rodents), disgust from plant litter or blocked views, and psychological effects caused by trees and animals (behavior, sound, smell) (Calaza et al., 2017).

2.1.3 Classification of urban green landscapes

There are several ways of classifying urban green landscapes such as based on their size, their intended purpose, their location, and usage, etc. (Byrne and Sipe, 2010). According to Forest Research, (2021) urban green landscapes include; urban parks, green areas around buildings, gardens, wetlands, green roofs, street trees, and community woodlands. Likewise, Swanwick et al., (2003) classified green landscapes based on the intended function of each green space in terms of the kind of services provided, its size and the extent of its catchment area, and the nature of the resource. These types of urban green landscapes include productive green (urban farmlands), incidental green space (housing green space), recreation green (e.g., parks), burial grounds (cemetery and churchyards), institutional green (e.g. school grounds), private garden (domestic garden), wetlands and woodlands and linear green areas like transport corridors (cycleways, rail, road, and walking route). Similarly, Panduro and Veie, (2013) identified the green landscapes in the city of Aalborg, Northern Denmark based on the quality and quantity of facilities offered by

lakes, parks, churchyards, common areas (shared green space), agriculture fields sports fields, nature, and green buffers.

2.1.4 An Overview of urban green landscapes in Addis Ababa

Identification of green landscape categories could vary based on the purpose of classification. Accordingly, different cities have used different green landscape classifications. Kumelachew Yeshitela et al, (2015) categorized the green landscapes in Addis Ababa into plantation forest, institutional forest, public recreational parks, special function parks, private gardens, street plantation, field crop, vegetable farm, grassland, and riverside vegetation.

Plantation forest: this type of vegetation is mainly found in the Northern part of Addis Ababa, particularly, on Entoto mountain. *The eucalyptus* tree is the dominant species in plantation forests. However, in some parts of the plantation forest pure stands of *Cupressus lusitanica* and *Pinus patula* are also found.

Figure 2. 1: *Picture of plantation forest on Mt. Entoto*

Source: *(Walta TV, 2020)*

Special function parks: These are green landscapes mainly established for the conservation of plant species, education, and research. However, they also provide recreational services to the public. One good example of special function parks is the Gulelle Botanic Garden (GBG) which lands on 705 hectares of land. The Addis Zoo Park (AZP), formerly called central (peacock) park also falls into this category. AZP was previously used for providing recreational and social services but is currently developed into a zoological park for the conservation of wild animals.

Institutional forest: are forests that are found inside the governmental and non-governmental institution compounds**.** Institutional forests in the city include a mixture of exotic and indigenous trees and shrubs. These forests are largely found within the compounds of USA, French, British, Italy, and German embassies, the various campus of Addis Ababa University, within the Ethiopian Orthodox Tewahedo church compound, and the grand and national palaces of Ethiopia.

Figure 2. 2: *Picture of institutional forest in the old national palace*

Source: *(Walta TV, 2020)*

Public parks: these are designed, built, and enclosed green landscapes mainly used for recreational and social services such as wedding and birthday ceremonies and other public gatherings. These categories of green landscapes include both shrubs and trees. Currently, there are nearly 20 recreational parks in Addis Ababa, including the recently built Friendship Square/Park and Unity Park.

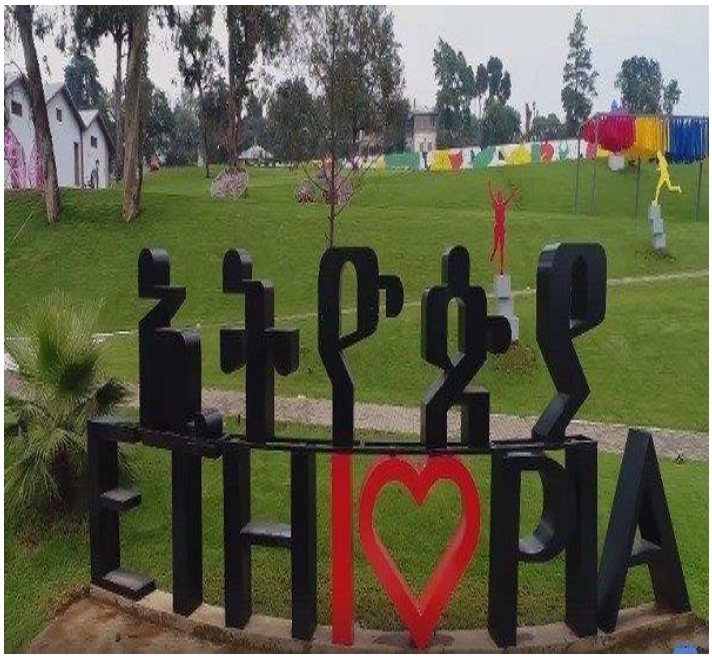

Figure 2. 3: *Picture Unity Park found in the National palace*

Source: *(Walta TV, 2020)*

Private gardens: These are small-sized green landscapes found within the compounds of privately owned houses and offices kept for private uses. This category constitutes vegetables, ornamental, and fruit trees. They are mainly established for providing vegetables, fruits, and aesthetic service. They also provide shading to houses and serve as stormwater infiltration by returning water to the atmosphere via evapotranspiration.

Street trees: These are trees planted along road divides, street sides/pedestrian roads, and public squares mainly for aesthetic values/beautification. Street trees play a crucial role by releasing oxygen, consuming carbon dioxide, providing shade to vehicles and pedestrians, reducing air pollution, and increasing the beauty of the streetscape. Moreover, they lower erosion and stormwater management costs by reducing the intensity and amount and of precipitation striking the ground.

Field crop: These are crops grown based on rain-fed urban agriculture. The land covered with this crop appears green during the rainy season that runs from June to September. The crops are usually harvested during November and December, therefore, the land remains bare till the next crop season. During the dry season, the land is mainly used for keeping livestock. The common field crops grown in the city include Wheat (*Triticum aestivum*), Tef (*Eragrostis tef*), and Barley (*Hordeum vulgare*).

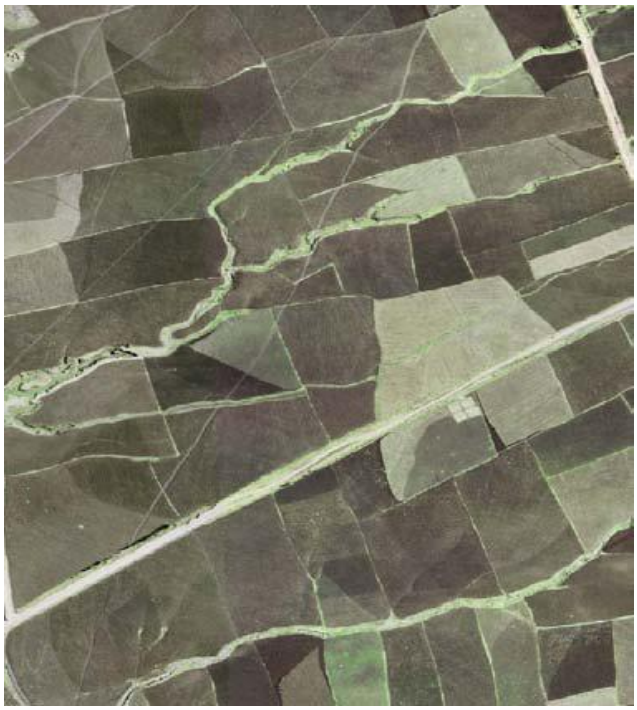

Figure 2. 4: *Field cropland in Addis Ababa*

Source: *(Kumelachew Yeshitela et al, 2015, pp. 11)*

Grassland: This category includes green areas mainly covered with grasses which are located within the compounds of the church, airport, military, and golf field. Grasses appear to be bare land during the dry season changing the morphology of the landscape.

Riparian vegetation. Addis Ababa is endowed with several streams and rivers. These rivers originate from the Northwest, North, and Northeastern parts of the city draining the city southward, and finally joins the Awash River. The major rivers that drain the city include Kebena, Great Akaki, Kechene, Little Akakai, Ginfile, Jemo, Bantiketu, etc. There is no documented information on the plant species composition of the riparian vegetation. However, various types of vegetation grow along the river banks of the city.

Vegetable farms: Are found in parts of the city where vegetables are grown using irrigation from the nearby rivers. The main vegetables planted in Addis Ababa include onion (*Allium cepa*), garlic (*Allium sativum*), tomato (*Lycopersicon esculentum),* cabbage (*Brassica oleravea*), lettuce (*Lactuca sativa*), and carrot (*Daucus carota*).

2.2 Urban blue landscapes

Blue spaces consider all the hydrographic features including lakes, ice masses, ponds, estuaries, playas, reservoirs, and swamps and marshes or a linear surface water drainage network such as streams, rivers coastlines, canals, and ditches) (Haeffner et al., 2017). The term "urban blue landscapes" refers to the flowing open surfaces water courses and standing water bodies such as lakes, reservoirs, streams, rivers, and ponds, etc. located within urban areas (Gunawardena et al., 2017; Radek and Renata, 2019). Several scholars have claimed that blue landscapes provide very different sensory experiences and are used in different ways with different outcomes and benefits that are often overlooked and remain poorly understood. However, it is evident that there exists an overlap between the green and blue landscapes (Haeffner et al., 2017; Easkey et al., 2020)

2.2.1 Benefits of urban blue landscapes

The widely acknowledged ecological benefits provided by urban blue landscapes include oxygen production, noise reduction, microclimate regulation, and carbon sequestration. Moreover, the blue spaces are used for recreation and social interaction purposes like physical exercise, sport, etc. People also visit urban blue landscapes for recreational reasons like watching various types of wild animals (e.g., fish, ducks) (Haeffner *et al.*, 2017). Furthermore, a recent study has reported that walking along or in blue spaces gives additional benefits for the mental health and well-being of people by decreasing anger, tension, depression, and improving restoration time (Vert et al., 2020).

However, water bodies in urban areas are not always considered with a positive attitude only. Ponds, rivers streams, and canals in urban areas can attract rubbish resulting in an unattractive

looking. There are also dangers from either the water itself (e.g., flooding) or associated potential waterborne disease (e.g. malaria) at least during the life cycle of mosquitoes (Gledhill and James, 2008).

2.3 Land use land cover change

Land cover is defined as the physical and biological cover over the land surface, including vegetation, water, bare soil, and/or man-made structures. On the other hand, land use refers to activities on the land or classification of land according to how it is being used, such as residential, industrial, commercial, agricultural, recreational, etc. Hence, both land use land cover is directly related to the activities of humans in their environment. Unlike land-use, land-cover information can be obtained from remote sensing. The land cover properties detected using remote sensing techniques concerning land use can be inferred, particularly with ancillary data or prior knowledge (Bhatta, 2011). Land-use change refers to a change in the way a certain area of land is being managed or used by humans, whereas, land cover change means an alteration in a given continuous property of the land like soil properties, vegetation type, etc. (Patel et al., 2019).

2.4 Remote sensing and GIS for urban land use land cover change

The method of detecting and monitoring the physical features of an area by measuring it's reflected and emitted radiation from a distance, such as from a satellite, drone, or airplane, is known as remote sensing (RS) (USGS, 2021). Whereas, GIS is an integrated system of computer software and hardware for capturing, storing, retrieving, manipulating, analyzing, and displaying geographically referenced or spatial information to aid development-oriented management and decision-making processes (Aboyade, 2001).

Improvements in remote-sensing data have enhanced spatial accuracy and availability of free to less-expensive satellite imageries. Geographic information system (GIS), combined with RS allows quantitative analyses of the pattern and rate of urban LULC dynamics with better accuracy and reasonable cost (Epstein et al., 2002). One of the advantages of RS data for earth observation applications is its wide-area coverage (synoptic view) and studying of areas hard to reach. Moreover, RS data is usually actual, timely, and temporal, or repetitive. High spatial resolution is also essential for LULC studies as the sensor may detect data on more diversified LULC types. Another advantage of remote sensing is its long-lasting records of data for more than 40 years of observations by now (Bobrinskaya, 2012).

GIS creates a flexible environment for storing, displaying, and analyzing digital spatial data needed for detecting urban LULC dynamics (Wu et al., 2006). RS imagery is the most important data input of GIS (Reis, 2008). Accordingly, RS imageries can serve as a source of data for monitoring and extraction of LULC types and their dynamics over different periods that occur in urban settings. Integrating GIS with the digital image classification has proved its capability to analyze a wide range of information about the rate, nature, direction, and location of urban land expansion and its consequential LST rise. Thus, the integration of RS and GIS was found to be effective in analyzing and monitoring the rate, extent, and patterns of urban growth and its impact on LST (Matiwos Belayhun, 2018).

2.5 Image classification

Image classification is the process of categorizing and labeling individual/groups of pixels or image objects within an image based on specific rules (Shinozuka and Mansouri, 2009). The principal aim of image classification is to categorize and assign all the pixels of a particular image into a proper land-cover class. Nowadays, there are numerous techniques for classifying satellite images. These classification techniques can be grouped into pixel-based (Supervised, unsupervised, and hybrid classification) and object-based image classification (Gašparović, 2020).

2.5.1 Supervised image classification

In supervised classification, the process of pixel categorization is governed by the image analyst who sets numerical descriptors of the different land cover types found in the image scene to the computer algorithm. To perform this, training areas that represent sample sites of known land cover types are used to compile a numerical "interpretation key" that defines the spectral characteristics for each land cover category. Every single pixel in the image scene is then compared numerically against each land cover class in the interpretation key and finally assigned to the name of the land cover class that it "looks most like" (Lillesand et al., 2015). Currently, there are several supervised image classification techniques. It should be noted that traditional methods used in nowadays research include Maximum Likelihood, Minimum Distance, as well as, contemporary machine learning-based methods like Random Forest Artificial, Neural Network, and Support Vector Machines (Gašparović, 2020).

Previous knowledge of the dataset is essentially needed for testing and training of classifiers in supervised classification. The analyst collects training samples based on prior knowledge of the

dataset. One important advantage of these classification techniques is detecting classification errors and correcting them. Another advantage of such techniques is that, after completing the classification process, they represent the actual land-cover features, i.e., the training samples based on which the classification is carried out. The main disadvantage of these techniques is that it is costly and time-taking. Moreover, the analysts or scientists may not consider all situations and land-cover classes during the selection of training samples. Thus, these techniques may lead to human errors during classification (Borra et al., 2019).

2.5.2 Unsupervised image classification

The unsupervised classification does not need prior knowledge of the area and training samples but only requires the number of land cover categories. In this type of classification, the entire satellite image is automatically classified into land cover classes by grouping pixels of similar radiometric characteristics. After classification, the class must be assigned automatically or manually to the proper land-cover category in the real world. The most commonly used researchers are Iterative Self Organizing Data Analysis (ISODATA) and k-means (Gašparović, 2020).

There are three main advantages of applying the unsupervised classification method. First, during the initial separation of image pixels, extensive prior knowledge of the area being classified is not needed. Second, the analyst who makes decisions while classification is not needed, hence human errors are less likely to occur, Third, some unique land cover categories ignored in a supervised classification may be recognized by unsupervised classification. However, there are limitations to the use of such classification methods. For instance, the land cover classes of interest may not necessarily correspond with the natural groupings identified by the classification process which is based on spectrally homogeneous pixels. Moreover, the analyst has limited control over the classes chosen by the classification process (Enderle and Weih, 2005).

2.5.3 Hybrid method

The hybrid method is intended to retain efficiency and/or accuracy and involve aspects of both unsupervised and supervised classification (Lillesand et al., 2015). This technique is primarily applied when one is unable to define well the differences between types of subclasses such as type of material used as roof cover, vegetation type, crop or soil type. Rule-based classification methods fall into hybrid methods. Such methods are based on some rules or conditions, e.g., water is an area where the MNDWI>0 or built-up represents the area where the NDBI>0 (Gašparović, 2020).

2.5.4 Object-based image analysis (OBIA)

In contrast to pixel-based image classification, the object-based or object-oriented classification uses both spectral and spatial information for classification. This method uses texture, color, shape, pattern, size, and context information to categorize pixels into meaningful objects. This makes it similar to the human visual interpretation of digital images, which works at multiple scales simultaneously. OBIA is a two-step process involving (1) segmentation of the imagery into separate image objects, followed by (2) classification of image objects to meaningful classes. The basic idea behind this is that the image being classified consists of relatively similar "patches" that are larger than individual pixels (Lillesand et al., 2015).

The object-based method has advantages that overcome the traditional pixel-based technique in two aspects. First, the so-called salt-and-pepper effects that are common in pixel-based classification are removed as the changes in classification units from pixels to image objects reduce within-class spectral variation. Second, complementary information on the direct spectral observations that improve classification accuracy can be derived from a large set of features characterizing objects such as textural, spatial, and contextual properties (Guoet et al., 2007; Liu and Xia, 2010). On the other hand, Liu and Xia, (2010), reported the potential limitation in using object-based classification is the dependence on segmentation parameters like scale. This may result in under or over-segmentation of image objects. Therefore, segmentation could be carried out with an appropriate scale for better classification accuracy while using object-based methods.

2.5.4.1 Image segmentation

Segmentation is a process that involves the grouping of pixels in an image scene into non-overlapping object segments, or features with homogeneous spatial and spectral properties (Witharana and Civco, 2014). The scale parameter is the main variable that determines the size of image objects during segmentation. To illustrate, in the case of the urban landscape, individual vehicles parked on streets may be better segmented (changed into image objects) at a fine-scale, whereas, buildings might be well segmented with a courser scale. Likewise, in the forest landscape, segmentation at a medium scale can generate image objects that represent trees of the same sizes and species, while segmentation at a coarser scale, could aggregate large areas of the forest into a single image object. Determination of the scale parameter used in OBIA depends on some factors such as the interest of the analyst on the general scale of the objects on the landscape to be identified and the resolution of the sensor (Lillesand et al., 2015).

After image segmentation, there are various image object spectral and spatial characteristics that help to classify or categorize the objects into proper land cover classes. These characteristics are broadly grouped into two types. The first is related to the intrinsic characteristics of each object itself (e.g. its texture, its spectral properties, its shape, its size, etc.). The second characteristics describe the relationships among image objects such as boundary shared with the same or other objects, their proximity to objects of the same or other types, their connectivity, and so forth. For instance, an object having a smooth texture, a linear shape, a similar spectral signature with asphalt, and topologically connected to other road objects would most likely be the road itself (Lillesand et al., 2015).

2.6 Land Surface temperature

Land surface temperature (LST) is how cold or hot the Earth's surface is when touched on a specific location. From the viewpoint of satellites, the Earth's surface is whatever it sees while it looks to the ground, through the atmosphere. It could be the roof of a building, sea surface, snow and ice, the leaves in the canopy of a forest, or the grass on a lawn. Thus, the land surface temperature is not the same as the air temperature that is included in the daily weather report (NASA, 2000).

LST, including also sea surface temperature (SST), is the principal geo–biophysical variable to be estimated from thermal bands of satellite images. Most of the thermal energy directly emitted by the land surface features is remotely detected by the thermal sensors that operate within this spectral region. It is a vital parameter in different disciplines that focuses on environmental studies including meteorology, ecology, climatology, geology, hydrology, oceanography, and so forth (Jimenez-Munoz et al., 2008).

2.7 Land surface temperature response to land use and land cover dynamics

Land use/land cover (LULC) dynamics caused by natural processes or anthropogenic activities drive the biogeochemistry of the Earth affecting the climate both at regional as well as global levels. Radical changes in the land cover combined with the shrinkage in water bodies and vegetation due to human activities increase the heat emission from the land surface and atmospheric temperatures. The higher concentration of human activities, paved land cover, or barren lands mainly leads to increased LST (Setturu et al., 2014). Landscape changes involving LULC dynamics have contributed to the increase in LST. The various land cover classes show the

variability with different land surface temperatures (Weng et al., 2007; Wichansky et al., 2008). Moreover, LULC dynamics influence evaporation rates, the absorption of solar radiation, storage of heat, wind turbulence, land surface temperature, and can considerably change the conditions of the near-surface atmospheric temperature. Furthermore, the key indicators considered to explain the global climate change including land cover/use, clouds, land surface temperature, exchanges of energy, and moisture can vary drastically both temporally and spatially. Thus, it is essential to monitor LULC dynamics at proper scales to mitigate its impacts on changing climate particularly land surface temperature (Setturu et al., 2014).

In Ethiopia, several studies have investigated the temporal and spatial pattern of LST in relation to the changes in LULC classes. For instance, Abel Balew and Tesfaye Korme, (2020) used NDVI and NDBI to analyze the spatial pattern of LST and its variation with different LULC types in Bahir Dar City and its surrounding. Likewise, Matiwos Belayhun, (2018) used NDVI to study its correlation with LST in the city of Dire Dawa, Ethiopia.

It is also evident from the literature that in Ethiopia, particularly Addis Ababa, the urban heat island (UHI) phenomenon and its relation to urban green landscapes has been studied by a few studies (e.g. Mathias Tesfaye and Tebarek Lika, 2016; Samson Workaye et al., 2018; Ermias Teferi and Hiwot Abreha, 2017). However, recently, (Simwanda et al., 2019), focused on the relationship between LST and the composition, spatial patterns, and configuration of impervious surfaces and green landscapes in four African cities, Addis Ababa (Ethiopia), Lagos (Nigeria), Nairobi (Kenya), and Lusaka (Zambia).

2.8 Thermal remote sensing for land surface temperature

Remote sensing, particularly, thermal remote sensing is very important for monitoring LST and analyzing the thermal characteristics of the earth's surface features as well as their relationships. In this regard, LST has been retrieved from low-resolution thermal satellite sensors, for example, Moderate Resolution Imaging Spectroradiometer (MODIS) and NOAA Advanced Very High-Resolution Radiometer (AVHRR). Moreover, LST can also be estimated from medium resolution thermal sensors such as Advanced Spaceborne Thermal Emission and Reflection Radiometer (ASTER), Landsat Thematic Mapper (TM), Enhanced Thematic Mapper Plus (ETM+), and Operational Land Imager (OLI)/ Thermal Infrared Sensor (TIRS) (Abel Balew and Tesfaye Korme, 2020). Thermal data is detected by satellite sensors that operate within the thermal infrared spectral

region. The radiance at the top of the atmosphere is captured by Thermal Infrared (TIR) sensors. However, radiation recorded by the sensor is influenced by atmospheric effects. Therefore, to obtain meaningful values, this row data should be corrected for atmospheric effects and emissivity. This radiometrically corrected temperature can be used to retrieve LST in Celsius degrees or Kelvin (Bobrinskaya, 2012).

2.9 Methods of land surface temperature retrieval

Many applications such as agro climate, meteorology, and environmental studies strongly require knowledge of land surface temperature. Satellite remote sensing in the infrared provides an interesting alternative for the continuous and global records of this parameter. Two main problems arise in using thermal remote sensing data for retrieving LST. These are the land emissivity effect and atmospheric effect. Hence, different algorithms have been developed to correct these two effects (Pozo et al., 1997). There are three major methods of retrieving LST (Wang et al., 2019) that include the Mono-Window Algorithm (MWA), developed by Qin et al., (2010), the Single-Channel (SC) Method, developed by Jimenez-Munoz and Sobrino, (2003), and the Split Window Algorithm (SWA), developed by McMillin, (1975).

2.9.1 Mono-window algorithm (MWA)

Qin's mono-window algorithm is shown in equation (1). MWA requires three parameters. These are land surface emissivity (Ɛ), the effective mean atmospheric temperature (Ta), and atmospheric transmittance (τ). However, equation (1) is proposed for Thematic Mapper (TM) thermal images (Wang et al., 2019).

$$T_s = [a_6 (1 - C_6 - D_6) + (b_6 (1 - C_6 - D_6) + C_6 + D_6) T_6 - D_6 T_a] / C_6 \quad (1)$$

Where;

T_s-LST in K; T_6 is the brightness temperature of Landsat 5 TM Band 6; T_a is the effective mean atmospheric temperature; C_6 and D_6 are the internal parameters for the MWA based on the atmospheric parameters and ground emissivity, and a_6 and b_6 are the coefficients used to approximate the derivative of the Planck radiance function for the thermal band.

Later, Wang et al., (2015) improved the algorithm for retrieving LST from Band 10 of Landsat 8. This improved algorithm is called Improved Mono-Window (IMW) algorithm as is shown in equation (2).

$$T_s = [a_{10}(1 - C_{10} - D_{10}) + (b_{10}(1 - C_{10} - D_{10}) + C_{10} + D_{10})T_{10} - D_{10}T_a] / C_{10} \quad (2)$$

where T_s is the LST estimated from Band 10 of Landsat 8 TIRS image; T_a is the effective mean atmospheric temperature; a_{10} and b_{10} are the constants used to approximate the derivative of the Planck radiance function for the TIRS Band 10; T_{10} is the brightness temperature of Landsat 8 TIRS Band 10; C_{10} and D_{10} are the internal parameters for the algorithm.

2.9.2 Single-channel (SC) method

The single-channel (SC) method was proposed in 2003 by Jiménez-Muñoz and Sobrino, (2003) and improved in 2009 by Jiménez-Muñoz et al., (2009). This algorithm requires only two input parameters, the land surface emissivity, LSE (Ɛ), and the atmospheric water vapor content (ω). Unlike MWA, the SC method does not require the effective mean atmospheric temperature (Ta) parameter, and the atmospheric water vapor content (Wang et al., 2019). The advantage of the SC algorithm is its simplicity. However, the SC algorithm applies to sensors with only one TIR band. Another disadvantage of the SC algorithm is the substantial effects of the uncertainty of atmospheric patterns on the accuracy of LST retrieval (Rongali et al., 2018).

Jiménez-Muoz et al. (2014), updated the SC method for Landsat 8 and calculated the corresponding parameters; the formula for the SC method is provided in equation (3).

$$LST = \gamma \left[\frac{1}{\varepsilon}\left(\psi 1 Lsen + \psi 2\right) + \psi 3\right] + \delta \quad (3)$$

Where; ε is LSE, Lsen is at-sensor registered radiance (W/ (m2·sr·μm)), γ and δ are variables based on the Planck's function given by:

$$\gamma = C2 Lsen Tsen 2 \lambda 4 Lsen C1 + 1 \quad (4)$$

$$\delta = -\gamma Lsen + Tsen \quad (5)$$

Where Tsen is the at-sensor brightness temperature; for band 10 of Landsat 8 and C*1* and *C2* are physical constants (C1=1.191×10^8 Wμm^4 sr^{-1} m^{-2}, C2=1.439×10^4 μm·K) (Käfer et al., 2020).

The three atmospheric function parameters; ψ1 ψ2 and ψ3 are calculated as follows;

$$\psi 1 = -7.2122w2 + 0.00005Ta2 - 2.452321w - 0.026275Ta\ 0.00005Ta2w + 0.02317Taw + 0.04663Taw2 - 0.00007Ta2w2 + 4.47297, \quad (6)$$

$$\psi 2=89.61569w2-0.00038Ta2+106.55093w+0.21578Ta+0.00141Ta2w-0.78444Taw-0.5732Taw2+0.00091Ta2w2-30.37028, \quad (7)$$

$$\psi 3=-14.65955w2-0.0001Ta2-79.95838w+0.04181Ta-0.00091Ta2w+0.54535Taw+0.09114Taw2-0.00014Ta2w2-3.76184. \quad (8)$$

2.9.3 Split window (SW) algorithm

The split window algorithm (SWA) was originally proposed by McMillin, (1975). It is an algorithm for observing the ocean surface temperature based on Advanced Very High-Resolution Radiometer (AVHRR) thermal infrared data. The basic principle behind this algorithm is that two adjacent TIR bands have different absorption properties; the difference between the brightness temperatures of the two TIR bands is used to determine the attenuation information of the atmosphere on thermal radiation. The main advantage of SWA that it is simple to operate and is less dependent on atmospheric parameters (Rongali et al., 2018; Wang et al., 2019). According to Jiménez-Muñoz et al., (2014), the equation to estimate LST using SW algorithm from Landsat 8 TIRS data is:

$$LST = Tisen+1.378(Tisen-Tjsen)+0.183(Tisen-Tjsen)2-0.268+(54.3-2.238w)(1-\varepsilon)+(-129.2+16.4w)\Delta\varepsilon \quad (9)$$

Where;

Ti_{sen} is at-sensor brightness temperatures for bands i (band 10) in Kelvins,

Tj_{sen} is at-sensor brightness temperatures for band j (band 11) in Kelvins,

ε is the mean emissivity, $\varepsilon = 0.5(\varepsilon i + \varepsilon j)$,

$\Delta\varepsilon$ is the emissivity difference, $\Delta\varepsilon = (\varepsilon i - \varepsilon j)$, and

w is the total atmospheric vapor content (in $g \cdot cm^{-2}$).

CHAPTER THREE

3. STUDY AREA, MATERIALS, AND METHODS

3.1 Study area description

3.1.1 Location

Addis Ababa is Ethiopia's capital and largest city. Addis Abba means "New Flower" in Amharic. It is the headquarters of the African Union (AU) and the United Nations Economic Commission for Africa (ECA). Hence, Addis Ababa is frequently referred to as Africa's "political capital." The city is sub-divided into 10 sub-cities: Akaki-Kalty, Arada, Bole, Lideta, Gulele, Kirkos, Kolfe, Nifas silk lafto, and yeka. The ten sub-cities are further divided into 116 woredas. The city is located in the central highlands of Ethiopia and is in-circled by mountain ridges of Entoto in the North, Wochecha in the West, Furi in the South West, and Yerer in the North East. In absolute terms, Addis Ababa lies between 38° 39′2.76′′ to 38° 54′19.4′′ East Longitude and 8° 50′13.06′′ to 9° 6′4.62′′ North Latitude covering a total area of 527 square kilometers (See Figure 3.1).

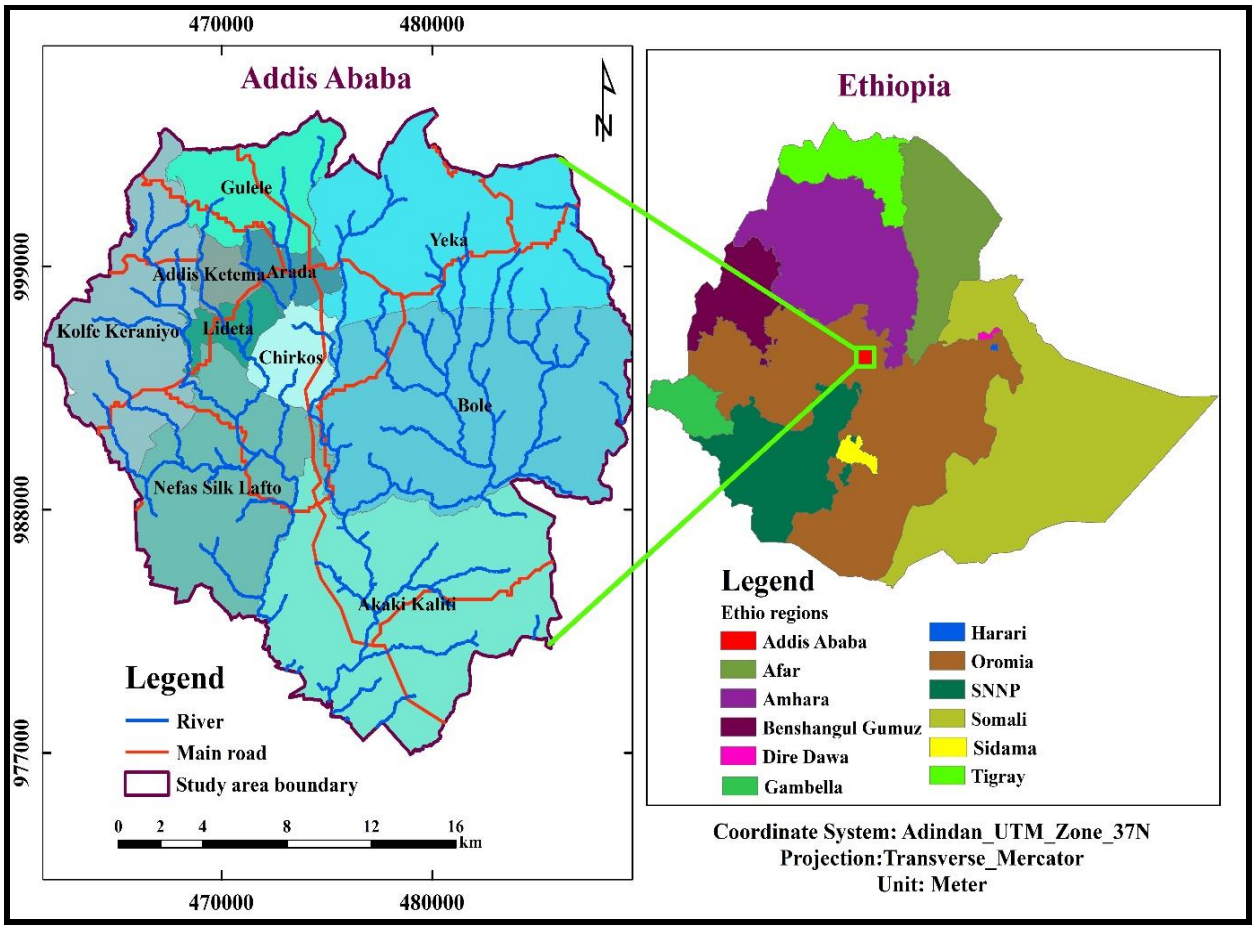

Figure 3. 1: *Location map*

3.1.2 Basic population characteristics

According to CSA, (July 2017) population estimation, Addis Ababa has a total human population of 3,433,999 with a population density of 6518 persons per square kilometers. The sex composition of the city reveals that 1,809,999 (47.3%) are males and the rest 1,809,000 (52.7%) are females. Whereas, the sex ratio indicates that there are 90 males for every 100 females in the city (Table 3.1). The 2007 Ethiopian population and housing census show that the city has an average household size of 4.1 and an annual population growth rate of 2.1. The major ethnic groups residing in the city include Amhara (47.1%), Oromo (19.5%), and Guragae (16.3%). The religious composition of the city shows that 74.7 % Orthodox Christians, 16.2 % Muslims and 7.8% Protestants (CSA, 2007).

Table 3. 1: *Addis Ababa population by sub-city, sex composition, sex ratio, and population density*

Sub-city	Male Population	Female Population	Total Population	Population Density	Sex Ratio
Addis Ketema	155,478	164,575	320,053	43,250	94
Akaki-Kaliti	110,435	116,747	227,182	1,924	95
Arada	123,445	141,696	265,141	26,755	87
Bole	180,782	206,573	387,355	3,212	88
Gulele	161,078	174,356	335,434	11,144	92
Kirkos	128,841	148,505	277,346	18,970	87
Kolfe-Keraniyo	258,480	279,081	537,561	8,777	93
Lideta	119,843	132,999	252,842	27,573	90
Nefas-Silk-Lafto	185,461	211,025	396,486	5,805	88
Yeka	201,156	233,443	434,599	4,970	86
Total	**1,624,999**	**1,809,000**	**3,433,999**	**6518**	**90**

Source: *CSA, 2017*

3.1.3 Physiography and drainage

The topography of Addis Ababa is characterized by contrasting plain areas and very steep slopes. In general, flatness dominates the southern part of the city and the slope is steeper in the northern part of the study area. USGS, (2001) slope classification is modified and adapted to reclassify the slope gradient in the study area (Table 3.2). The result shows that 34.4 % is slopping, 28.4 % is moderately steep and 16.7% gently sloping. Whereas 7.2% of the area in the city is characterized by flat to very gently sloping topography and only 0.5% is very steep. The topography forms plateau in the northern, western, South Western, and North-Eastern parts of the city. As a result, the streams drain towards the south from the Entoto mountain range, southeast from Mt. Wechecha, towards southwest from Mt. Yerer and Mt. Furi resembling a dendritic drainage pattern (Teklit

Berhe, 2015). The major rivers that drain the city include Little Akaki, Great Akaki, Kebena, Kechene, Kutume, and Banchi yiketu. The altitude in the city ranges from 2044 to 3141 meters above mean sea level (MSL) with a mean elevation of 2347 meters above MSL (Figure 3.2).

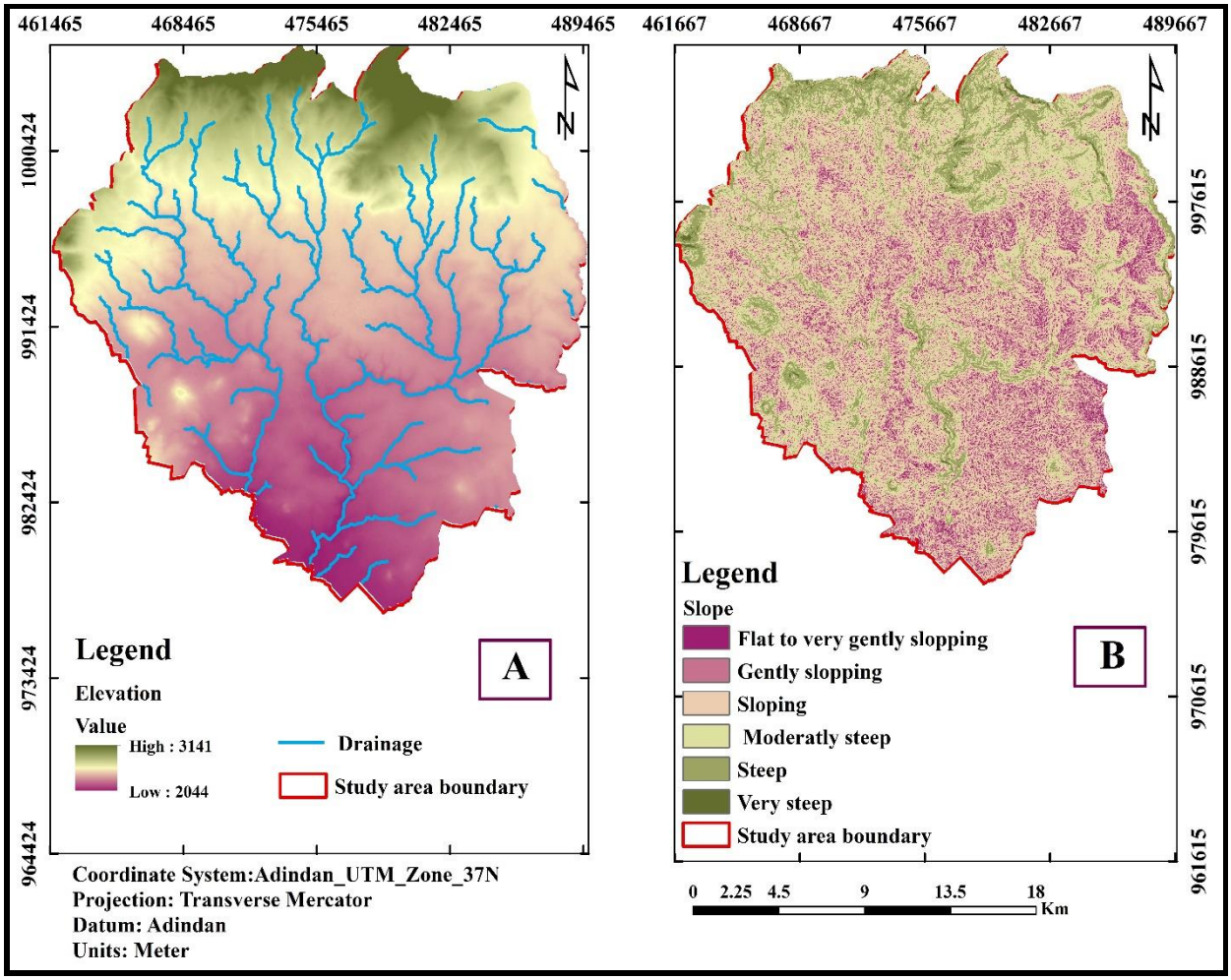

Figure 3. 2: *A) Elevation map and B) Slope map*

Table 3. 2: *Reclassified slope*

Slope gradient in (%)	Description	Area Coverage	
		Area in sq. km.	Percentage
0-2	Flat to very gently sloping	37.9	7.2
2-5	Gently sloping	88.1	16.7
5-10	Slopping	181.2	34.4
10-20	Moderately steep	149.5	28.4
20-50	Steep	67.3	12.8
Above 50	Very Steep	2.6	0.5

Source: *Computed from DEM (12.5m by 12.5m)*

3.1.4 Climate

A. Precipitation

Precipitation data was obtained from the NMA recorded at 12 stations (Abyssinia school, Bole, Addis Ababa observatory, Akaki, Ayertena, Intoto, Kolfe keranyo, Kotebe Luke, Kotebe TTC, Medihanealem School, Megabit 28 School, and Yekatit 23 School) for the last 23 years (1998 to 2020). The result shows that the average precipitation in the city is 1126.48mm. Most of the precipitation in the city was recorded during the rainy season months of June, July, August, and September. The month with the most precipitation on average is August with 286.0mm of precipitation. The month with the least precipitation on average is December with an average of 6.6mm (Figure 3.3). The precipitation ranges from 694.9mm to 1452.0mm during the years 2012 and 2004 respectively (Figure 3.4).

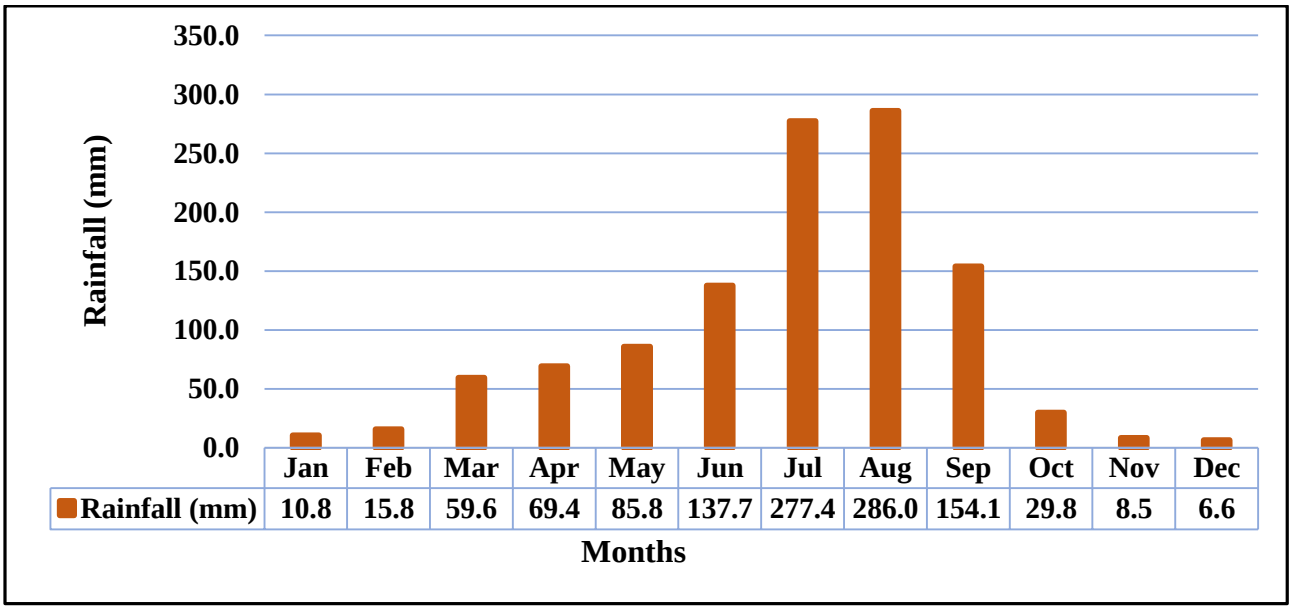

Figure 3. 3: *Average monthly rainfall in Addis Ababa during the years 1998 to 2020*

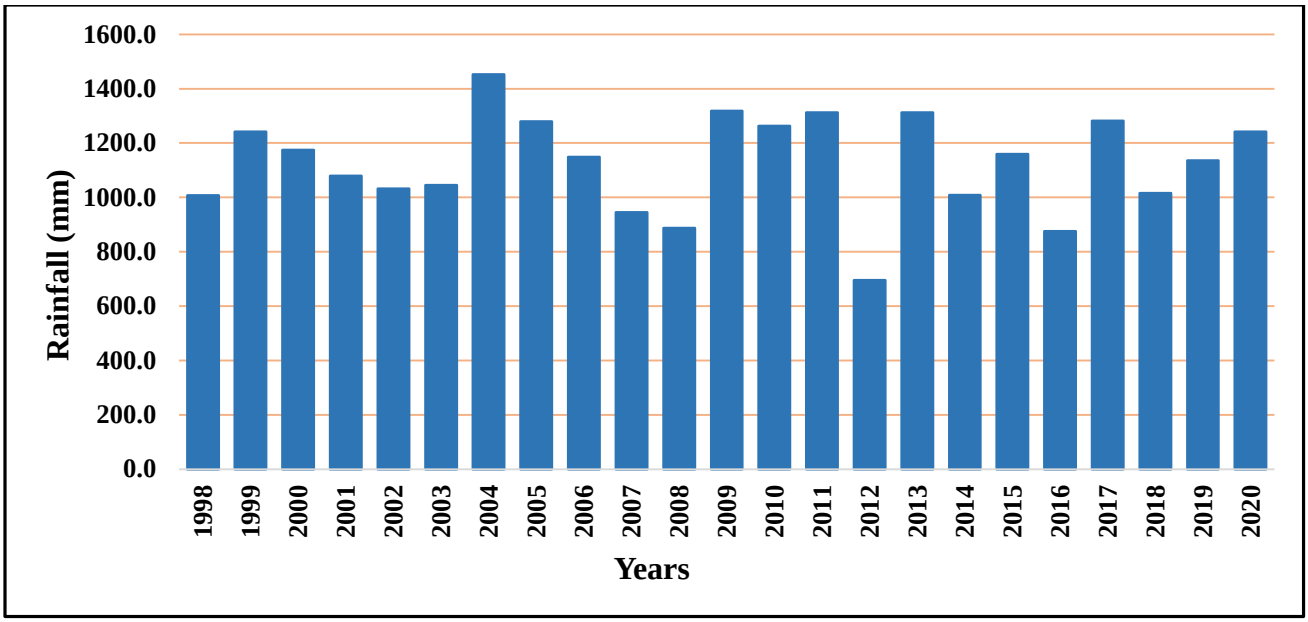

Figure 3. 4: *Annual rainfall distribution in Addis Ababa during the years1998 to 2020*

B. Temperature

The average recorded temperature in Addis Ababa from Abyssinia school, Bole, Addis Ababa observatory, Akaki, Ayertena, Intoto, Kolfe keranyo, Kotebe Luke, Kotebe TTC, Medihanealem School, Megabit 28 School, and Yekatit 23 school stations during the years 1998 to 2020 was 17.2^{0}C. The warmest month, on average, is March with an average maximum temperature of 25.9^{0}C. While the coolest month on average, is December, with an average minimum temperature of 8.3^{0}C (Table 3.3 and Figure 3.5).

Table 3. 3: *Maximum, minimum and mean monthly temperature in Addis Ababa from 1998 to 2020*

	Jan	Feb	Mar	Apr	May	Jun	Jul	Aug	Sep	Oct	Nov	Dec
Temp Max	24.1	25.4	25.9	25.5	25.2	23.5	21.2	20.7	21.9	23.3	23.6	23.3
Mean	16.5	17.8	18.6	18.8	18.7	17.6	16.3	16.0	16.5	16.7	16.3	15.8
Temp Min	8.9	10.1	11.4	12.1	12.2	11.6	11.4	11.3	11.2	10.1	9.1	8.3

Source: *NMA, 2021*

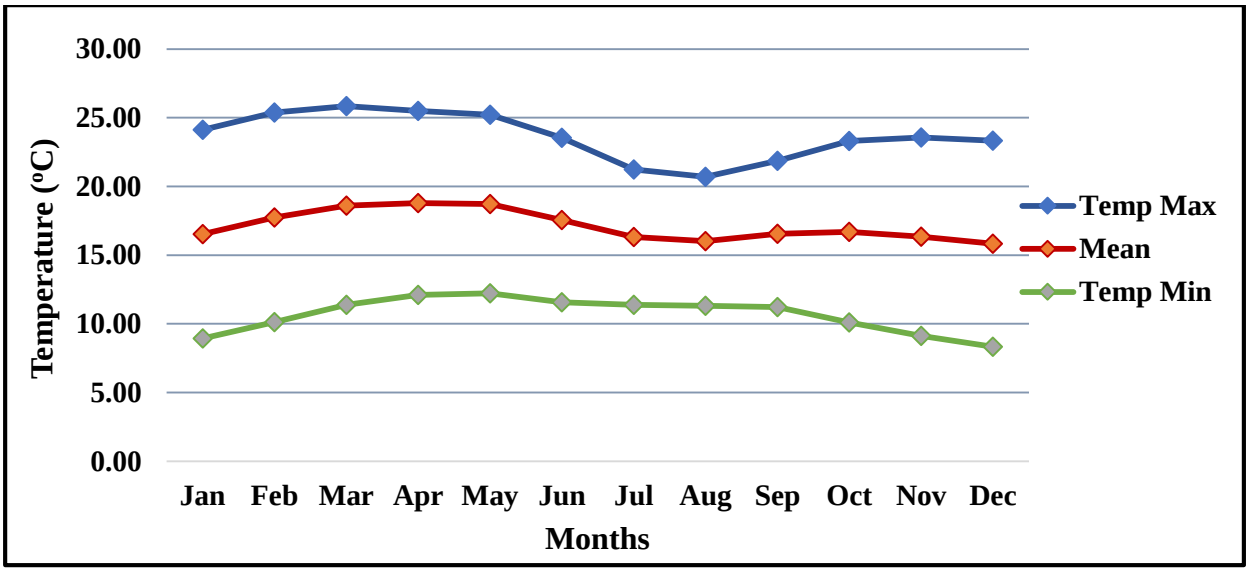

Figure 3. 5: *Minimum, maximum, and mean monthly Temperature in Addis Ababa from 1998 to 2020*

3.1.5 Soil

The information obtained from the Ministry of Water Resource (Ethiopia) indicates that the dominant soil types in the study area are eutric nitisols, calcic xerosols, and chromic luvisols constituting 21.2%, 6.9%, and 2.2% respectively (Table 3.4 and Figure 3.6). Other soil types in the study area include pellic vertisols, orthic solonchaks, and leptosols.

Table 3. 4: *Soil types*

Soil type	Area (sq. km.)	Percentage
Eutric nitisols	111.6	21.2
Calcic xerosols	36.3	6.9
Chromic luvisols	11.4	2.2
Orthic solonchaks	4.9	0.9
Leptosols	2.8	0.5
Pellic vertisols	2.8	0.5

Source: *Based on MoWR digital data, 2004*

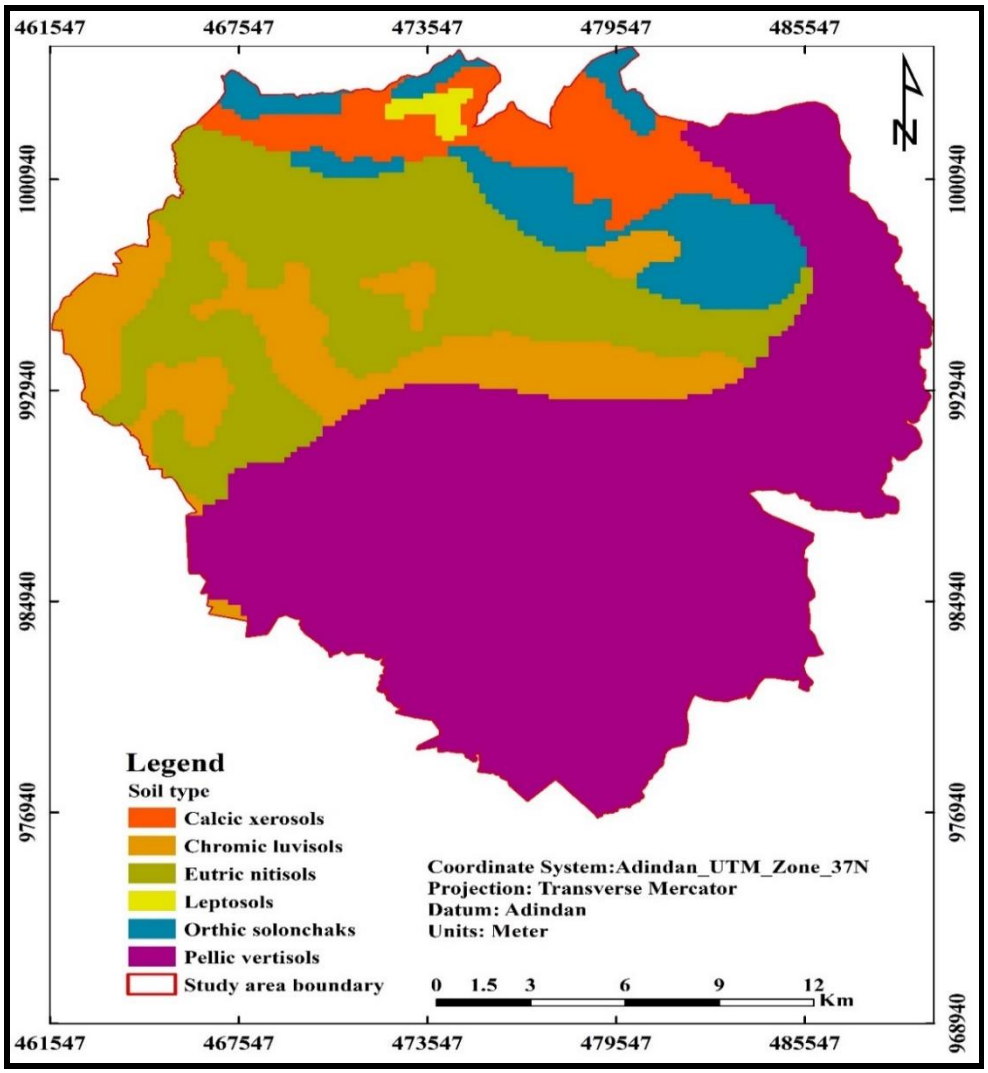

Figure 3. 6: *Soil map, based on MoWR digital data*

3.2 Materials and software

3.2.1 Materials

3.2.1.1 Primary data

Remotely-sensed imageries data have been increasingly used as a primary source of information for remote sensing and geographical information systems (GIS) applications (Craig, 1991). With the obtainability of high-resolution remote sensing images and multi-source geospatial data, there is a boundless requirement to transform Earth observation data into useful information essential for urban planning and decision making (Vatseva et al., 2016). Accordingly, in the present study, high-resolution imagery from commercially available SPOT 5 and freely available Sentinel-2A satellite images were obtained from European Space Agency (ESA) and the USGS website (http://earthexplorer.usgs.gov) respectively. The SPOT 5 and sentinel-2 images were used as input

for the OBIA. Landsat 7 ETM+ and Landsat 8 OLI/TIRS thermal and multispectral images were also freely downloaded from the USGS website to retrieve LST and calculate LULC indices respectively. Additionally, LST data products of MODIS (MOD11A1) Version 6 daily 1km spatial resolution imagery were downloaded freely from the website of Earth Data and used for the retrieved LST validation. Moreover, a 12.5m (resampled) spatial resolution digital elevation model (DEM) was acquired from the Alaska Satellite Facility (ASF) (www.asf.alaska.edu) to generate data on drainage, elevation, and slope gradient layer for the study area (Table 3.5). Furthermore, for ground-truthing and image classification accuracy validation reference data was collected using Google Earth image and handheld GPS devices with an accuracy of ± 3 m.

Table 3. 5: *Satellite images and details of their respective bands used*

Data set	Band name	Central band/band width (µm)	Spatial resolution	Acquisition date	Purpose	Source
SPOT 5	B1 (Green) B2 (Red) B3 (NIR) SWIR	0.49-0.61 0.61-0.68 0.78-0.89 1.58-1.70	10mX10m 10mX10m 10mX10m 20mX20m	Jan, 2006	OBIA and LULC Classification	ESA
Sentinel-2A	Band 2 (Blue) Band 3 (Green) Band 4 (Red) Band 8 (NIR) Band 11 (SWIR)	0.49 0.56 0.665 0.842 1.61	10mX10m 10mX10m 10mX10m 10mX10m 20mX20m	Jan 25, 2016 and Jan 18, 2021	OBIA and LULC Classification	USGS
Landsat 7 ETM+	Band 1 (Blue) Band 2 (Green) Band 3 (Red) Band 4 (NIR) Band 5 (SWIR 1) Band 6 (Thermal)	0.45 - 0.52 0.52 - 0.60 0.63 - 0.69 0.77 - 0.90 1.55 - 1.75 10.40 - 12.50	30mX30m 30mX30m 30mX30m 30mX30m 30mX30m 30mX30m	Jan 04,2006	LULC indices calculation and LST retrieval	USGS
Landsat 8 OLI/TIRS	Band 2 (Blue) Band 3 (Green) Band 4 (Red) Band 5 (NIR) Band 6 (SWIR 1) Band 10(Thermal 1)	0.452 - 0.512 0.533 - 0.590 0.636 - 0.673 0.851 - 0.879 1.566 - 1.651 10.60 - 11.19	30mX30M 30mX30M 30mX30M 30mX30M 30mX30M 30mX30m	Jan 24, 2016 and Jan 05, 2021	LULC indices calculation and LST retrieval	USGS
MODIS-LST	Band 31 (TIR) Band 32 (TIR)	10.78 -11.27 11.77 - 12.27	1kmX1km 1kmX1km	Jan 04,2006, Jan 24, 2016 & Jan 05, 2021	For LST validation	Earth Data
DEM	Not Applicable	Not Applicable	12.5mX12.5m (resampled)	April 2008	slope, drainage, and elevation	ASF

The study period covers 15 years and the years 2006, 2016, and 2021 were selected to analyze the spatiotemporal pattern of urban-blue green landscapes and their effect on LST. These years were selected due to the availability of high-resolution images at hand. All the images were acquired during the dry month of January to minimize atmospheric problems such as cloud and haze effects.

3.2.1.2 Secondary data

Shapefiles with attributes of administrative boundaries, roads, rivers as well as population data from the Central Statistical Agency (CSA) of Ethiopia were collected and used as secondary data sources in this study. Besides, Meteorological station data on temperature and precipitation, and digital soil data were collected from the National Meteorological Agency (NMA) of Ethiopia, and the Ministry of Water Resource-Ethiopia (MoWR) respectively.

3.2.2 Software

The main software packages that were used in this study include ESRI product ArcGIS 10.6.1, ERDAS Imagine 2015, QGIS 3.10.5, eCognition Developer 9.1, ENVI 5.3, Stata 15, Google Earth Pro, and Microsoft Office products (Microsoft Office and Excel).

3.3 Methods

3.3.1 Image pre-processing

For better feature identification and other related applications, raw satellite images cannot be used due to mainly radiometric, atmospheric, and geometric effects. Hence, pre-processing was carried out before data processing and information extraction. Preprocessing carried out for SPOT 5, Sentinel-2A, Landsat 7 ETM+, and Landsat 8 OLI/TIRS imageries include radiometric correction (haze and noise reduction), geometric correction (by providers), layer stacking, and sub setting. Image mosaicking was also implemented on SPOT 5 and Sentinel-2A image scenes on ERDAS Imagine 2015. Another task of pre-processing includes scan-line error correction (SLC) which is applied for the Landsat 7 ETM+ images (Bands 1 to 6). The SLC was performed using the gap-fill tool in QGIS 3.10.5. For the thermal bands of Landsat 7 ETM+ (Band 6) and Landsat 8 TIRS (Band 10), atmospheric correction, particularly the Dark Object Subtraction-1 (DOS-1) method as proposed by (Chavez Jr, 1988) was applied using the Semi-automatic classification plugin (SCP) in QGIS (Filgueira et al., 2019).

3.3.2 Image enhancement

Image enhancement refers to improving the image quality to a better and more understandable level for information extraction and interpretation. It is carried out for better interpretation of images by human viewers (Bhatta, 2011). Numerous ways help to enhance an image. In this study, band rationing or indices (arithmetic operations performed on images) were used. Accordingly, during image classification, NDVI, NDBI, and MNDWI were computed within eCognition Developer 9.1 to boost the interpretability of vegetation, built-up, and water land use/cover classes respectively.

3.3.3 Image classification

Image classification is the process of assigning and labeling groups of image objects or pixels based on spectral and spatial information for classification. There are various techniques for classifying remotely sensed images. The common ways of classification include pixel-based such as unsupervised, Supervised, and hybrid classification, and image object-based. In this study, the object-based image analysis was applied (see section 3.3.3.2 for details). The true color combination of the land cover classes in the study area is presented in Appendix 5.

3.3.3.1 Nomenclature of land cover classes

To standardize the classification United States Geological Survey (USGS) land cover classification system was contextualized and adopted (USGS, 1975 as cited in Hillel and Hatfield, 2005). Thus, five land cover classes were identified in the study area. These are the built-up, vegetation, urban farmland, bare land, and water. The description of each land use classes is presented as follows:

Built-up: include areas allotted to residential, commercial and services, industrial, transportation, communication and utilities, mixed urban and other paved surfaces.

Figure 3. 7: *A picture of a built-up area in Addis Ababa, taken from Mt. Yeka*

Vegetation: include forests, grasslands, shrubs, and other green spaces (except cropland).

Figure 3. 8: *An example green landscape within Friendship Square/Park*

Urban farmland: include urban cultivated land (farmland with and without crop).

Figure 3. 9: *A picture of onion farm in Akaki area, Southern Addis Ababa*

Bare land: bare exposed rock, excavation sites, quarries, and gravel pits.

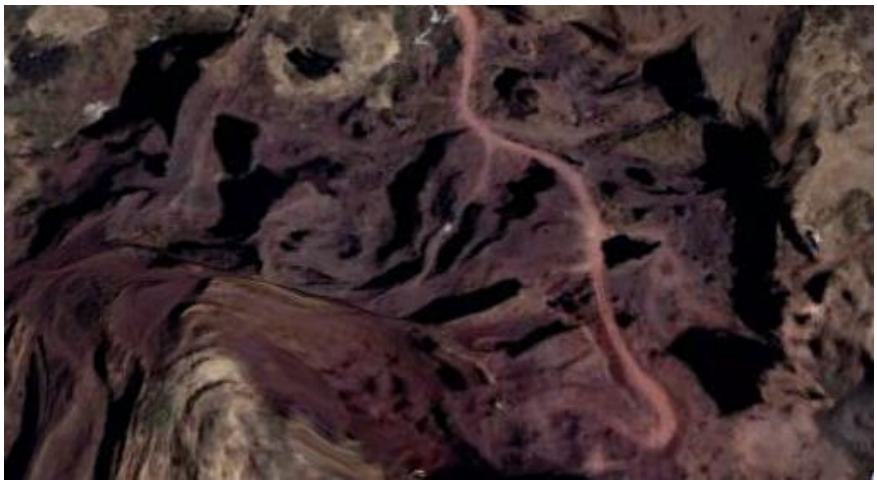

Figure 3. 10: *A picture of the red ash excavation site in Southern Addis Ababa*

Source: *(Google Earth, 2021)*

Water: include both the flowing and standing urban surface waters such as rivers, ponds, and lake and wastewater treatment sites.

Figure 3. 11: *A picture of an artificial lake inside Friendship Square/Park*

3.3.3.2 Object-based image analysis (OBIA)

For this particular study, Object-based image analysis was applied using high-resolution imageries of SPOT 5 and Sentinel-2A satellites as an input. OBIA is more robust than the pixel-based paradigm as its potential for image classification in heterogeneous areas like urban areas has been proved (Bisquert et al., 2014).

Unlike pixel-based classification, OBIA always analyzes images as objects instead of pixels that enables to reduce the ‘‘salt and pepper” effect which emanates from neighboring pixels and results in better classification accuracy (Ziwei et al., 2019). OBIA is a rule set-based technique and involves a two-step process: (i) image segmentation followed by (ii) classification and merging. eCognition Developer 9.1 software was used to implement the OBIA.

Segmentation

Segmentation is a process where an image scene is decomposed into image objects that have similar textural, spectral, and spatial attributes. Segmentation is very important because the resulting image objects are inputs for the subsequent step (classification) (Witharana and Civco, 2014).

In eCognition Developer software, there are numerous algorithms for segmentation. A few of them include Multi-Resolution Segmentation (MRS), Multi-Threshold Segmentation (MTS), and Spectral Difference Segmentation (SDS). MRS was used in this particular study, as it has been proven to be one of the most effective image segmentation algorithms in the OBIA framework (Witharana and Civco, 2014). MRS is a region growing method that starts with a pixel forming an object and merging the neighboring homogeneous pixels until the parameters criterion (set by the user) is attained (Bisquert et al., 2014). The main parameters that govern MRS are the scale (Controls the size of resulting objects), Shape (controls the weight of color during segmentation as shape + color =1), and Compactness (controls the compactness of the resulting object as compactness + smoothness =1). Different combination of these parameters was experimented using the Trail-and-Error approach to get the best combination (Gülçin and Akpinar, 2018; Labib and Harris, 2018). An example of segmentation result and segmentation parameters combination is presented in Figure 3.12 and Table 3.6 respectively.

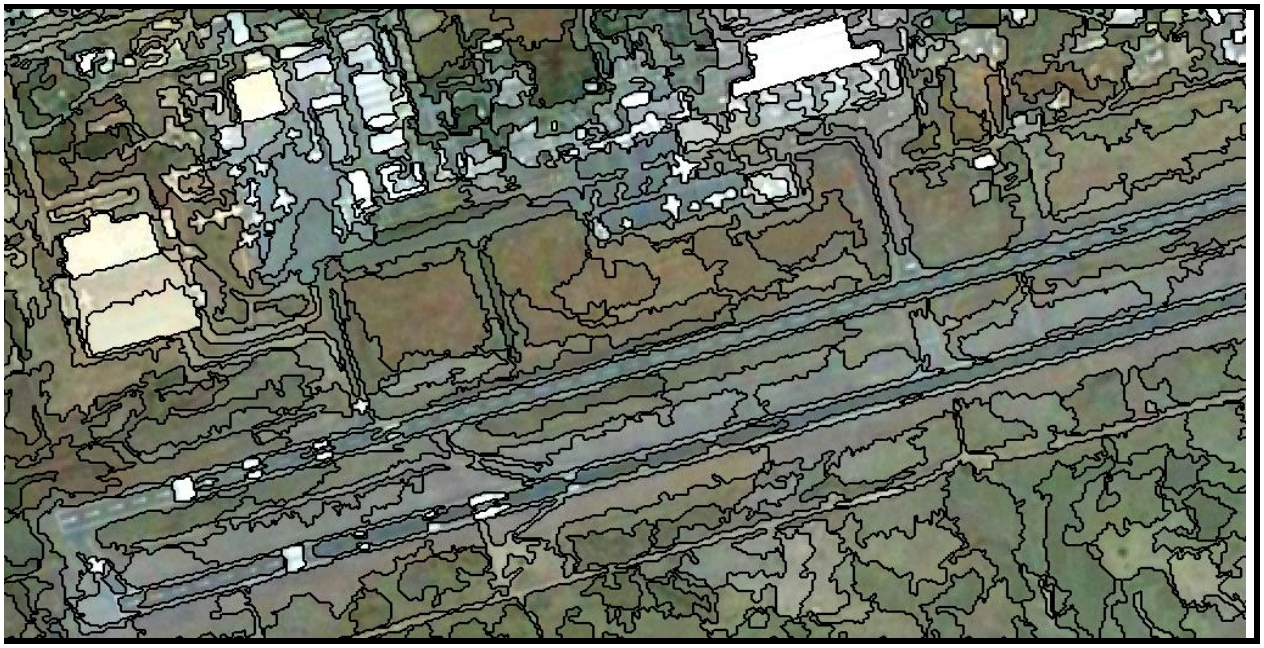

***Figure 3. 12**: An example of segmentation during 2006 with scale=30, shape=0.3 & compactness=0.1*

Table 3. 6: *Segmentation parameters combinations for 3 images*

Algorithm	Segmentation parameters	SPOT 5 (2006)	Sentinel-2A (2016)	Sentinel-2A (2021)
Multi-Resolution Segmentation (MRS)	Layer weights (Blue, Green, red, NIR)	1,1,1	1,1,1,2	1,1,1,2
	Scale parameter	30	30	30
	Shape	0.3	0.2	0.3
	Compactness	0.1	0.2	0.3
	No of resulting image objects	62,605	128,269	167,454

Source: *Computed from eCognition Developer 9.1 software*

Classification and merge

This is the second stage in OBIA where the image objects generated were categorized into built-up, vegetation, urban farmland, bare land, and water land use/cover classes. Various classification algorithms are integrated with eCognition Developer 9.1 software. Quite a few of them include assign class, classification, and hierarchal classification.

Figure 3. 13: *An example of the process tree with rule sets for 2021 classification in eCognition*

The assign class algorithm is the simplest algorithm among them and has been applied in this study (Akmalov et al., 2017). The Assign class algorithm requires the user to set at least four parameters: (i) level, (ii) class filter (the class from which the image objects are assigned to the user class), (iii) threshold condition (determines whether an image object matches a condition or not), (iv) use class (the new or existing class to which the image objects are supposed to be assigned).

In this study, five major image object features are used for classifying the objects into proper land use classes. These are (i) layer values such as the brightness and standard deviation, (ii) geometry of objects (e.g., areal extent in pixels), (iii) shape (e.g., asymmetry and rectangular fit), (iv) class-related features like relative border to other classes and (v) customized object features, for instance, NDVI, NDBI, and MNDWI which were used to extract vegetation, built-up and water land cover classes respectively. An example of a process tree with rule sets is presented in Figure 3.13.

During classification, there was confusion between vegetation and urban farmland (with crop). However, an attempt has been made to differentiate the classes using rectangular fit (as croplands have higher rectangular fit value) and a manual editing tool. Bare land was also mixed with urban farmland (without crop). Brightness value was used to discriminate between bare land and farmland (without crop) given the brightness values for bare land are relatively higher in general.

Finally, each land cover class is merged using the merge region algorithm in eCognition and the final result was exported in ERDAS Imagine images (*.img) format for layout and further analysis.

3.3.3.3 Classification accuracy assessment

The process of estimating accuracy is the next step that follows classification. Inaccurate classification results might lead to misleading analyses, and consequently to misleading conclusions. The confusion matrix (sometimes called contingency table or error matrix) was used to estimate accuracy measures such as overall accuracy, Producer's accuracy, user's accuracy, and Kappa statistics. Overall accuracy is calculated by dividing the total number of properly classified pixels (sum of the values on the confusion matrix's main diagonal) by the total number of reference pixels, which is a fairly coarse assessment. The producer's and user's accuracy are used to measuring the accuracy of individual classes. In the confusion matrix, the producer's accuracy is computed by dividing cell (i i) by the sum of column i while the user's accuracy is computed by dividing (i i) by the sum of row (Gašparović, 2020).

The Kappa coefficient, K is a more robust measure of classification accuracy than overall accuracy as it takes into account the off-diagonal elements and the diagonal terms. (Ahmad and Quegan, 2012). It is computed as (Gašparović, 2020):

$$k = \frac{N\sum_{i=1}^{r} Xii - \sum_{i=1}^{r}(Xi+*X+i)}{N^2 - \sum_{i=1}^{r}(Xi+*X+i)} \quad (3.1)$$

Where:

r - number of rows in the confusion matrix,

Xii – the values in column i and row i (on the main diagonal),

X_{i+} - the total number of measurements in row i,

X_{+i} - the total number of measurements in column i, and

N -is the number of measurements in the matrix as a whole.

Map of the ground control points is presented in Appendix 7.

3.3.4 LULC change detection

Change in LULC pattern was computed in square kilometers for each land cover class during the periods. LULC conversion matrix (image differencing) technique was applied in a GIS environment to detect the change directions i.e. which land use/cover class has converted into what (Binyam Alemu et al., 2015). The percentage share (Ebrahim Esa and Mohammed Assen, 2017) of each land-use class and the annual rate of change (Belaybeh Bufebo and Eyasu Elias, 2021) in square kilometers per year was calculated to obtain the magnitude of the changes undergone between the study periods using equations 3.2 and 3.3 respectively as follows:

$$\text{Percentage share} = \left(\frac{T2 - T1}{T1}\right) * 100, \quad (3.2)$$

$$\text{Rate of change (Sq.km/year)} = \left(\frac{T2 - T1}{N}\right) \quad (3.3)$$

Where: T1 and T2 area of land use/land cover type at the initial and final year respectively and

N is the time interval/number of years between the initial and final years.

3.3.5 Land surface temperature retrieval

Land Surface Temperature (LST) is defined as the temperature of the earth's surface which we feel when we directly touch or contact it. In other words, it is the skin temperature of the surface (NASA, 2000). In this study, the thermal bands of Landsat 7 ETM+ (Band 6) and Landsat 8 TIRS Band 10 are used to calculate LST. Landsat 8 TIRS Band 10 is preferred due to the higher stary light error and larger calibration uncertainty associated with band 11 (Guha, 2018; USGS, 2019b; Abel Balew and Tesfaye Korme, 2020). To estimate LST, several steps have been followed:

3.3.5.1 Conversion of DNs to at sensor spectral radiance

The first step in estimating LST is converting row digital numbers (DNs) values to at sensor radiance. Equations 3.3 (USGS, 2019a) and 3.4 (USGS, 2019b) are used to convert DNs into radiance units for Landsat ETM+ thermal band (band 6) and Landsat 8 TIRS band 10 respectively.

$$L_\lambda = \left(\frac{LMAX\lambda - LMIN\lambda}{QCALMAX - QCALMIN}\right) * (QCAL - QCALMIN) + LMIN_\lambda \quad (3.3)$$

Where:

L_λ is at sensor spectral radiance in (Watts/ (m^2 * sr * µm)),

QCAL stands for quantized calibrated pixel value (DNs),

$LMIN_\lambda$ is spectral radiance scaled to QCALMIN in (Watts/ (m^2 * sr * µm)) = 3.2

$LMAX_\lambda$ is spectral radiance scaled to QCALMAX in (Watts/ (m^2 * sr * µm)) = 12.65

QCALMIN in DN = 1 is the minimum quantized calibrated pixel value (equivalent to LMIN), QCALMAX in DN =255 is the maximum quantized calibrated pixel value (equivalent to LMAX).

$$L_\lambda = ML * Q_{cal} + AL \quad (3.4)$$

Where: L_λ is at sensor spectral radiance (W/ (m2 * sr * µm)), M_L is RADIANCE_MULT_BAND_n from the metadata (radiance multiplicative scaling factor for the band) = 0.0003342, A_L is RADIANCE_ADD_BAND_n from the metadata (Radiance additive scaling factor for the band) = 0.1 and Qcal = Standard product pixel values that have been quantized and calibrated (DN).

3.3.5.2 Top of atmosphere brightness temperature

This refers to the effective at-satellite temperature and is computed as follows (USGS, 2019a; USGS, 2019b):

$$T = \frac{K2}{\ln(\frac{K1}{L\lambda}+1)} \quad (3.5)$$

Where:

T - Effective at-satellite temperature in Kelvin,

L_λ - Spectral radiance at the sensor's aperture in (Watts/ (m^2 * sr * µm)),

K1- Band-specific thermal conversion constant one from the metadata and K2 - Band-specific thermal conversion constant two from the metadata as presented in Table 3.7.

Table 3. 7: *Meta data of thermal constants for Landsat 7 ETM+ (Band 6) & Landsat 8 TIRS (Band 10)*

Landsat 7 ETM+ (Band 6)		**Landsat 8 TIRS (Band 10)**	
Thermal constant (K1)	Thermal constant (K2)	Thermal constant (K1)	Thermal constant (K2)
666.09	1282.71	774.8853	1321.0789

Source: *Metadata file of Landsat 7 ETM+ (2006) and Landsat 8 OLI/TIRS (2016 and 2021)*

3.3.5.3 Land surface emissivity estimation

Before LST retrieval, land surface emissivity was computed after calculating NDVI. Equations 3.8 and 3.6 (Van de Griend and Owe, 1993) are utilized to obtain NDVI and LSE respectively.

$$LSE\ (\varepsilon) = 1.009 + 0.047 * \ln(NDVI) \quad (3.6)$$

3.3.5.4 LST estimation

Finally, Mono-Window Algorithm (Kumari et al., 2018; Rongali et al., 2018; Simwanda et al., 2019) is implemented to retrieve LST on ERDAS Imagine 15 model maker using equation 3.7.

$$LST\ (^oC) = \frac{T}{1+\left(\lambda\ X\ \frac{T}{\rho}\right) ln\varepsilon} - 273.15 \quad (3.7)$$

Where λ = average wave- length of emitted radiance (λ = 11.45 µm and 10.89 µm for Landsat 7 ETM+ Band 6 and Landsat-8 band 10 respectively; $\rho = h \times c/\sigma$ (1.438×10^{-2} mK), σ = Boltzmann constant (1.38×10^{-23} J/K), h = Planck's constant (6.626×10^{-34} Js) and c = velocity of light (2.998×10^{-8} m/s); and ε is the land surface emissivity. Therefore, ρ = 14380 (Rongali et al, 2018).

3.3.5.5 LST result validation

The common methods used for validating LST derived from TIRS sensors include near-surface air temperature, ground-based measurements (Avdan and Jovanovska, 2016), and LST retrieved from other TIR sensors (Yosef Mengistu et al., 2017). In this study, LST retrieved from another sensor i.e., Moderate Resolution Imaging Spectrometer (MODIS) product MOD11A1 of 1 km spatial resolution was used for comparison and validation purposes.

The validation was carried out in several steps. First, the MODIS LST product obtained from the Earth Data website was downscaled multiplying by 0.02. Second, a total of 500 random points were generated and LST values were extracted to the generated points using ArcGIS 10.6.1 for each study year. Then, for the sake of comparison and validation the original Landsat 7 ETM+ and Landsat 8 LST result (30m) is resampled to 1km spatial resolution to match with MODIS LST product using bilinear interpolation on ERDAS Imagine (Yosef Mengistu et al., 2017). Eventually, the difference between the MODIS LST product and retrieved LST was computed for each of the generated points.

3.3.6 Land use land cover indices

There are several kinds of LULC indices used in geospatial studies. In this study, LULC indices such as Normalized Difference Vegetation Index (NDVI), Normalized Difference Built-up Index (NDBI), and Modified Normalized Difference Water Index (MNDWI) has been used to analyze the relationship of LST against Vegetation, the built-up environment, and the blue landscape land use classes respectively. The indices were computed from Landsat ETM+ (for the year 2006) and Landsat 8 OLI/TIRS (for the years 2016 and 2021) imageries. NDVI was developed by (Rouse et al., 1973) and computed as follows:

$$NDVI = \frac{(\rho NIR - \rho red)}{(\rho NIR + \rho red)} \quad (3.8)$$

Where; ρred – reflectance in the red band (Band 3 for the Landsat 7 ETM+ sensor and Band 4 for the Landsat 8 OLI/TIRS sensor) and ρNIR- reflectance in the Near-Infrared band (Band 4 and Band 5 for the Landsat 7 ETM+ and Landsat 8 OLI/TIRS sensors respectively). NDVI value ranges between -1 and +1 and it enhances all vegetation and resulting in a positive value. Soil may have a nearby zero value, while waterbody features have negative values (John et al., 2020).

The Normalized Difference Built-up Index has been developed by (Zha et al., 2003) and expressed as follows:

$$\text{NDBI} = \frac{(\rho\text{SWIR1} - \rho NIR)}{(\rho\text{SWIR1} + \rho NIR)} \quad (3.9)$$

Where; ρSWIR- reflectance in the Short-Wave Infrared band (Band 5 in Landsat 7 ETM+ and Band 6 in Landsat 8 OLI/TIRS). The values of NDBI ranges from -1 to +1 where built-up areas tend to have higher positive values. Water bodies have negative NDBI values and values closer to zero NDBI values indicate areas with vegetation cover (Abel Balew and Tesfaye Korme, 2020).

The MNDWI is calculated using equation 3.9 as suggested by (Hanqiu Xu, 2006).

$$\text{MNDWI} = \frac{(\rho\text{Green} - \rho SWIR1)}{(\rho\text{Green} + \rho SWIR1)} \quad (3.10)$$

Where; ρGreen- reflectance in the green band (Band 2 for Landsat 7 ETM+ and Band 3 for Landsat 8 OLI/TIRS). The result of the MNDWI produces three results: (i) water with greater positive values. (ii) Built-up areas having negative values; and (3) soil and vegetation with negative values.

3.3.7 Statistical analysis

The relationship between LST with NDVI, NDBI, MNDWI and altitude was analyzed using linear regression. The regression was carried out for all the study years with LST as the dependent variable and NDVI, NDBI, MNDWI and altitude as the independent variables. To perform the regression analysis, 3 steps have been followed.

First, a total of 1000 random points were generated from NDVI, NDBI, MNDWI and (DEM) altitude raster for the study years 2006, 2016, and 2021.

Afterward, values were extracted from the raster files for each generated point. Create random points tool and extract multi values to points tools were utilized from ArcGIS 10.6.1 to generate the random points and extract the respective values respectively.

Finally, spatial scatter plots with Pearson's correlation coefficient (r) and coefficient of determination (R^2) values were calculated to determine the degree of relationship and the amount of information shared between LST and LULC indices using Stata 15 software (Naeem et al., 218). The linear regression coefficient (r) is interpreted based on the strength of ±0.50 to ±1 represents a strong correlation, ±0.30 to ±0.49 represents a medium correlation, and below ±0.30 represents

a weak correlation (Statistics Solutions, 2021). The general workflow of the study is shown in Figure 3.14

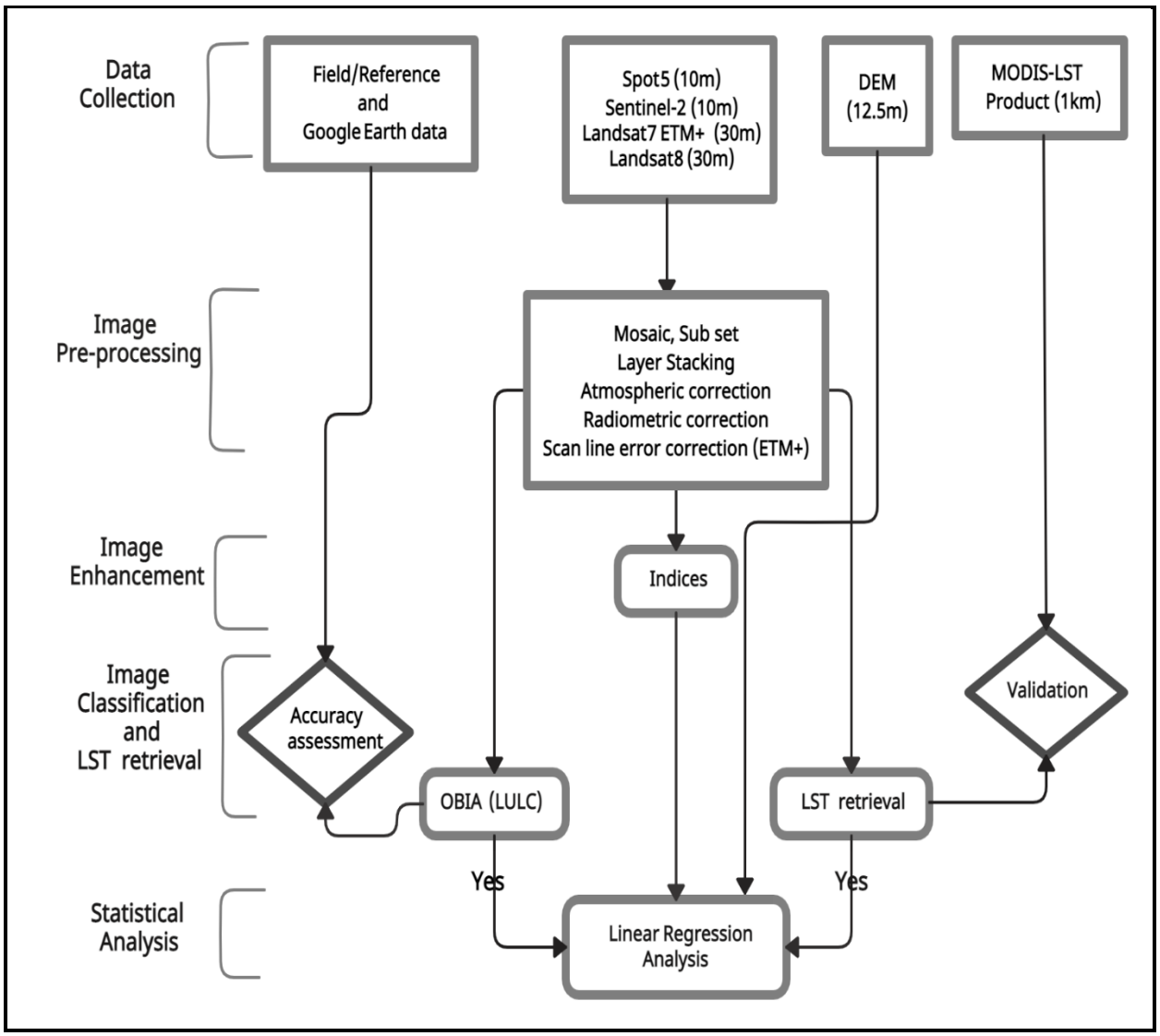

Figure 3. 14: *General workflow of the study*

CHAPTER FOUR

4. RESULTS

4.1. Object-based image classification accuracy assessment

Tables 4.1, 4.2, and 4.3 shows several LULC classification accuracy measures such as overall accuracy, producer's accuracy, user's accuracy, and Cohen's kappa coefficient.

Table 4. 1: *Accuracy assessment of LULC classification during 2006 using a confusion matrix*

Classified	Water	Urban farmland	Vegetation	Built-up	Bare land	Row total	User's accuracy
Water	**27**	1	1	0	0	30	90%
Urban farmland	0	**47**	0	1	2	50	94%
Vegetation	1	1	**38**	0	0	40	95%
Built-up	0	2	2	**56**	0	60	93%
Bare land	0	1	2	0	**37**	40	92%
Column total	28	52	43	57	39	220	
Producer's accuracy	96%	90%	88%	98%	95%		
Overall Classification Accuracy = 93%			**Overall Kappa Statistics = 91%**				

Table 4. 2: *Accuracy assessment of LULC classification during 2016 using a confusion matrix*

Classified	Water	Urban farmland	Vegetation	Built-up	Bare land	Row Total	User's accuracy
Water	**29**	0	1	0	0	30	96%
Urban farmland	1	**46**	1	1	1	50	92%
Vegetation	0	2	**38**	0	0	40	95%
Built-up	0	0	1	**57**	2	60	95%
Bare land	0	0	1	2	**37**	40	90%
Column total	30	48	42	60	40	220	
Producer's accuracy	96%	95%	90%	95%	92%		
Overall Classification Accuracy = 94%			**Overall Kappa Statistics = 92%**				

Table 4. 3: *Accuracy assessment of LULC classification during 2021 using a confusion matrix*

Classified	Water	Urban farmland	Vegetation	Built-up	Bare land	Row total	User's accuracy
Water	**27**	1	2	0	0	30	90%
Urban farmland	1	**37**	1	0	1	40	92%
Vegetation	0	0	**49**	0	1	50	98%
Built-up	0	2	0	**58**	0	60	96%
Bare land	0	0	2	0	**38**	40	95%
Column total	28	40	54	58	40	220	
Producer's accuracy	96%	92%	90%	100%	95%		
Overall Classification Accuracy = 95%			**Overall Kappa Statistics = 93%**				

The final object-based LULC classification result shows an overall accuracy of 93%, 94%, and 95% during 2006, 2016, and 2021 respectively. Whereas, Cohen's kappa coefficient became 91%, 92%, and 93% for 2006, 2016, and 2021 classification results respectively. (Tables 4.1 - 4.3).

4.2. Spatiotemporal dynamics in land use/and cover

Spatiotemporal analysis of LULC was carried by applying an object-based image analysis approach using high-resolution satellite imagery as an input. The land cover of the study area was categorized into the built-up, vegetation, urban farmland, bare land, and water land cover classes. Table 4.4 portrays the land cover classification and analysis result during January 2006, 2016, and 2021.

In January 2006 the largest share of the LULC goes to built-up with a total of 211. 7 sq.km (40.2 %) followed by urban farmland, vegetation and bare land accounting 141.3 sq.km (26.8%), 105.0 sq.km (19.9%) and 67.7 sq.km (12.9%) respectively.

In January 2016, the built-up had grown more in aerial coverage having a total area of 301.1 sq. km which is 57.1% of the total land cover in the city. During this year the aerial extent of vegetation, urban farmland, and bare land had noticeably diminished to 95.3 sq. km (18.1%), 93.2 sq. km (17.7%), and 36.1 sq. km (6.8%) respectively.

Table 4. 4: *Land use/cover dynamics during 2006, 2016 and 2021*

Land cover class	2006		2016		2021		Annual rate of change	
	Area (sq.km)	Percent	Area (sq.km)	Percent	Area (sq.km)	Percent	Area (sq.km)	Percent
Built-up	211.7	40.2	301.1	57.1	350.6	66.5	9.3	4.4
Vegetation	105.0	19.9	95.3	18.1	95.9	18.2	-0.6	-0.6
Urban farmland	141.3	26.8	93.2	17.7	57.7	10.9	-5.6	-3.9
Bare land	67.7	12.8	36.1	6.8	21.4	4.1	-3.1	-4.6
Water	1.6	0.3	1.5	0.3	1.6	0.3	0.0	0.0
Total	**527.2**	**100.0**	**527.2**	**100.0**	**527.2**	**100.0**		

Source: *Computed using ArcGIS 10.6.1*

Likewise, in January 2021 the built-up land remains the dominant land cover class considerably expanding its coverage to 350.6 sq. km representing 66.5% of the total land coverage. Vegetation accounts for 95.9 sq. km (18.2%) resembling a very slight increase i.e., 0.6 sq. km increase between the period January 2016 and 2021. In contrast, urban farmland and bare land had revealed a drastic decline in aerial coverage bringing the figures down to 57.7 sq. km (10.9%) and 21.4sq.km (4.1%) respectively. The water land cover class accounts 1.6 sq.km (0.3%), 1.5 sq.km (0.3%) and 1.6

sq.km (0.3%) during January 2006, 2016 and 2021 respectively. The result also depicts that, during the period between January 2006 and 2021 the built-up had substantially grown by 138.9 sq. km which is 65.7% of the built-up in 2006. Whereas, urban farmland, bare land, and vegetation have reduced by 83.7 sq. km, 46.2 sq. km, and 9.2 sq. km respectively. The annual increasing rate of change in built-up from 2006 to 2021 was 4.4%, but, bare land, urban farmland, and vegetation declined annually by 4.6%, 3.9%, and 0.6% respectively.

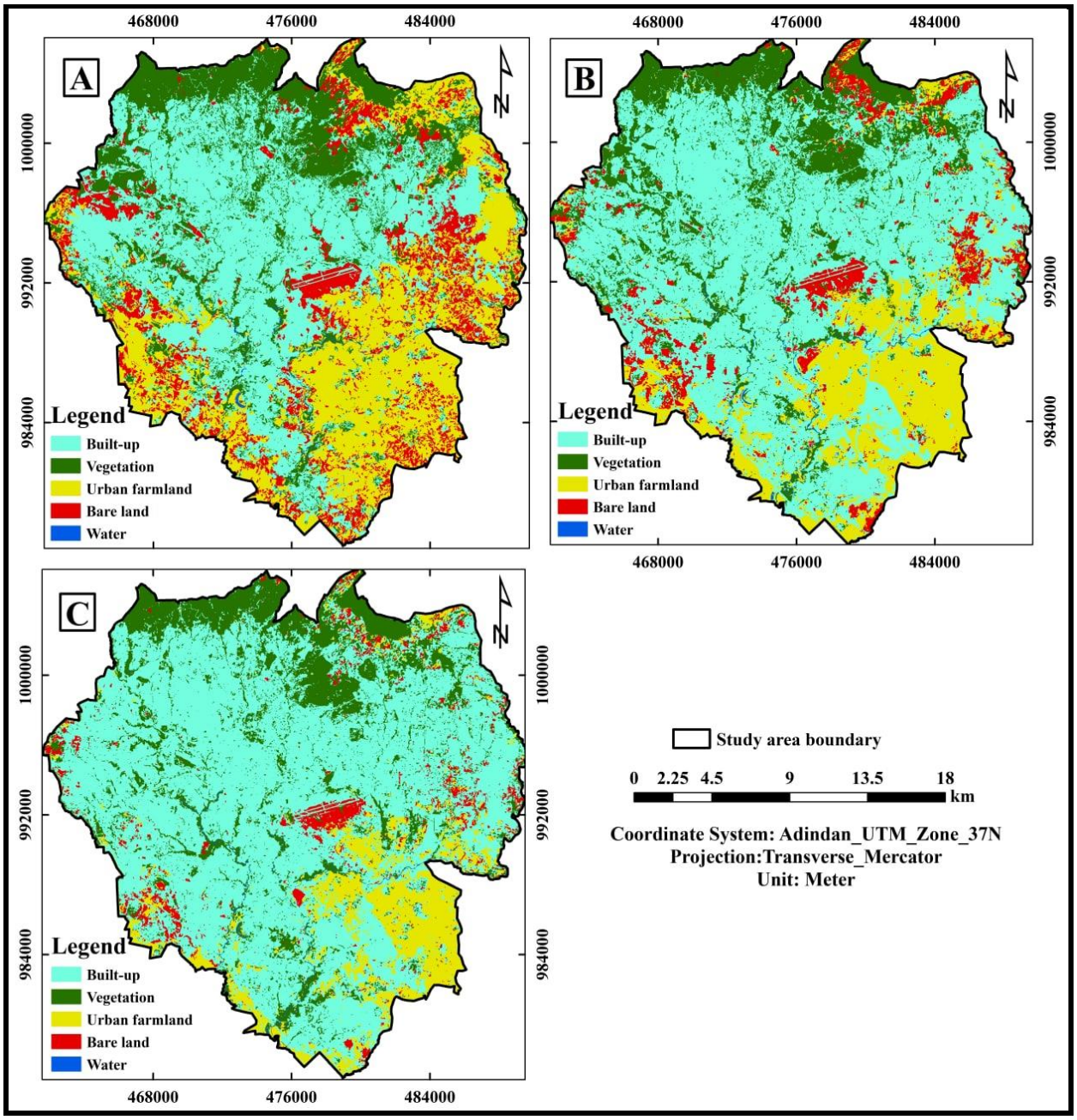

Figure 4. 1: *LULC map A) during 2006, B) during 2016 and C) during 2021*

The spatial LULC distribution presented in figure 4.1 shows that the vegetation cover is mainly observed in the Northern part of the city and along the river banks throughout the study periods. Bare land was observed in the North-Eastern, Eastern, Central, Western, Southern, South-Western, and South-Eastern parts of the city. While urban farmland was distributed in the North-Eastern, Eastern (only during 2006), Western (only during 2006), Southern, South-Western, and South-Eastern parts of the city. Figure 4.1 also reveals that the city expansion is heading towards the Eastern, Western, and Southern parts of the city.

4.2.1 Land use/cover conversion matrix

The land use/land cover matrices show the extent and direction of what is changing to what i.e. which land use/cover class is transforming into another and which remains unchanged. The results from change matrices revealed 20 types of conversion between the land use/cover categories (Table 4.5 and Appendix 6). However, the conversion between water and other land use classes was not taken into account as there was no considerable conversion from and to water. The result illustrates that during the whole study period (2006 to 2021), most of the urban farmland was converted into built-up by 75.9 sq. km (53.7%) and followed by the conversion into vegetation by 13.3 sq. km (9.4%) and bare land by 7.4sq.km (5.3%). In this manner, 40.2 sq. km (59.4%), 9.9 sq. km (14.6%), and 8.1 sq. km (11.9%) of bare land were converted into built-up, urban farmland, and vegetation respectively. Similarly, 50.5 sq.km (48.1%), 2.5 sq.km (2.3%) and 1.5 sq.km (1.5%) of vegetation was converted in to built-up, urban farmland and bare land cover categories respectively. The result further reveals that the built-up land use category was converted into vegetation, bare land, and urban farmland by 22.2 sq. km (10.5%), 3.7 sq. km (1.8%), and 2.9 sq. km (1.8%) respectively.

Whereas, 182.2 sq.km (86.0%) of built-up, 49.5 sq.km (47.2%) of vegetation, 41.0 sq.km (29.1%) of urban farmland and 8.5 sq.km (11.9%) of bare land remained unaltered during the last 15 years.

Table 4. 5: *Land use/cover conversion matrix during 2006, 2016 and 2021*

Change type	Observed change					
	Between 2006 and 2016		Between 2016 and 2021		Between 2006 and 2021	
	Area (Sq.km)	Area (%)	Area (Sq.km)	Area (%)	Area (Sq.km)	Area (%)
Built-up to Bare land	6.8	3.2	4.7	1.5	3.7	1.8
Built-up (unchanged)	170.8	80.8	271.9	90.3	182.1	86.0
Built-up to Urban farmland	6.9	3.3	5.7	1.9	2.9	1.4
Built-up to Vegetation	26.7	12.6	18.9	6.3	22.2	10.5
Vegetation to Bare land	3.5	3.3	0.8	0.8	1.5	1.5
Vegetation to Built-up	43.8	41.7	26.5	27.8	50.5	48.1
Vegetation to Urban farmland	4.9	4.7	1.3	1.4	2.5	2.3
Vegetation (unchanged)	52.4	49.9	66.5	69.7	49.5	47.2
Urban farmland to Bare land	12.5	8.8	3.4	3.7	7.4	5.3
Urban farmland to Built-up	55.1	38.9	31.4	33.6	75.9	53.7
Urban farmland (unchanged)	63.9	45.3	46.8	50.2	41.0	29.1
Urban farmland to Vegetation	9.2	6.5	5.38	5.8	13.3	9.4
Bare land (unchanged)	12.9	19.1	12.2	33.9	8.5	12.5
Bare land to Built-up	31.1	46.1	18.9	52.3	40.2	59.4
Bare land to Urban farmland	16.3	24.1	2.5	6.9	9.9	14.6
Bare land to Vegetation	7.1	10.5	2.1	5.9	8.1	11.9

Source: *Computed using ArcGIS 10.6.1*

4.3. Land surface temperature validation result

The estimated LST from Landsat 7 ETM+ band 6 and Landsat 8 TIRS band 10 were compared and validated against LST data products of MODIS (MOD11A1) Version 6 daily 1km spatial resolution. A total of 500 random points were generated for each study year and the LST values were extracted from both MODIS LST and estimated LST raster. The validation result demonstrated that 86.6% (433-pixel LST values), 81.4% (407-pixel LST values) and 80.2% (401-pixel LST values) extracted shows a maximum difference of ±2ºC between MODIS LST product and estimated LST during January 2006, 2016, and 2021 respectively.

4.4. Spatiotemporal pattern of land surface temperature

In this study, the Landsat 7 ETM+ thermal band (band 6) was used to retrieve LST during the year 2006. Whereas, Landsat 8 TIRS band 10 was utilized to estimate LST during 2016 and 2021 for the city of Addis Ababa. Table 4.6 shows the minimum, maximum, mean, and standard deviation of LST during the years 2006, 2016, and 2021. The result depicts that the highest minimum temperature was estimated during January 05, 2021, having a minimum LST value of 15.9ºC followed by January 24, 2016, and January 04, 2006, with a minimum LST value of 15.1ºC and

9.6ºC respectively. Similarly, the highest maximum temperature was recorded during January 05, 2021, with a maximum LST value of 37.3ºC. In contrast, the maximum temperature was lower during January 24, 2016, and January 04, 2006, representing a maximum LST value of 34.9ºC and 32.0ºC respectively.

Overall, the mean LST result showed an increasing trend from 2006 to 2016 and 2021 in Addis Ababa. The mean LST value during January 05, 2021, was 28.2ºC which is comparatively higher than 27.2ºC and 25.8ºC on January 24, 2016, and January 04, 2006, respectively. In other words, the average LST value increased by 1.4ºC (between 2006 and 2016), by 1.0ºC (between 2016 and 2021), and by 2.4ºC (between 2006 and 2021).

Table 4. 6: *Descriptive statistics of LST during 2006, 2016 and 2021*

	LST (ºC)				Mean LST difference		
	MIN	**MUX**	**Mean**	**STD**	**2006-2016**	**2016-2021**	**2006-2021**
04 January, 2006	9.6	32.0	25.8	2.6	1.4	1.0	2.4
24 January, 2016	15.1	34.9	27.2	2.5			
05 January, 2021	15.9	37.3	28.2	2.8			

Source: *Computed*

4.5. Land surface temperature variation among LULC classes

The estimated value of LST was extracted using the zonal statistics tool in ArcGIS 10.6.1 software for each land use/cover category. The result presented in Figure 4.2 and Table 4.7 confirmed that there was LST variation among the land use/cover classes in the study area.

Table 4. 7: *Descriptive statistics of LST among LULC Classes during 2006, 2016 and 2021*

Class name	LST (ºC), 2006				LST (ºC), 2016				LST (ºC), 2021			
	Min	**MUX**	**Mean**	**STD**	**Min**	**MUX**	**Mean**	**STD**	**Min**	**MUX**	**Mean**	**STD**
Built-up	16.4	32.0	25.8	2.6	17.2	34.9	27.6	1.6	17.7	36.7	28.6	2.1
Vegetation	9.6	29.9	24.3	3.0	15.1	33.5	25.9	2.9	15.9	35.8	26.0	3.4
Urban farmland	14.0	31.3	26.9	1.8	15.1	34.6	27.9	2.7	16.9	37.0	29.5	2.1
Bare land	13.1	32.0	26.9	1.9	18.9	34.9	28.7	1.8	18.8	37.2	30.1	2.1
Water	11.6	29.9	24.8	2.1	17.1	31.9	25.5	2.2	16.7	34.5	26.0	2.9

Source: *Computed*

Table 4.7 portrays that bare land experienced the highest mean LST during the whole range of the study period having an average LST value of 26.9ºC, 28.7ºC, and 30.1ºC in January 2006, 2016, and 2019 respectively. Urban farmland tends to have the second-highest mean LST of 26.9ºC, 27.9ºC and 29.5ºC in January 2006, 2016, and 2021 respectively. Built-up exhibited the third-highest average LST having mean LST values of 25.8ºC, 27.6ºC, and 28.6ºC during 2006, 2016,

and 2021 respectively. On the other hand, the lowest mean LST was shown by vegetation with a mean LST of 24.3ºC in 2006 and 26.0ºC in 2021. While the mean LST of water slightly lowers that of vegetation (25.5ºC vs. 25.9ºC) during 2016.

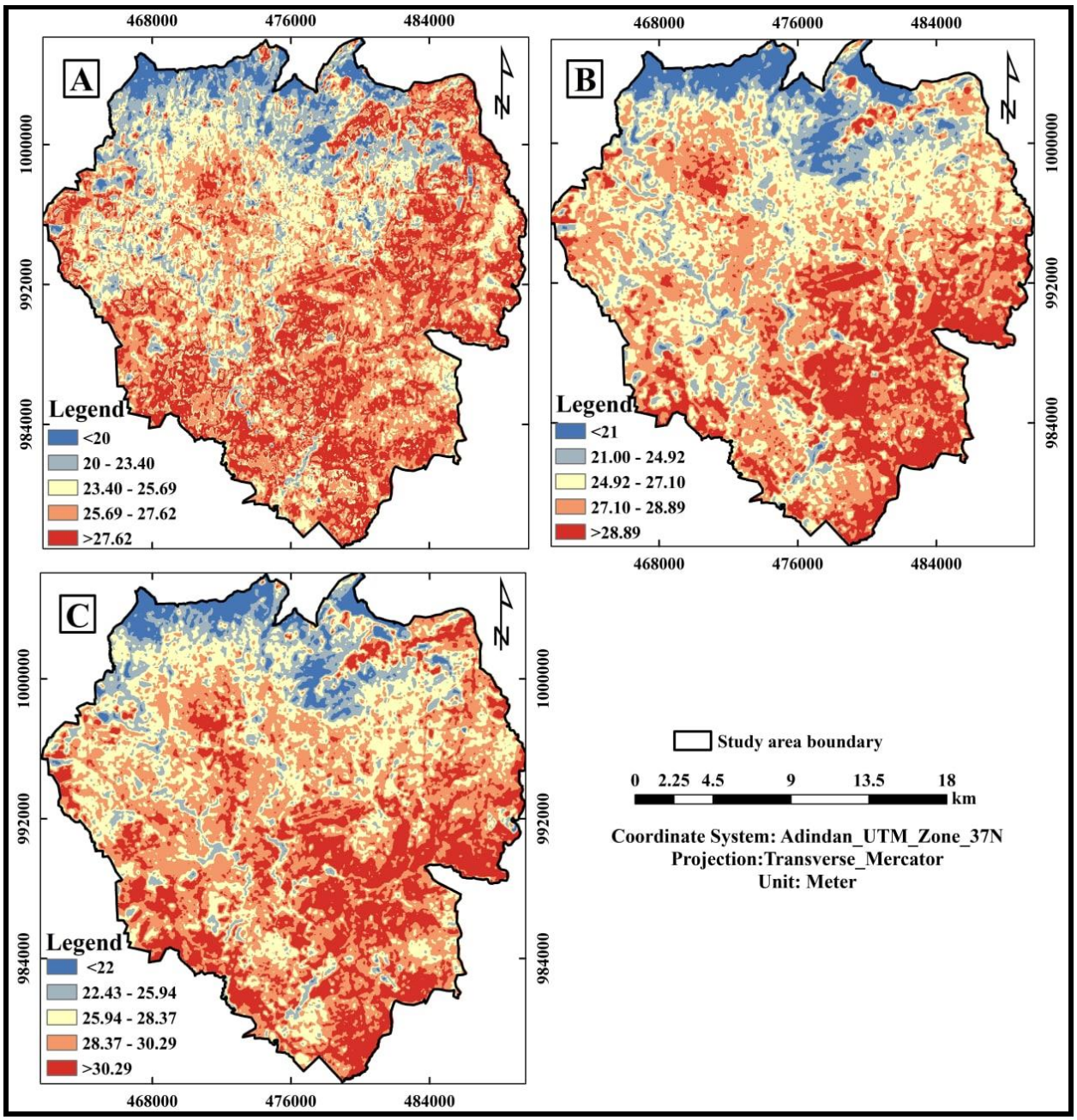

Figure 4. 2: *LST map A) during 2006, B) during 2016 and C) during 2021*

4.6 Statistical analysis

Linear regression analysis was performed for all the study years, with LST as the dependent variable and NDBI, NDVI, MNDWI and altitude as predictor variables using Stata 15 software

(Appendices 1, 2, 3 and 4). Table 4.7 gives the results for Pearson's correlation coefficient (r) and the coefficient of determination (R^2) while the scatter plots are shown in Figures 4.4, 4.6, 4.8 and 4.9. The results of R^2 values during all the study years reveal that NDBI is a better predictor of LST compared to NDVI and MNDWI.

4.6.1 NDVI-LST relationship

Figure 4.3 shows that the maximum NDVI value decreased from 0.60 in 2006 to 0.58 between 2016 and 2021. While minimum NDVI value increased from -0.37 in 2006 to -0.15 and -0.13 in 2016 and 2021 respectively.

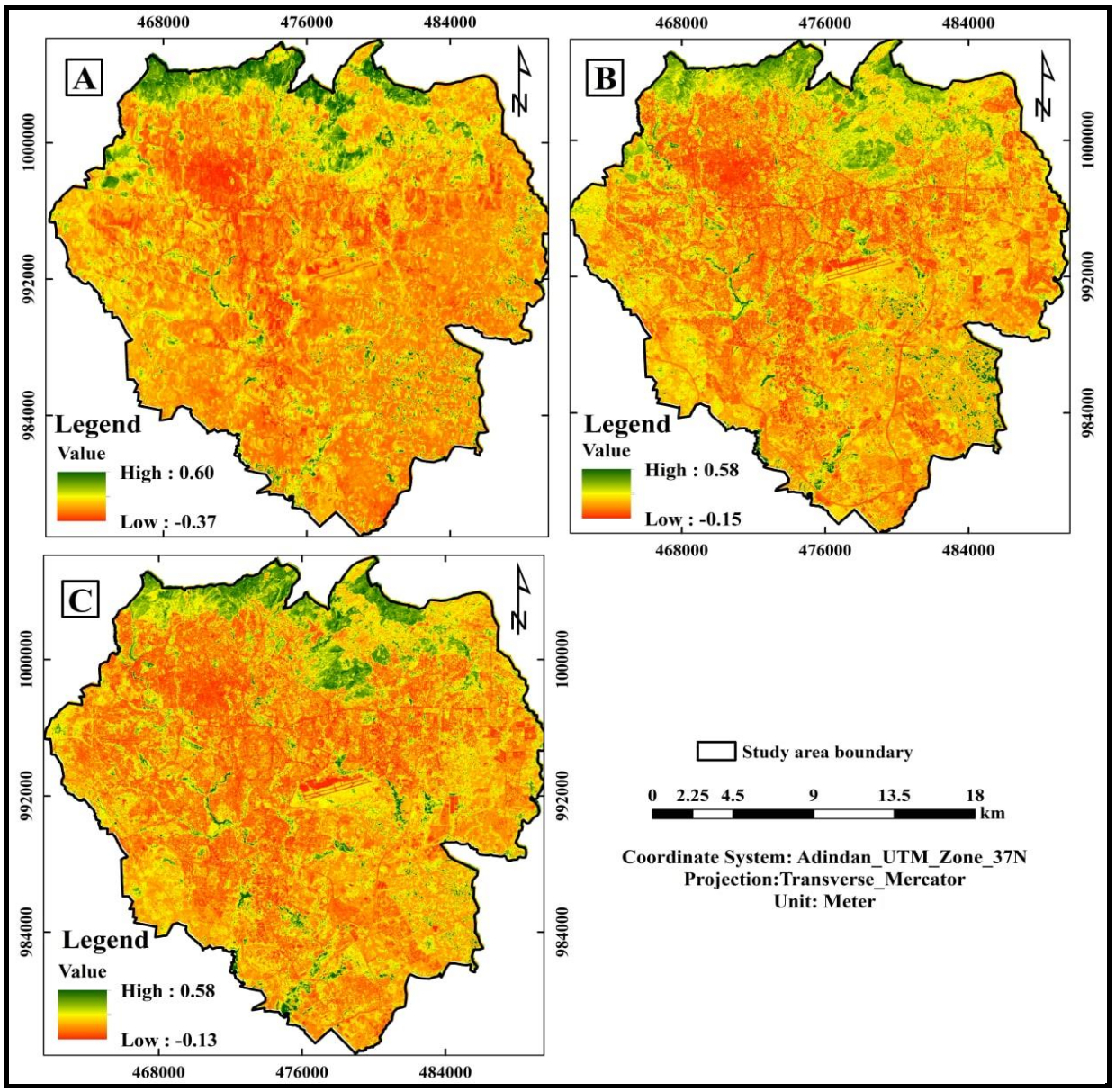

Figure 4. 3: *NDVI map A) during 2006, B) during 2016 and C) during 2021*

The statistical results in Table 4.8 and the scatter plot in Figure 4.4 show a strong negative correlation between NDVI and LST with r values of -0.56, -0.55, and -0.50 during the years 2006, 2016, and 2021 respectively. This means that the lower the NDVI, the higher the LST and vice versa. The R^2 values were found to be 0.31, 0.30, and 0.23 indicating that 31%, 30%, and 23% of the variations in LST were explained by NDVI (vegetation cover) in 2006, 2016, and 2021 respectively.

Table 4. 8: *R^2 and r values of LST with NDVI, NDBI, MNDWI and altitude in 2006, 2016 and 2021*

Year	NDVI		NDBI		MNDWI		Altitude	
	r	**R2**	**r**	**R2**	**r**	**R2**	r	**R2**
2006	-0.56	0.31	0.57	0.33	-0.27	0.07	-0.39	0.16
2016	-0.55	0.3	0.63	0.4	-0.29	0.08	-0.47	0.22
2021	-0.5	0.23	0.53	0.29	-0.24	0.06	-0.31	0.08

Source: *Computed*

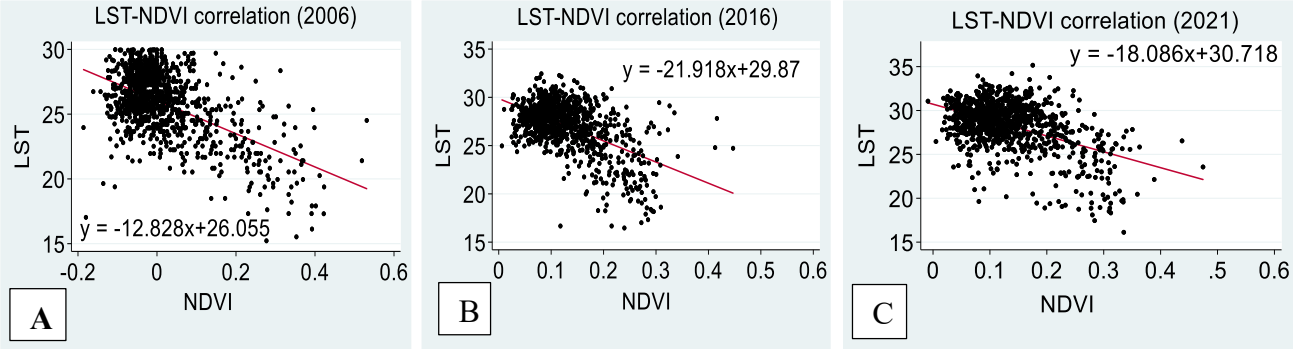

Figure 4. 4: *Scatter plots of NDVI and LST A) in 2006, B) in 2016 and C) in 2021*

4.6.2 NDBI-LST relationship

It is evident from Figure 4.5 that the maximum NDBI values were found to be 0.48, 0.34, and 0.30 during 2006, 2016, and 2021 respectively. Whereas the minimum NDBI values were -0.48, -0.43, and -0.45 for the years 2006, 2016, and 2021 respectively. The linear regression carried out indicated that there was a strong positive relationship between NDBI and LST with a correlation coefficient of r =0.57, 0.63, and 0.53 in 2006, 2016, and 2021 respectively (Table 4.8). The result also portrays that the coefficient determination (R^2) value was the highest during 2016 (0.40) and reduced to 0.33 and 0.29 in 2006 and 2021 respectively. In other words, NDBI contributed by 40%, 33%, and 29% in LST variation during the respective years 2006, 2016, and 2021.

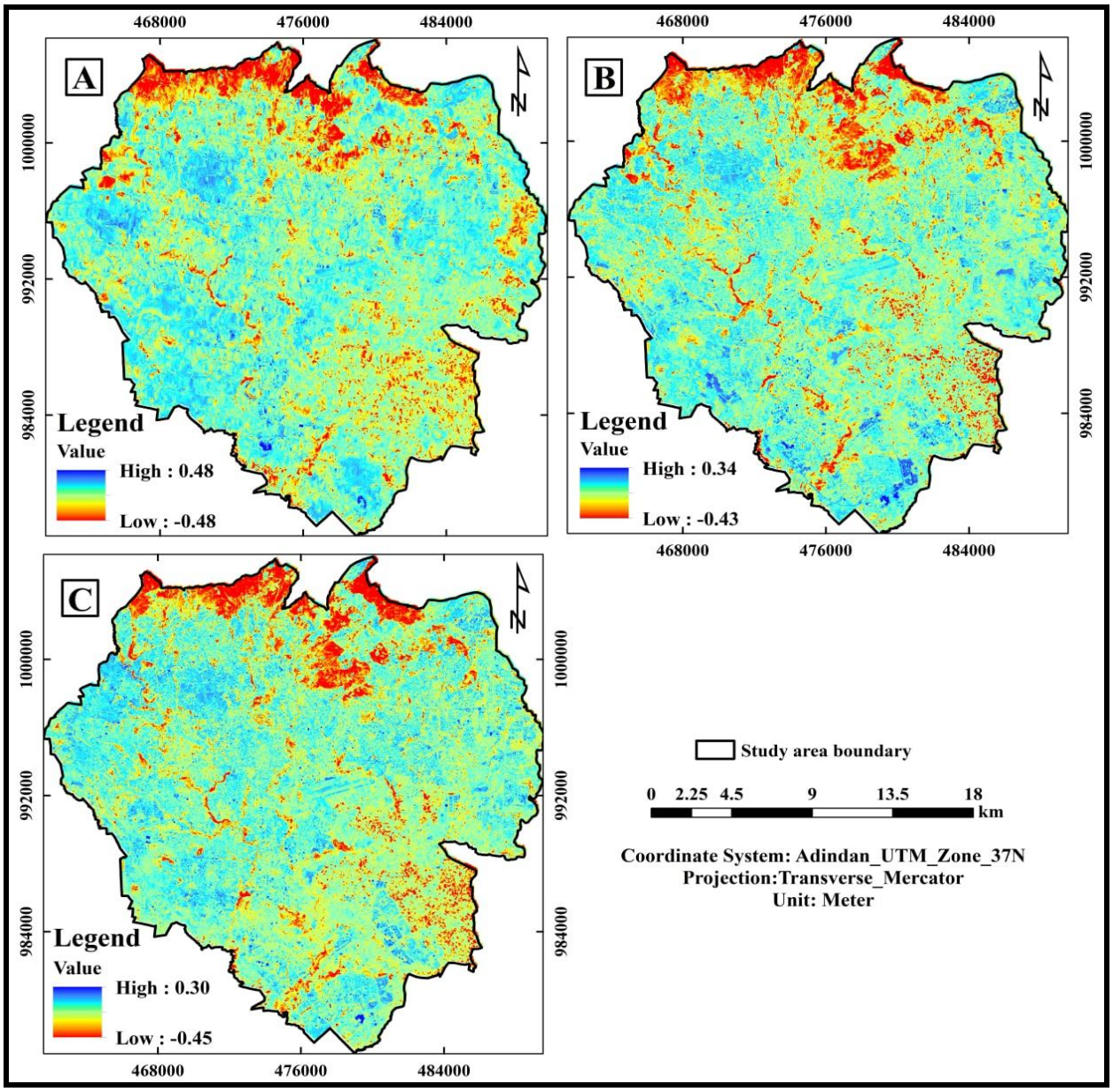

Figure 4. 5: *NDBI map A) during 2006, B) during 2016 and C) during 2021*

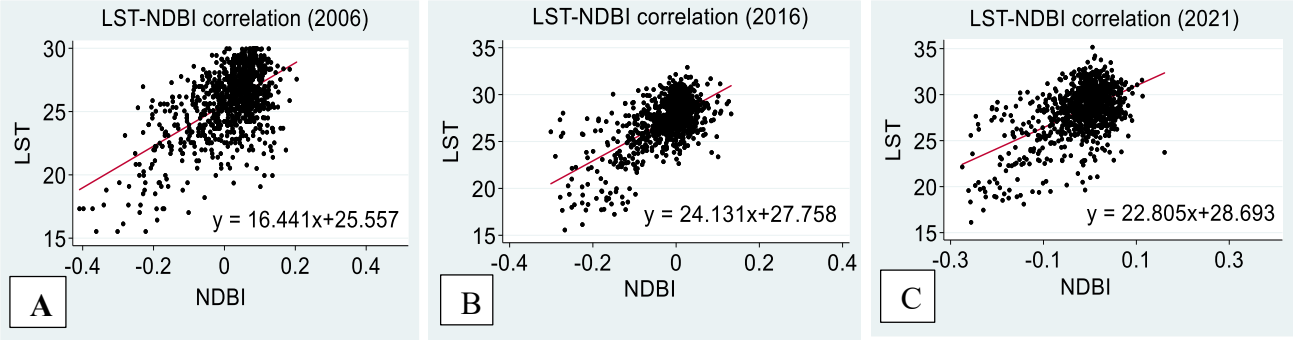

Figure 4. 6: *Scatter plots of LST and NDBI A) in 2006, B) in 2016 and C) in 2021*

4.6.3 MNDWI-LST relationship

Figure 4.7 illustrates that the MNDWI value ranges from -0.54 to 0.59 in 2006; -0.45 to 0.27 in 2016; and -0.47 to 0.20 in 2021. The Pearson's correlation results presented in table 4.8 and Figure 4.8 shows a weak negative association between MNDWI and LST with r = -0.27, -0.29, and -0.24 during 2006, 2016, and 2021 respectively.

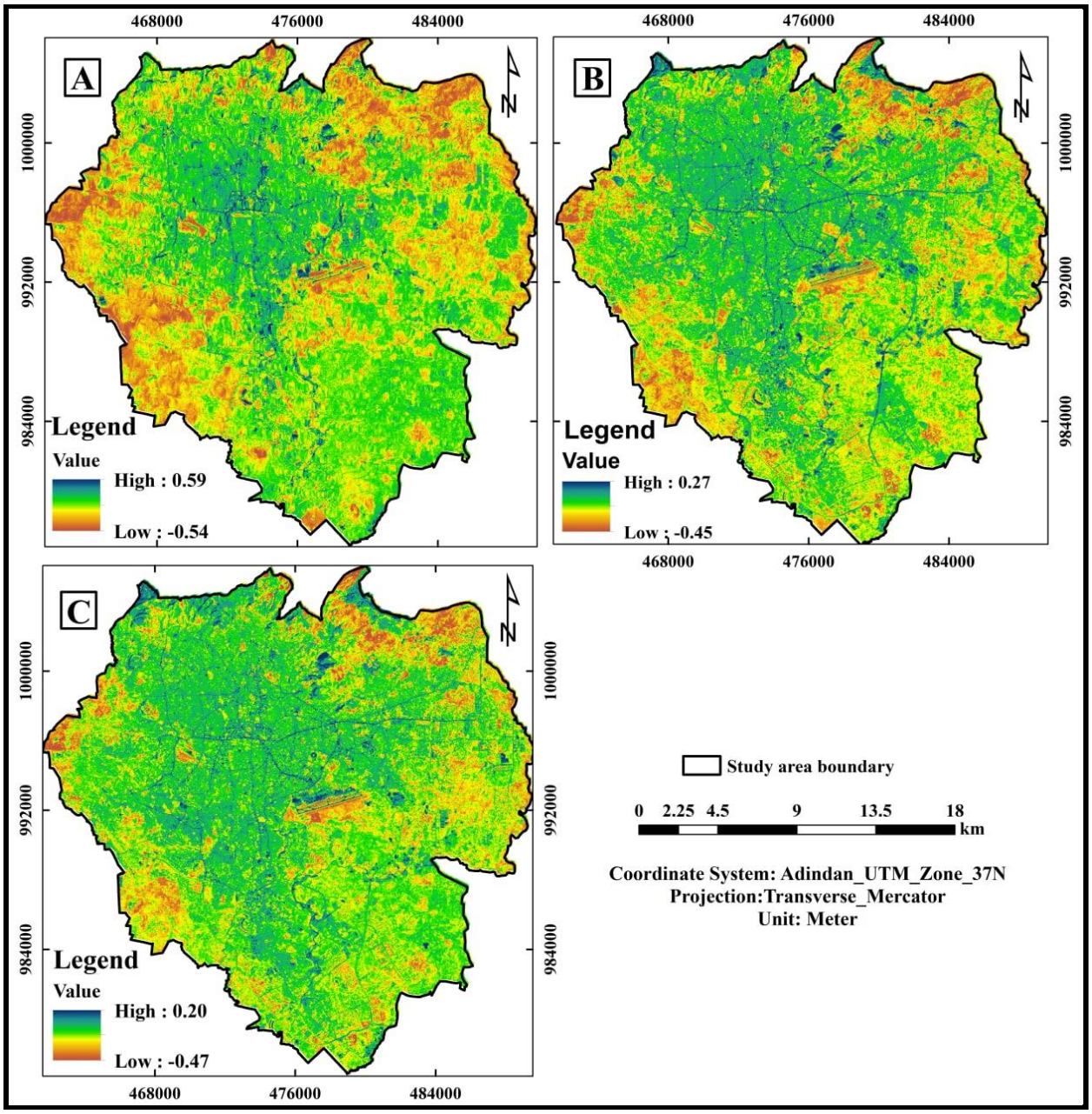

Figure 4. 7: *MNDWI map A) during 2006, B) during 2016 and C) during 2021*

The R^2 values were found to be 0.07, 0.08, and 0.06, meaning that LST was influenced by urban blue landscapes (urban surface water) with an estimate of 7%, 8%, and 6% variations during 2006, 2016, and 2021 respectively (Table 4.8).

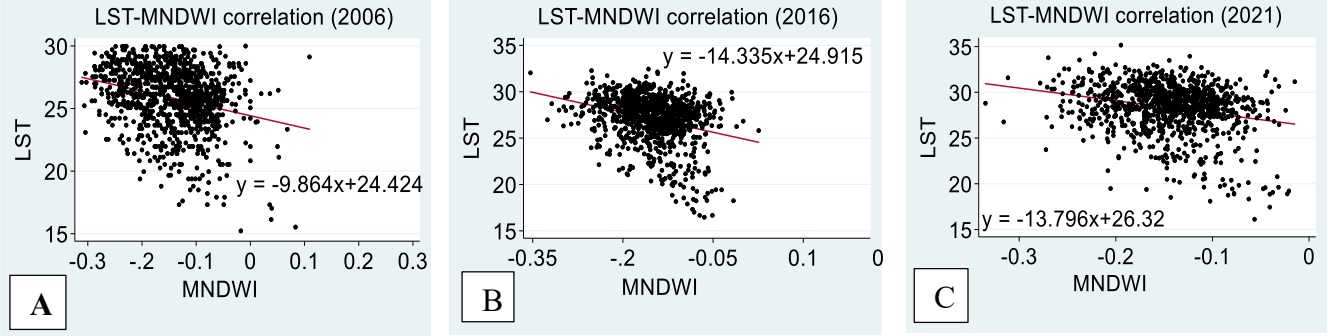

Figure 4. 8: *Scatter plots of LST and MNDWI A) in 2006, B) in 2016 and C) in 2021*

4.6.4 Altitude-LST relationship

The model values for Pearson correlation coefficient (r) were found to be -0.39, -0.47 and -0.31 in 2006, 2016 and 2021 indicating a moderate negative relationship between altitude and LST. On the other hand, R^2 values became 0.16, 0.22 and 0.08 in 2006, 2016 and 2021 respectively. This means that 16%, 22% and 8% of the variations in LST were explained by altitude during the years 2006, 2016 and 2021 respectively.

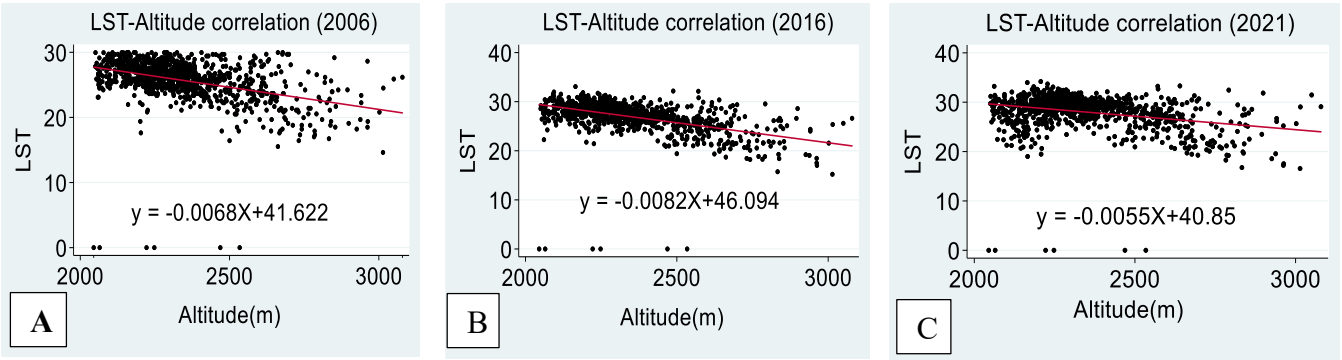

Figure 4.9: *Scatter plots of LST and Altitude A) in 2006, B) in 2016 and C) in 2021*

CHAPTER FIVE

5. DISCUSSIONS

The image classification, which was carried out by implementing Object-based Image Analysis (OBIA) identified 5 major land use/land cover classes in the study area. These are built-up, vegetation, urban farmland, bare land, and water. Acceptable accuracy results were attained for overall accuracy (93%, 94%, and 95 %) and Cohen's kappa coefficient (91%, 92%, and 93%) during 2006, 2016, and 2021 respectively (Tables 4.1-4.3). Therefore, this indicates that there is a high level of agreement between the classified image and the ground truth, suggesting that it is possible to use the result for further analysis. These accuracy results are in good agreement with similar studies conducted in the country and elsewhere (Binyam Tesfaw et al., 2014; Gülçin and Akpinar, 2018).

5.1 Land use and land cover dynamics

The LULC change analysis indicated that the study area has experienced a noticeable land use/cover change over the past 15 years both spatially and temporally. Overall, in all the study periods the built-up land cover class experienced a rapid expansion at the expense of vegetation, urban farmland, and bare land. In contrast, in general, urban farmland, urban green landscapes, and bare land have shrunken in aerial extent during the last 15 years. This has resulted due to the unplanned and uncontrolled city urbanization along with population pressure. These results confirm the research results and conclusions of several previous studies conducted in the city (Rosa Assaye et al., 2015; Mathias Tesfaye and Tebarek Lika, 2017; Ermiayas Teferi and Hiwot Abreha, 2017; Simwanda et al., 2019).

However, the urban green landscapes showed a very slight increase between 2016 and 2021. This is due to the recent green interventions like the green legacy campaign and beautifying sheger/Addis Ababa project as reported in an earlier study by Biruk Terrefe, (2020). On the other hand, water remains relatively unaltered in aerial coverage and holds the least share of the LULC in the city during the years 2006 to 2021. Figure 4.1 reveals the city is mainly expanding towards the South, East, and West directions instead of North which is steep and densely vegetated (Rosa Assaye et al., 2015).

5.2 Land use/Land cover conversion matrix

The land use and land cover transformation detected by the conversion matrix depicts that the city experienced a multidimensional change between different land-use classes. As seen in Table 4.5, most of the bare land (59.4%), urban farmland (53.7%), and urban green (48.1%) were transformed into built-up between the study period 2006 and 2021. Mathias Tesfaye and Tebarek Lika, (2017) conducted research to assess the pace, extent, and pattern of urbanization and its impact on urban-green areas in the Bole sub-city of Addis Ababa. Their result showed a similar pattern of LULC transformation among the land use/cover classes. On the other hand, the largest lost share of the built-up goes to the urban green landscape (10.5%) compared to the conversion of built-up to other land use classes between the years 2006 and 2021. This implies that the urban redevelopment and river buffer projects like beautifying Sheger and associated relocation programs which demolished settlements have contributed to the conversion of built-up into vegetation. This is evident in areas like Arat killo, Lideta, Kirkos (behind St, Estfanos church), Dejach Wube, etc., where, many upgrading or renewals, and slum improvement activities have been undergoing (Herslund et al., 2017; Mathias Tesfaye and Tebarek Lika, 2017). Another possible reason for this is that, according to the Addis Ababa drainage basin and green areas development office, 2020 during the recent years, large hectares of trees have been planted along the roadsides, street medians, and public squares which shades/ hides the paved surface below the street tree canopies.

5.3 Comparison between model LST and MODIS LST product

To assess the reliability of the LST result derived from thermal bands of Landsat 7 ETM+ (Band 6) and Landsat 8 TIRS (Band 10), LST data products of MODIS (MOD11A1) Version 6 daily 1km spatial resolution was used. The comparison result yielded that 86.6%, 81.4% and 80.2% pixel LST values extracted lied within ±2ºC surface temperature between MODIS LST product and retrieved LST during January 2006, 2016, and 2021 respectively. This validation result is in line with some previous studies (Yosef Mengistu et al., 2017; Srivastava et al., 2009) that found a maximum difference of ±2ºC while comparing MODIS LST product and estimated LST from Landsat 8 TIRS sensor. It should be taken into consideration that there exists a spatial resolution difference between the sensors i.e. 30m for Landsat 7 ETM+ and Landsat 8 TIRS versus 1km for MODIS LST product. Besides, MODIS LST is retrieved using the split-window algorithm on bands 31 and 32 (Wan and Dozier, 1996), while the mono window algorism is utilized in this study. Therefore, the LST differences are normal and anticipated.

5.4 LST trend and spatial variation

The results from this study revealed (Table 4.6) that the average LST has increased progressively during the last fifteen years in the study area. Likewise, the maximum and minimum LST values also showed an increasing trend during the years under study. Similar LST trends have been identified in the study area by the results of previous studies (Ermiyas Teferi and Hiwot Abreha, 2017; Dissanayake et al., 2019).

As it is evident from the maps in Figure 4.2, in its spatial pattern, lower LST values were observed in the Northern part of the city (at foot of Mt. Entoto), along with the river courses and vegetation-covered areas. While most of the southern, eastern, and central parts of the city are relatively characterized by higher LST values. These results are supported by the research findings of Rosa Assaye et al., (2015) and Samson Warkaye et al., (2018) who conducted similar studies in the city. The standard deviation of the 2021 LST exceeds that of 2006 and 2016 implying that the surface temperature exhibited a substantial variation in that specific period.

5.5 LST variation among land use/land cover classes

Table 4.7 portrays the statistic values for the five major land cover classes identified. The result shows that the highest mean LST was observed in bare land with a mean LST value of 26.9ºC in 2006, 28.7ºC in 2016, and 30.1ºC in 2021. Urban farmland experienced the second-highest average LST compared to vegetation and water having a mean LST of 26.9ºC, 27.9ºC, and 29.5ºC in 2006, 2016, and 2021 respectively. These results confirm the findings of earlier studies (Simwanda et al., 2019; Abel Balew and Tesfaye Korme, 2020) who stated that radiation-exposed land or bare soil (farmland without crop) had higher thermal property and radiate energy that is responsible for raising LST.

The built-up mean LST was found to be higher as compared to the mean LST of vegetation and water. This implies that non-evaporating and non-transpiring built-up areas (impervious surfaces) such as residential sites, parking lots, industrial parks and shades, street networks, and other paved surfaces contribute a lot in increasing LST over the area. These results are coincident with the findings of previous studies conducted elsewhere (Abu Bakar et al., 2016; Priyankara et al., 2019). However, in contrast to a previous study (Matiwos Belayhun, 2018) the average LST of built-up tends to be lower as compared to the average LST of urban farmland and bare land. Conversely, the mean LST for vegetation and water classes was lesser compared to other land use/cover classes

throughout the study period. Other scholars (Su et. al, 2011; Ogunjobi et al., 2018; Jovish John et al., 2020) also witnessed that vegetation cover plays a vital role in lowering LST by providing shade and cooling the surrounding via the process of evapotranspiration. Similarly, the urban blue (urban surface water) also has the potential to contribute a cooling effect through the process of evaporation as reported by Wu et al., (2019).

5.6 The relationship of LST with NDVI, NDBI, MNDWI and altitude

In this study, NDVI-LST, NDBI-LST, MNDWI-LST and altitude-LST relationships were investigated using linear regression analysis and the statistical results are presented in Table 4.8. The result showed that NDVI tends to have a strong negative linear relationship with LST in all the study years. This suggests that the higher the vegetation cover the lower the surface temperature and vice versa. These results are supported by the findings of previous studies conducted elsewhere (Sun et al., 2012; Adebowale and Kayode, 2015; Bakar et al., 2016; Hua and Ping, 2018; Mwangi et al., 2018; Malik et al., 2019).

In contrast, the linear regression analysis revealed that the NDBI-LST relationship was found to be strong and positive in 2006, 2016, and 2021. This means that as the coverage and density of built-up areas (impervious surfaces) such as residential sites, parking lots, industrial parks and shades, street networks, and other paved surfaces increases, LST increases (Tyubee and Anyadike, 2015; Bakar et al., 2016; Malik et al., 2019).

The regression analysis also demonstrated that MNDWI has a weak negative correlation with surface temperature in the study area. The weak and indirect relationship between MNDWI and LST indicates that the potential of the urban blue landscapes in affecting LST in the study area is limited as compared to NDVI, MNDWI and altitude. However, this result is different from Sun et al., (2012) and Hua and Ping, (2018) who found a strong negative correlation between MNDWI and LST. The result further shows that moderate negative relationship between altitude and LST suggesting that the higher the altitude the lower the LST and vice versa (Peng et al., 2020).

Furthermore, based on the R^2 values presented in Table 4.8, it is predicted that NDBI and NDVI are the two most important parameters responsible for the variation of LST in the study area compared to altitude and MNDWI.

CHAPTER SIX

6. CONCLUSION AND RECOMMENDATIONS

6.1 Conclusion

This study was mainly focused on mapping effects of urban blue-green landscapes on land surface temperature using a geospatial techniques in the city of Addis Ababa. The study applied the OBIA method for LULC classification and identified five major LULC classes i.e. built-up, vegetation, urban farmland, bare land, and water. The findings of the study revealed that there has been a substantial transformation between the LULC classes in the city since 2006 in Addis Ababa. The built-up area was found to be the most dominant land use/cover class and has shown a considerably expanding trend with an annual growth rate of 4.4% (9.3 sq. km) per year during the last 15 years. On other hand, the area coverage under urban farmland, vegetation (except between 2016 and 2021), and bare land have shrunken continuously and extensively between the study periods 2006-2016, 2016-2021, and 2006 -2021. Between the study periods, 2016 to 2021 vegetation showed a slight increase in area coverage. This is due to the contribution of recent green interventions like the green legacy campaign, river buffer project/ beautifying Sheger project in raising the green landscapes coverage in the city. Whereas, the area covered under the urban surface water remained relatively unaltered for the last 15 years.

While considering the whole range of study periods, the findings from the LULC conversion matrix demonstrated that 75.9 sq. km (53.7%) of urban farmland, 50.5 sq. km (48.1%) of vegetation, and 40.2 sq. km (59.4%) of bare land, was transformed into built-up class. Therefore, it can be concluded that the expansion of built areas such as residential sites, parking lots, industrial parks and shades, street networks, etc. is the most prominent phenomenon and is responsible for the shrinking of urban farmland, bare land, and vegetation coverage in the city since 2006. The spatial analysis result of this study reveals that the city expansion is heading towards the Eastern, Western, and southern parts of the city instead of the North which is characterized by dense vegetation and steep slopes.

Moreover, LST was retrieved from the thermal imageries of Landsat 7 ETM + (band 6) and Landsat 8 TIRS (band 10) using the Mono-Window Algorithm (MWA). The findings indicated that LST varied both spatially and temporally throughout the study periods. The spatial variation was mainly due to the variation of different LULC types in the city. Whereas the changes in the

LULC have contributed to the temporal variation of LST in the city. It was observed that the minimum, maximum and mean LST values showed an increasing trend since 2006. The descriptive statistics for LST were extracted for each land use/cover class to examine how LST varied among the LUL classes. The result showed that the highest mean LST was observed on bare land followed by urban farmland and built-up land use/cover classes throughout the periods of study. It was also observed that the average LST showed an increasing trend among all the LULC classes in the last 15 years.

Therefore, the present study had demonstrated that the state of LULC dynamics during the study period and its potential for modifying LST in the city. The result also revealed the effect of anthropogenic activities, particularly the built-up areas which experienced a drastic change over time as a result of the increase in population and the associated infrastructure development in the city. Hence, the findings of this study have indicated that LULC alteration had contributed to the modification of LST in Addis Ababa during the period.

Furthermore, the relationship of LST against NDVI, NDBI, MNDWI and altitude was examined quantitatively using linear regression analysis at a pixel level. The results for Pearson's coefficient (r) values during all the study years indicate that a strong negative correlation was observed between NDVI and LST meaning that the higher the healthy vegetation cover the lower will be the LST. Unlike NDVI, NDBI showed a strong positive correlation with LST, indicating that the higher coverage of built-up areas such as residential sites, parking lots, industrial parks and shades, street networks, etc., the higher will be the surface heating in the city. MNDWI tends to have a weak negative correlation with LST. Altitude showed a moderate negative relationship with LST. The regression analysis further indicated that the results of Coefficient of determination (R^2) values were found to be the highest for NDBI followed by NDVI, altitude and MNDWI throughout the study period. This implies that NDBI, NDVI and altitude are the three most important parameters to predict LST in the study area compared to MNDWI. Therefore, it can be concluded that built-up area, vegetation cover and altitude plays the most decisive role in the variation of LST in the city compared to urban surface water during the last 15 years.

Lastly, the study witnessed the potential of integrating remote sensing, particularly thermal remote sensing and GIS for investigating the urban thermal environment with respect to different LULC classes.

6.2 Recommendations

Based on the findings and conclusions drawn, the following recommendations are suggested:

- This study demonstrated that the drastic growth in urbanization and considerable loss in vegetation cover have contributed a lot to the alteration of the urban thermal environment. Therefore, it is highly recommended that when planning and designing, urban policy-makers and planners should consider diversified green landscapes such as green buildings (urban buildings with vegetation cover on exterior walls and roofs), street greening, small and large parks, green trails for walking/cycling, playing grounds, etc.
- Urban blue-green landscapes should better be planned and designed in such a way that, it could be possible to make adjustments to adapt to changing and forthcoming demands.
- Blue-green development opportunities should be promoted and extended into other sectors and projects like the greening of business areas, schools, shopping areas, residential housing estates, industrial areas, and private green areas and gardens, etc.
- While planning and designing for future blue-green interventions in the city, it would be beneficial to consider the construction of man-made lakes within the green landscapes to strengthen the cooling effect, as was the case in Friendship Square/Park.
- The results of this study were discussed with the focus on the spatiotemporal pattern of LULC dynamics and the consequential LST modification in the city. The author realizes that some other driving forces of LST other than LULC dynamics such as slope, latitude, albedo, etc., were not considered in this study. Therefore, it is recommended that future studies should focus to fill this gap. Moreover, the temporal extent should also be widened to better understand the LULC dynamics and its effect on the LST trend in the city.

References

A. A. Van De Griend & M. Owe. (1993). On the relationship between thermal emissivity and the normalized difference vegetation index for natural surfaces, *International Journal of Remote Sensing*, 14:6, 1119-1131, DOI: 10.1080/01431169308904400

Abel Balew &, Tesfaye Korme. (2020). Monitoring land surface temperature in Bahir Dar city and its surrounding using Landsat images. *The Egyptian Journal of Remote Sensing and Space Science*. 23. 10.1016/j.ejrs.2020.02.001.

Aboyade, O. (2001). Geographic information systems: application in planning and decision-making processes in Nigeria. *Unpublished paper presented at the Environmental and Technological unit in the Development Policy Centre, Ibadan*.

Abu Bakar, Suzana Binti & Pradhan, Biswajeet & Lay, Usman & Abdullahi, Saleh. (2016). Spatial assessment of land surface temperature and land use/land cover in Langkawi Island. IOP Conference Series: *Earth and Environmental Science*. 37. 012064. 10.1088/1755-1315/37/1/012064.

Addis Abba city drainage basin and green areas development office. (2020). Annual report on Green spaces development.

Addis Ababa City Structure Plan. (2017-2027). Draft Final Summary Report [Online] Available at: https://c40productionimages.s3.amazonaws.com/other_uploads/images/2036_Addis_Ababa_Structural_Plan_2017_to_2027.original.pdf?1544193458 Retrieved on November 13, 2020

Adebowale, B. I., & Kayode, S. E. (2015, July). Geospatial assessment of urban expansion and land surface temperature in Akure, Nigeria. In *Proceedings of the ICUC9—9th International Conference on Urban Climate Jointly with 12th Symposium on the Urban Environment, Toulouse, France* (pp. 20-24).

Ahmad, Asmala & Quegan, S. (2012). Analysis of maximum likelihood classification on multispectral data. Applied Mathematical Sciences. 6. 6425-6436.

Akmalov, S., Blanpain, O., & Masson, E. (2017). Study of ecological changes in syrdarya province by using the remote sensing and geobia analysis method. *Irrigation and Melioration*, *2017*(2), 15-19.

Ang Kean Hua & Owi Wei Ping. (2018). The influence of land-use/land-cover changes on land surface temperature: a case study of Kuala Lumpur metropolitan city, *European Journal of Remote Sensing*, 51:1, 1049-1069, DOI: 10.1080/22797254.2018.1542976

Arvanitidis, Paschalis & Lalenis, Konstantinos & Petrakos, George & Psycharis, Yannis. (2009). Economic aspects of urban green space: a survey of perceptions and attitudes. *International Journal of Environmental Technology and Management*. 11. 143-168.

Basudeb Bhatta. (2011). Remote Sensing and GIS. Textbook. – Oxford University Press. Textbook. - Second Edition – 716p.

Bayram Cemil Bilgili and Ercan Gökyer. (2012). Urban Green Space System Planning, Landscape Planning, Dr. Murat Ozyavuz (Ed.), ISBN: 978-953-51-0654-8, In Tech, [Online] Available at: http://www.intechopen.com/books/landscape-planning/urban-green-space-system-planning Retrieved on December 31, 2020

Belaybeh Bufebo & Eyasu Elias. (2021). Land Use/Land Cover Change and Its Driving Forces in Shenkolla Watershed, South Central Ethiopia. *The Scientific World Journal*, *2021*.

Binyam Alemu, Efrem Garedew, Zewudu Eshetu, & Habtemariam Kassa. (2015). Land use and land cover changes and associated driving forces in northwestern lowlands of Ethiopia. *International research journal of agricultural science and soil science*, *5*(1), 28-44.

Binyam Tesfaw & Maeda, Eduardo & Hurskainen, Pekka & Pellikka, Petri. (2014). Object-based image analysis for distinguishing indigenous and exotic forests in coffee production areas of Ethiopia. Applied Geomatics. 10.1007/s12518-014-0136-x.

Biruk Terrefe. (2020). Urban layers of political rupture: the 'new' politics of Addis Ababa's megaprojects, *Journal of Eastern African Studies*, 14:3, 375-395, DOI: 10.1080/17531055.2020.1774705

Bisquert, Mar & Bégué, Agnès & Deshayes, Michel. (2014). Object-based delineation of homogeneous landscape units at regional scale based on MODIS time series. *International Journal of Applied Earth Observation and Geoinformation*. 47. 72-82.

Bobrinskaya. M., (2012). Remote Sensing for Analysis of Relationships between the Land cover and Land Surface Temperature in Ten Megacities.

Byrne, Jason & Sipe, Neil. (2010). Green and open space planning for urban consolidation – A review of the literature and best practice. Urban Research Program.

Calaza, Pedro & Carinanos, Paloma & O'Brien, Liz & Calfapietra, Carlo. (2017). The Cost of Greening: Disservices of Urban Trees. 10.1007/978-3-319-50280-9_9.

Chavez Jr PS. (1988). An improved dark-object subtraction technique for atmospheric scattering correction of multispectral data. *Remote sensing of environment* 24(3):459-479. DOI: https://doi.org/10.1016/0034- 4257(88)90019-3

Craig m. Trotter. (1991). Remotely-sensed data as an information source for geographical information systems in natural resource management a review, *International Journal of Geographical Information Systems*, 5:2, 225-239, DOI: 10.1080/02693799108927845

CSA. (2007). Summary and Statistical Report of the 2007 population and Housing Census of Ethiopia. Addis Ababa, Ethiopia

CSA. (2017). Population Projection of Ethiopia for All Regions at Wereda Level from 2014 – 2017. Addis Ababa, Ethiopia

D. Pozo Vázquez, F.J. Olmo Reyes, L. Alados Arboledas. (1997). A comparative study of algorithms for estimating land surface temperature from AVHRR Data, *Remote Sensing of Environment*, Volume 62, Issue 3, Pages 215-222, ISSN 0034-4257, https://doi.org/10.1016/S0034-4257(97)00091-6.

De La Barrera, F., Reyes-Paecke, S., Banzhaf, E. (2016). Indicators for green spaces in contrasting urban settings. Ecological Indicators, 62, 212–219

Dissanayake, D. M. S. L. B., Morimoto, T., Murayama, Y., & Ranagalage, M. (2019). Impact of landscape structure on the variation of land surface temperature in the sub-Saharan region: A case study of Addis Ababa using Landsat data (1986–2016). *Sustainability*, *11*(8), 2257.

Dunnet, N., Swanwick, C., Wooley, H. (2002). Improving Urban Parks, Play Areas and Open Spaces. 217 pp., University of Sheffield. Queen's Printer. London.

Easkey Britton, Gesche Kindermann, Christine Domegan, Caitriona Carlin. (2020). Blue care: a systematic review of blue space interventions for health and wellbeing, *Health Promotion International*, Volume 35, Issue 1, Pages 50–69, https://doi.org/10.1093/heapro/day103

Ebrahim Esa Hassen & Mohammed Assen. (2017). Land use/cover dynamics and its drivers in Gelda catchment, Lake Tana watershed, Ethiopia. *Environmental Systems Research*. 6. 10.1186/s40068-017-0081-x.

Elif Sertel & Ugur Alganci. (2016). Comparison of pixel and object-based classification for burned area mapping using SPOT-6 images, Geomatics, Natural Hazards and Risk, 7:4, 1198-1206, DOI: 10.1080/19475705.2015.1050608

Enderle, D.I., & Weih, R.C. (2005). Integrating Supervised and Unsupervised Classification Methods to Develop a More Accurate Land Cover Classification. *Journal of the Arkansas Academy of Science, 59*, 65-73.

Epstein, J., Payne, K., and Kramer, E. (2002). Techniques for mapping suburban sprawl. *Photogr. Eng. Remote Sens.* 63, 913–918.

Ermias Teferi & Hiwot Abreha. (2017). Urban Heat Island Effect of Addis Ababa City: Implications of Urban Green Spaces for Climate Change Adaptation. 10.1007/978-3-319-49520-0_33.

Filgueiras, R., Mantovani, E. C., Althoff, D., Dias, S. H., & Cunha, F. F. D. (2019). Sensitivity of evapotranspiration estimated by orbital images under influence of surface temperature. *Engenharia Agrícola*, *39*(SPE), 23-32.

Forest Research. (2021). What is greenspace/green infrastructure (GI)? Types of greenspace [Online] Available at: https://www.forestresearch.gov.uk/tools-and-resources/urban-regeneration-and-greenspace-partnership/greenspace-in-practice/types-of-greenspace/ Retrieved on January 9, 2021

Gašparović, M. (2020). Urban growth pattern detection and analysis. In Urban Ecology (pp. 35-48). Elsevier.

Gledhill, David & James, Philip. (2008). Rethinking Urban Blue Spaces from a Landscape Perspective: Species, scale and the human element. Band. 42. 151-164.

Guha, Subhanil & Govil, Himanshu & Dey, Anindita & Gill, Neetu. (2018). Analytical study of land surface temperature with NDVI and NDBI using Landsat 8 OLI and TIRS data in Florence and Naples city, Italy. *European Journal of Remote Sensing*. 51. 667-678. 10.1080/22797254.2018.1474494.

Gülçin, Derya & Akpinar, Abdullah. (2018). Mapping Urban Green Spaces Based on an Object-Oriented Approach. *Bilge International Journal of Science and Technology Research*. 2. 71-81. 10.30516/bilgesci.486893.

Gunawardena, Kan-Chane & Wells, Mike & Kershaw, Tristan. (2017). Utilizing green and bluespace to mitigate urban heat island intensity. *Science of The Total Environment*. 584-585. 1040-1055. 10.1016/j.scitotenv.2017.01.158.

GUO, Q., KELLY, M., GONG, P. and LIU, D. (2007). An object-based classification approach in mapping tree mortality using high spatial resolution imagery. *GIS science & remote sensing*, 44, pp. 24–47.

Hanqiu Xu. (2006): Modification of normalized difference water index (NDWI) to enhance open water features in remotely sensed imagery, *International Journal of Remote Sensing*, 27:14, 3025-3033

Haq, S. M. A. (2011). Urban green spaces and an integrative approach to sustainable environment. *Journal of Environmental Protection*, 2(5): 601-608.

Herslund, Lise & Backhaus, Antje & Fryd, Ole & Jørgensen, Gertrud & Jensen, Marina & Limbumba, Tatu & Liu, Li & Mguni, Patience & Mkupasi, Martha & Habtemariam, Liku & Yeshitela, Kumelachew. (2017). Conditions and opportunities for green infrastructure – Aiming for green, water-resilient cities in Addis Ababa and Dar es Salaam. *Landscape and Urban Planning*. 180. 10.1016/j.landurbplan.2016.10.008.

Hillel, D., & Hatfield, J. L. (Eds.). (2005). *Encyclopedia of Soils in the Environment* (Vol. 3). Amsterdam: Elsevier.

Jennings V., Browning M.H.E.M., Rigolon A. (2019) Friend or Foe? An Overview of the Services and Disservices from Urban Green Spaces. In: Urban Green Spaces. *Springer Briefs in Geography*. Springer, Cham. https://doi.org/10.1007/978-3-030-10469-6_2

Jiménez-Muñoz, J.C.; Cristóbal, J.; Sobrino, J.A.; Sòria, G.; Ninyerola, M.; Pons, X. (2009). Revision of the Single-Channel Algorithm for Land Surface Temperature Retrieval from Landsat Thermal-Infrared Data. *IEEE Trans. Geosci. Remote Sens. 47*, 339–349.

Jimenez-Munoz, Juan-Carlos & Sobrino, Jose & Skokovic, Drazen & Mattar, Cristian & Cristóbal Rosselló, Jordi. (2014). Land Surface Temperature Retrieval Methods from Landsat-8 Thermal Infrared Sensor Data. *Geoscience and Remote Sensing Letters*, IEEE. 11. 1840-1843. 10.1109/LGRS.2014.2312032.

Jimenez-Munoz, Juan-Carlos & Sobrino, Jose. (2003). A generalized single-channel method for retrieving land surface temperature from remote sensing data (vol 109, art no D08112, 2004). *Journal of Geophysical Research*. 108. 10.1029/2003JD003480.

Jimenez-Munoz, Juan-Carlos & Sobrino, Jose. (2008). Split-Window Coefficients for Land Surface Temperature Retrieval from Low-Resolution Thermal Infrared Sensors. *Geoscience and Remote Sensing Letters*, IEEE. 5. 806 - 809. 10.1109/LGRS.2008.200163

Jose G V H, Karina P, Patricia H. (2018). Urban Green Spaces as a Component of an Ecosystem Functions, Services, Users, Community **027** Involvement, initiatives, and Actions. *Int J Environ Sci Nat* Res. 8(1): 555730. DOI: 10.19080/IJESNR.2018.08.555730.

Jovish John, G. Bindu, B. Srimuruganandam, Abhinav Wadhwa. (2020): Land use/land cover and land surface temperature analysis in Wayanad district, India, using satellite imagery, Annals of GIS, DOI: 10.1080/19475683.2020.1733662

Käfer, Pâmela Suélen, Rolim, Silvia Beatriz Alves, Diaz, Lucas Ribeiro, Rocha, Nájila Souza da, Iglesias, María Luján, & Rex, Franciel Eduardo. (2020). Comparative Analysis of Split-Window and Single-Channel Algorithms for Land Surface Temperature Retrieval of a Pseudo-invariant Target. *Boletim de Ciências Geodésicas*, *26*(2), e2020008. .https://doi.org/10.1590/s1982-21702020000200008

Kumari, Babita & Tayyab, Mohammad & Shahfahad & Salman, & Mallick, Javed & Khan, Mohammad Firoz & Rahman, Atiqur. (2018). Satellite-Driven Land Surface Temperature (LST) Using Landsat 5, 7 (TM/ETM+ SLC) and Landsat 8 (OLI/TIRS) Data and Its Association with Built-Up and Green Cover Over Urban Delhi, India. 1. 63-78. 10.1007/s41976-018-0004-2.

Kumelachew Yeshitela, Liberatus Mrema, Alazar Assefa and Simon Mpyanga. (2015). Water Resilient Cities in Africa: Green area typologies and mapping of green structures in Addis Ababa and Dar es Salaam. [Online] Available at:

https://ign.ku.dk/english/research/landscapearchitectureplanning/landscapetechnology/water-green-africa/projectpublications/filer/Report1-WP1-GREEN-AREA-TYPOLOGIES-AND-MAPPING-OF-GREEN-STRUCTURES.pdf Retrieved on January 06, 2021.

Lee, Andrew & Jordan, Hannah & Horsley, Jason. (2015). Value of urban green spaces in promoting healthy living and wellbeing: Prospects for planning. Risk Management and Health care Policy. 8. 131. 10.2147/RMHP.S61654.

Lillesand, T., Kiefer, R. W., & Chipman, J. (2015). Remote sensing and image interpretation. John Wiley & Sons.

Liu, Desheng & Xia, Fan. (2010). Assessing object-based classification: Advantages and limitations. *Remote Sensing Letters*. 1. 187-194. 10.1080/01431161003743173.

Malik, M. S., Shukla, J. P., & Mishra, S. (2019). Relationship of LST, NDBI, and NDVI using Landsat-8 data in Kandaihimmat watershed, Hoshangabad, India.

Mathias Tesfaye Abebe & Tebarek Lika Megento. (2016). The city of Addis Ababa from 'forest city' to 'urban heat island': Assessment of urban green space dynamics. *Journal of Urban and Environmental Engineering*. 10. 254-262. 10.4090/juee. 2016. V10n2.254262.

Mathias Tesfaye Abebe & Tebarek Lika Megento. (2017). Urban green space development using GIS-based multi-criteria analysis in Addis Ababa metropolis. *Applied Geomatics, 9*, 247-261.

Matiwos Belayhun Haylemariyam. (2018). Detection of Land Surface Temperature in Relation to Land Use Land Cover Change: Dire Dawa City, Ethiopia. *J Remote Sens GIS 7*: 245. doi:10.4172/2469-4134.1000245

McMillin L.M. (1975). Estimation of sea surface temperatures from two infrared window measurements with different absorption. *J. Geophys.* Res.; 80:80–82. Doi: 10.1029/JC080i036p05113.

Melissa Haeffner, Douglas Jackson-Smith, Martin Buchert, Jordan Risley. (2017). Accessing blue spaces: Social and geographic factors structuring familiarity with, use of, and appreciation of urban waterways, Landscape and Urban Planning, 167, 136-146, ISSN 0169-2046, https://doi.org/10.1016/j.landurbplan.2017.06.008.

Mwangi, P.W., Karanja, F.N. and Kamau, P.K. (2018). Analysis of the Relationship between Land Surface Temperature and Vegetation and Built-Up Indices in Upper-Hill, Nairobi. *Journal of Geoscience and Environment Protection*, 6, 1-16.

Naeem, Shahid; Cao, Chunxiang; Qazi, Waqas A.; Zamani, Mehdi; Wei, Chen; Acharya, Bipin K.; Rehman, Asid U. (2018). "Studying the Association between Green Space Characteristics and Land Surface Temperature for Sustainable Urban Environments: An Analysis of Beijing and Islamabad" *ISPRS Int. J. Geo-Inf.* 7, no. 2: 38. https://doi.org/10.3390/ijgi7020038

NASA-National Aeronautics and Space Administration, (2000). Land Surface Temperature [Online] Availableat:https://earthobservatory.nasa.gov/globalmaps/MOD_LSTD_M#:~:text=Land%20surface%20temperature%20is%20how,the%20atmosphere%20to%20the%20ground. Retrieved on October 30, 2020.

Ogunjobi KO, Adamu Y, Akinsanola AA, Orimoloye IR. (2018). Spatiotemporal analysis of land use dynamics and its potential indications on land surface temperature in Sokoto Metropolis, Nigeria. R. Soc. open sci. 5:180661.

Panduro, Toke & Veie, Kathrine. (2013). Classification and valuation of urban green spaces—A hedonic house price valuation. Landscape and Urban Planning. 120. 119–128. 10.1016/j.landurbplan.2013.08.009.

Pataki, Diane & Carreiro, Margaret & Cherrier, Jennifer & Grulke, Nancy & Jennings, Viniece & Pincetl, Stephanie & Pouyat, Richard & Whitlow, Thomas & Zipperer, Wayne. (2010). Coupling biogeochemical cycles in urban environments: ecosystem services, green solutions, and misconceptions. *Frontiers in Ecology and the Environment*. 9. 27-36. 10.2307/41149674.

Patel, S.K., Verma, P., Singh, G.S. (2019). Agricultural growth and land use land cover change in peri-urban India. *Environmental Monitoring and Assessment* 191 (9), 600.

Pauleit, Stephan & Hansen, Rieke & Rall, Emily & Zölch, Teresa & Andersson, Erik & Luz, Ana & Száraz, Luca & Tosics, Iván & Vierikko, Kati, (2017). Urban Landscapes and Green Infrastructure. 10.1093/acrefore/9780199389414.013.23.

Peng, Xiaoxue & Wu, Wenyuan & Zheng, Yaoyao & Sun, Jingyi & Hu, Tangao & Wang, Pin. (2020). Correlation analysis of land surface temperature and topographic elements in Hangzhou, China. Scientific Reports. 10. 10451. 10.1038/s41598-020-67423-6.

Priyankara, P., Ranagalage, M., Dissanayake, D., Morimoto, T., Murayama, Y. (2019). Spatial Process of Surface Urban Heat Island in Rapidly Growing Seoul Metropolitan Area for Sustainable Urban Planning Using Landsat Data (1996– 2017). Climate 7.

Qin, Zhihao & Karnieli, Arnon & Berliner, Pedro. (2010). A Mono-Window Algorithm for Retrieving Land Surface Temperature from Landsat TM data and its Application to the Israel-Egypt Border Region. *International Journal of Remote Sensing*. 22. 3719-3746. 10.1080/01431160010006971.

Radek Dušek & Renata Popelková. (2019). Water in most important towns of the Czech Republic, Journal of Maps, 15:2, 425-435, DOI: 10.1080/17445647.2019.1601136

Rajan KS, Ramachandra TV. (2013). Land Surface Temperature Responses to Land Use Land Cover Dynamics. Geoinfor Geostat An Overview 1:4. doi:10.4172/2327-4581.1000112. 10.4172/2327-.

Rakhshandehroo, Mehdi & Afshin, Sahrakar & Mohd Yusof, Mohd Johari. (2017). Terminology of Urban Open and Green Spaces.

Rongali, Gopinadh & Keshari, A.K. & Gosain, A. & Khosa, Rakesh. (2018). Split-Window Algorithm for Retrieval of Land Surface Temperature Using Landsat 8 Thermal Infrared Data. *Journal of Geovisualization and Spatial Analysis*. 2. 10.1007/s41651-018-0021-y.

Rongali, Gopinadh & Keshari, A.K. & Gosain, Ashvani & Khosa, Rakesh. (2018). A Mono-Window Algorithm for Land Surface Temperature Estimation from Landsat 8 Thermal Infrared Sensor Data: A Case Study of the Beas River Basin, India. *Pertanika Journal of Science and Technology.* 26.

Rosa Assaye, K.V. Suryabhagavan and M. Balakrishnan. (2015). Geo-Spatial Approach for Urban Green Space and Environmental Quality: A case study in Addis Ababa. M.Sc. Thesis. Addis Ababa University.

Rouse, J.W., Haas, R.H., Schell, J.A. and Deering, D.W. (1973). Monitoring Vegetation Systems in the Great Plains with ERTS. 3rd ERTS Symposium, NASA SP-351, Washington DC, 10-14 December 1973, 309-317.

Roy, Dr & Byrne, Jason & Pickering, Catherine. (2012). A systematic quantitative review of urban tree benefits, costs, and assessment methods across cities in different climatic zones. *Urban Forestry & Urban Greening*. 11. 351-363. 10.1016/j.ufug.2012.06.006.

S. M. Labib & Angela Harris. (2018). The potentials of Sentinel-2 and Landsat-8 data in green infrastructure extraction, using object-based image analysis (OBIA) method, *European Journal of Remote Sensing*, 51:1, 231-240, DOI: 10.1080/22797254.2017.1419441

Samson Workaye & Suryabhagavan, Karuturi & Belliethathan, Satishkumar. (2018). Urban Green Areas to Mitigate Urban Heat Island Effect: The Case of Addis Ababa, Ethiopia. *International Journal of Ecology and Environmental Sciences*. 44. 353-367.

SelÃƒÂ§uk, Reis. (2008). Analyzing Land Use/Land Cover Changes Using Remote Sensing and GIS in Rize, North-East Turkey. Sensors. 8. 10.3390/s8106188.

Setturu, Bharath & Rajan, K. & Ramachandra, T V. (2014). Land Surface Temperature Responses to Land Use Land Cover Dynamics. Geoinformatics & Geostatistics: An Overview. Bharath S, Rajan KS, Ramachandra TV (2013) LandSurface Temperature Responses to Land Use Land Cover Dynamics. Geoinfor Geostat An Overview 1:4. doi:10.4172/2327-4581.1000112. 10.4172/2327-.

Simwanda, M.; Ranagalage, M.; Estoque, R.C.; Murayama, Y. (2019). Spatial Analysis of Surface Urban Heat Islands in Four Rapidly Growing African Cities. *Remote Sens.* 2019, 11, 1645.

Simwanda, Matamyo., & Murayama, Yuji. (2018). spatiotemporal patterns of urban land-use change in the rapidly growing city of Lusaka, Zambia: Implications for sustainable urban development. *Sustainable Cities and Society* https://doi.org/10.1016/j.scs.2018.01.039

Statistics Solutions. (2021). Pearson's Correlation Coefficient. [Online] Available at: https://www.statisticssolutions.com/pearsons-correlation-coefficient/ Retrieved on April 06, 2021.

Su,Y. & Huang, G. & Chen, X. & Chen, S. & Li, Z. (2011). Research progress in the eco-environmental effects of urban green spaces. *Shengtai Xuebao/ Acta Ecologica Sinica*. 31. 7287-7300.

Sun, Q., Wu, Z., & Tan, J. (2012). The relationship between land surface temperature and land use/land cover in Guangzhou, China. *Environmental Earth Sciences*, *65*(6), 1687-1694.

Swanwick, Carys & Dunnett, Nigel & Woolley, Helen. (2003). Nature, Role, and Value of Green Space in Towns and Cities: An Overview. Built Environment. 29. 94-106. 10.2148/benv.29.2.94.54467.

Teklit Berhe. (2015). Remote Sensing and GIS-Based Urban Land Suitability Modeling at Parcel Level Using Multicriteria Decision Analysis; A Case Study of Bole Sub City, Addis Ababa, Ethiopia. *Unpublished thesis work*

Tyubee, B. T., & Anyadike, R. N. C. (2015, July). Investigating the effect of land use/land cover on urban surface temperature in Makurdi, Nigeria. In *Proceedings of the ICUC9—9th International Conference on Urban Climate Jointly with 12th Symposium on the Urban Environment, Toulouse, France* (pp. 20-24).

Uça Avcı, Zehra & Karaman, Muhittin & Ozelkan, Emre & Papila, Ibrahim. (2011). A Comparison of Pixel-Based and Object-Based Classification Methods, A Case Study: Istanbul, Turkey.

Ugur Avdan, Gordana Jovanovska. (2016). "Algorithm for Automated Mapping of Land Surface Temperature Using LANDSAT 8 Satellite Data", *Journal of Sensors*, vol. 2016, Article ID 1480307, 8 pages, 2016. https://doi.org/10.1155/2016/480307

UN- HABITAT. (2017). The State of Addis Ababa: The Addis Ababa we Want [Online] Available at: https://unhabitat.org/the-state-of-addis-ababa-2017-the-addis-ababa-we-want Retrieved on October 12, 2020

UN-HABITAT. (2010-2013). The State of African Cities 2010: Governance, Inequality, and Urban Land Markets. Cities, 31, 425–429. Doi: 10.1016/j.cities.2012.07.007

United Nations (Department of Economic and Social Affairs - Population Division. (2014). World Urbanization Prospects: The 2014 Revision Highlights

University of Leeds. (2015). A Brief Guide to the Benefits of Urban Green Spaces [Online] Available at:https://www.euro.who.int/__data/assets/pdf_file/0010/342289/Urban-Green-Spaces_EN_WHO_web3.pdf%3Fua=1 Retrieved on October 23, 2020

USGS. (2001). Percent-Slope Classes to Characterize the Unsaturated Zone in North Carolina. [Online]Available at: https://www2.usgs.gov/water/southatlantic/publications/ofr01495/#metadat.Retrieved on February 16, 2021.

USGS. (2019a). Landsat 7 Data Users Handbook [Online] Available at: **https://www.usgs.gov/core-science-systems/nli/landsat/landsat-7-data-users-handbook** Retrieved on January 10, 2021.

USGS. (2019b). Landsat 8 Data Users Handbook [Online] Available at: https://www.usgs.gov/core-science-systems/nli/landsat/landsat-8-data-users-handbook. Retrieved on April 1, 2021.

USGS. (2021). What is remote sensing and what is it used for? [Online] Available at: https://www.usgs.gov/faqs/what-remote-sensing-and-what-it-used?qt-news_science_products=0#qt-news_science_products Retrieved on January 2021.

Vatseva, R., Kopecká, M., Otahel, J., Rosina, K., Kitev, A., & Genchev, S.E. (2016). Mapping Urban Green Spaces Based on Remote Sensing Data: Case Studies in Bulgaria and Slovakia.

Vert, C.; Gascon, M.; Ranzani, O.; Márquez, S.; Triguero-Mas, M.; Carrasco-Turigas, G.; Arjona, L.; Koch, S.; Llopis, M.; Donaire-Gonzalez, D.; et al. (2020). Physical and mental health effects of repeated short walks in a blue space environment: A randomized crossover study. *Environ. Res.188*, 109812.

Walta TV. (2020). Shegre Park Project. [Online] Available at: https://www.youtube.com/watch?v=tkdovTyx_uM&t=1478s Retrieved on January 10, 2021.

Wan, Z., Dozier, J. A. (1996). A generalized split-window algorithm for retrieving land surface temperature from space. IEEE Trans. *Geosc. Rem. Sens*.34 (4), 892–905,

Wang, Fei & Qin, Zhihao & Caiying, Song & Tu, Lili & Karnieli, Arnon & Zhao, Shuhe. (2015). An Improved Mono-Window Algorithm for Land Surface Temperature Retrieval from Landsat 8 Thermal Infrared Sensor Data. *Remote Sensing*. 7. 4268-4289. 10.3390/rs70404268.

Wang, L., Lu, Y., & Yao, Y. (2019). Comparison of Three Algorithms for the Retrieval of Land Surface Temperature from Landsat 8 Images. *Sensors (Basel, Switzerland)*, *19*(22), 5049. https://doi.org/10.3390/s19225049

Weng Q, Liu H, Lu D. (2007). Assessing the effects of land use and land cover patterns on thermal conditions using landscape metrics in the city of Indianapolis, United States. *Urban Ecosyst*. 10. 203-219. 10.1007/s11252-007-0020-0.

Wichansky PS, Steyaert LT, Walko RL, Weaver CP. (2008). Evaluating the effects of historical land cover change on summertime weather and climate in New Jersey: part I: land cover and surface energy budget changes. *J Geophys Res* 113: D10107.

Witharana, Chandi & Civco, Daniel. (2014). Optimizing multi-resolution segmentation scale using empirical methods: Exploring the sensitivity of the supervised discrepancy measure Euclidean distance 2 (ED2). *ISPRS Journal of Photogrammetry and Remote Sensing*. 10.1016/j.isprsjprs.2013.11.006.

World Agroforestry. (2020). Ethiopia to grow 5 billion trees in the Second Green Legacy Campaign [Online] Available at: https://www.worldagroforestry.org/blog/2020/06/09/ethiopia-grow-5-billion-trees-second-green-legacy-campaign Retrieved on November 13, 2020

World Health Organization (WHO). (2017). Urban Green Spaces: A Brief for Action [Online] Available at: https://www.euro.who.int/__data/assets/pdf_file/0010/342289/Urban-Green-Spaces_EN_WHO_web3.pdf%3Fua=1 Retrieved on January 02, 2021

Wu, C., Li, J., Wang, C., Song, C., Chen, Y., Finka, M., & Rosa, D.L. (2019). Understanding the relationship between urban blue infrastructure and land surface temperature. *The Science of the total environment, 694*, 133742.

Wu, Q.; Li, H.Q.; Wang, R.S.; Paulussen, J.; He, H.; Wang, M.; Wang, B.H.; Wang, Z. (2006). Monitoring and predicting land-use change in Beijing using remote sensing and GIS. *Landscape and Urban Planning*, *78*, 322–333.

Yosef Mengistu Darge & Binyam Tesfaw Hailu & Ameha Atnafu Muluneh & Tesfaye Kidane. (2017). Detection of geothermal anomalies using Landsat 8 TIRS data in Tulu Moye geothermal prospect, Main Ethiopian Rift.

Young, Robert. (2010). Managing municipal green space for ecosystem services. Urban Forestry & Urban Greening - URBAN FOR URBAN GREEN. 9. 313-321. 10.1016/j.ufug.2010.06.007.

Zha, Yong & Gao, Jingqing & Ni, S. (2003). Use of normalized difference built-up index in automatically mapping urban areas from TM imagery. *International Journal of Remote Sensing - INT J REMOTE SENS.* 24. 583-594. 10.1080/01431160304987.

Ziwei Deng, Xiang Zhu, Qingyun He, Lisha Tang. (2019). Land use/land cover classification using time-series Landsat 8 images in a heavily urbanized area, *Advances in Space Research*, Volume 63, Issue 7,2019, Pages 2144-2154 https://,doi.org/10.1016/j.asr.2018.12.005.

Appendices

Appendix 1: Regression analysis between NDVI and LST during 2006, 2016 and 2021

```
. regress lst2006 ndvi2006
```

Source	SS	df	MS	Number of obs	=	1,000
				F(1, 998)	=	449.69
Model	1950.43639	1	1950.43639	Prob > F	=	0.0000
Residual	4328.66327	998	4.33733795	R-squared	=	0.3106
				Adj R-squared	=	0.3099
Total	6279.09967	999	6.28538505	Root MSE	=	2.0826

lst2006	Coef.	Std. Err.	t	P>|t|	[95% Conf.	Interval]
ndvi2006	-12.82847	.6049516	-21.21	0.000	-14.0156	-11.64135
_cons	26.05517	.0667088	390.58	0.000	25.92426	26.18607

```
. regress lst2016 ndvi2016
```

Source	SS	df	MS	Number of obs	=	1,000
				F(1, 998)	=	437.67
Model	2008.06306	1	2008.06306	Prob > F	=	0.0000
Residual	4578.89657	998	4.58807272	R-squared	=	0.3049
				Adj R-squared	=	0.3042
Total	6586.95963	999	6.59355319	Root MSE	=	2.142

lst2016	Coef.	Std. Err.	t	P>|t|	[95% Conf.	Interval]
ndvi2016	-21.91827	1.04769	-20.92	0.000	-23.97419	-19.86234
_cons	29.87016	.1500697	199.04	0.000	29.57567	30.16465

```
. regress lst2021 ndvi2021
```

Source	SS	df	MS	Number of obs	=	1,000
				F(1, 998)	=	295.88
Model	1710.24355	1	1710.24355	Prob > F	=	0.0000
Residual	5768.69676	998	5.78025727	R-squared	=	0.2287
				Adj R-squared	=	0.2279
Total	7478.94031	999	7.48642673	Root MSE	=	2.4042

lst2021	Coef.	Std. Err.	t	P>|t|	[95% Conf.	Interval]
ndvi2021	-18.0857	1.051429	-17.20	0.000	-20.14897	-16.02244
_cons	30.71846	.1594107	192.70	0.000	30.40564	31.03127

Appendix 2: Regression analysis between NDBI and LST during 2006, 2016 and 2021

```
. regress lst12006 ndbi2006
```

Source	SS	df	MS	Number of obs	=	1,000
				F(1, 998)	=	484.68
Model	2176.92679	1	2176.92679	Prob > F	=	0.0000
Residual	4482.45178	998	4.49143465	R-squared	=	0.3269
				Adj R-squared	=	0.3262
Total	6659.37858	999	6.66604462	Root MSE	=	2.1193

lst12006	Coef.	Std. Err.	t	P>|t|	[95% Conf.	Interval]
ndbi2006	16.4408	.7467815	22.02	0.000	14.97536	17.90624
_cons	25.55703	.0681117	375.22	0.000	25.42338	25.69069

```
. regress lst12016 ndbi2016
```

Source	SS	df	MS	Number of obs	=	1,000
				F(1, 998)	=	655.98
Model	2508.92472	1	2508.92472	Prob > F	=	0.0000
Residual	3817.02115	998	3.82467049	R-squared	=	0.3966
				Adj R-squared	=	0.3960
Total	6325.94587	999	6.33227815	Root MSE	=	1.9557

lst12016	Coef.	Std. Err.	t	P>|t|	[95% Conf.	Interval]
ndbi2016	24.13078	.9421599	25.61	0.000	22.28194	25.97962
_cons	27.75827	.0651487	426.08	0.000	27.63042	27.88611

```
. regress lst12021 ndbi2021
```

Source	SS	df	MS	Number of obs	=	1,000
				F(1, 998)	=	391.34
Model	2106.62821	1	2106.62821	Prob > F	=	0.0000
Residual	5372.3121	998	5.38307825	R-squared	=	0.2817
				Adj R-squared	=	0.2810
Total	7478.94031	999	7.48642673	Root MSE	=	2.3201

lst12021	Coef.	Std. Err.	t	P>|t|	[95% Conf.	Interval]
ndbi2021	22.80542	1.152814	19.78	0.000	20.5432	25.06763
_cons	28.69309	.0759031	378.02	0.000	28.54414	28.84203

Appendix 3: Regression analysis between MNDWI and LST during 2006, 2016 and 2021

```
. regress lst22006 mndwi2006
```

Source	SS	df	MS	Number of obs	=	1,000
				F(1, 998)	=	76.79
Model	448.623176	1	448.623176	Prob > F	=	0.0000
Residual	5830.47649	998	5.84216081	R-squared	=	0.0714
				Adj R-squared	=	0.0705
Total	6279.09967	999	6.28538505	Root MSE	=	2.4171

lst22006	Coef.	Std. Err.	t	P>|t|	[95% Conf.	Interval]
mndwi2006	-9.864381	1.125682	-8.76	0.000	-12.07336	-7.655406
_cons	24.4239	.1777348	137.42	0.000	24.07513	24.77268

```
. regress lst22016 mndwi2016
```

Source	SS	df	MS	Number of obs	=	1,000
				F(1, 998)	=	93.77
Model	565.734157	1	565.734157	Prob > F	=	0.0000
Residual	6021.22548	998	6.03329206	R-squared	=	0.0859
				Adj R-squared	=	0.0850
Total	6586.95963	999	6.59355319	Root MSE	=	2.4563

lst22016	Coef.	Std. Err.	t	P>|t|	[95% Conf.	Interval]
mndwi2016	-14.33484	1.480348	-9.68	0.000	-17.23979	-11.42989
_cons	24.91545	.2355319	105.78	0.000	24.45325	25.37764

```
. regress lst22021 mndwi2021
```

Source	SS	df	MS	Number of obs	=	1,000
				F(1, 998)	=	62.46
Model	440.512374	1	440.512374	Prob > F	=	0.0000
Residual	7038.42793	998	7.052533	R-squared	=	0.0589
				Adj R-squared	=	0.0580
Total	7478.94031	999	7.48642673	Root MSE	=	2.6557

lst22021	Coef.	Std. Err.	t	P>|t|	[95% Conf.	Interval]
mndwi2021	-13.79635	1.745652	-7.90	0.000	-17.22191	-10.37078
_cons	26.32005	.2652281	99.24	0.000	25.79958	26.84052

Appendix 4: Regression analysis between Altitude and LST during 2006, 2016 and 2021.

```
. regress LST2006  DEM
```

Source	SS	df	MS	Number of obs	=	1,000
				F(1, 998)	=	189.48
Model	1685.08235	1	1685.08235	Prob > F	=	0.0000
Residual	8875.18499	998	8.89297093	R-squared	=	0.1596
				Adj R-squared	=	0.1587
Total	10560.2673	999	10.5708382	Root MSE	=	2.9821

LST2006	Coef.	Std. Err.	t	P>|t|	[95% Conf.	Interval]
DEM	-.006797	.0004938	-13.77	0.000	-.007766	-.0058281
_cons	41.62206	1.16235	35.81	0.000	39.34113	43.90299

```
. regress LST2016  DEM
```

Source	SS	df	MS	Number of obs	=	1,000
				F(1, 998)	=	287.00
Model	2425.00356	1	2425.00356	Prob > F	=	0.0000
Residual	8432.50745	998	8.44940626	R-squared	=	0.2233
				Adj R-squared	=	0.2226
Total	10857.511	999	10.8683794	Root MSE	=	2.9068

LST2016	Coef.	Std. Err.	t	P>|t|	[95% Conf.	Interval]
DEM	-.0081539	.0004813	-16.94	0.000	-.0090984	-.0072094
_cons	46.09363	1.132991	40.68	0.000	43.87031	48.31694

```
. regress LST2021  DEM
```

Source	SS	df	MS	Number of obs	=	1,000
				F(1, 998)	=	94.48
Model	1092.15679	1	1092.15679	Prob > F	=	0.0000
Residual	11536.3495	998	11.5594684	R-squared	=	0.0865
				Adj R-squared	=	0.0856
Total	12628.5063	999	12.6411474	Root MSE	=	3.3999

LST2021	Coef.	Std. Err.	t	P>|t|	[95% Conf.	Interval]
DEM	-.0054721	.000563	-9.72	0.000	-.0065768	-.0043674
_cons	40.85025	1.325203	30.83	0.000	38.24975	43.45075

Appendix 5: True color composite images of the study area A) SPOT 5 image during 2006, B) Sentinel-2A during 2016 and Sentinel-2A during 2021.

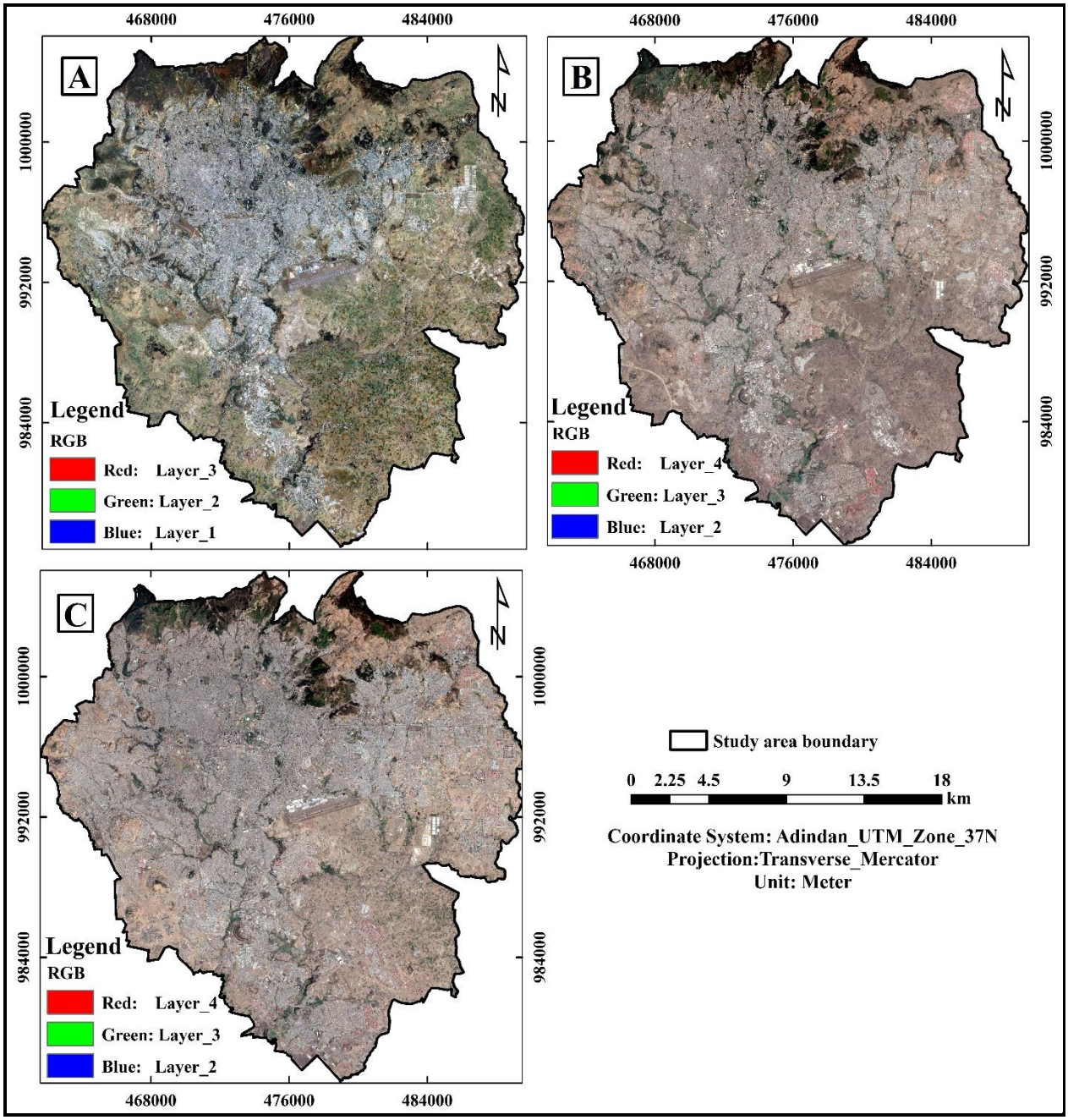

Appendix 6: A map showing conversion between LULC classes from 2006 to 2021

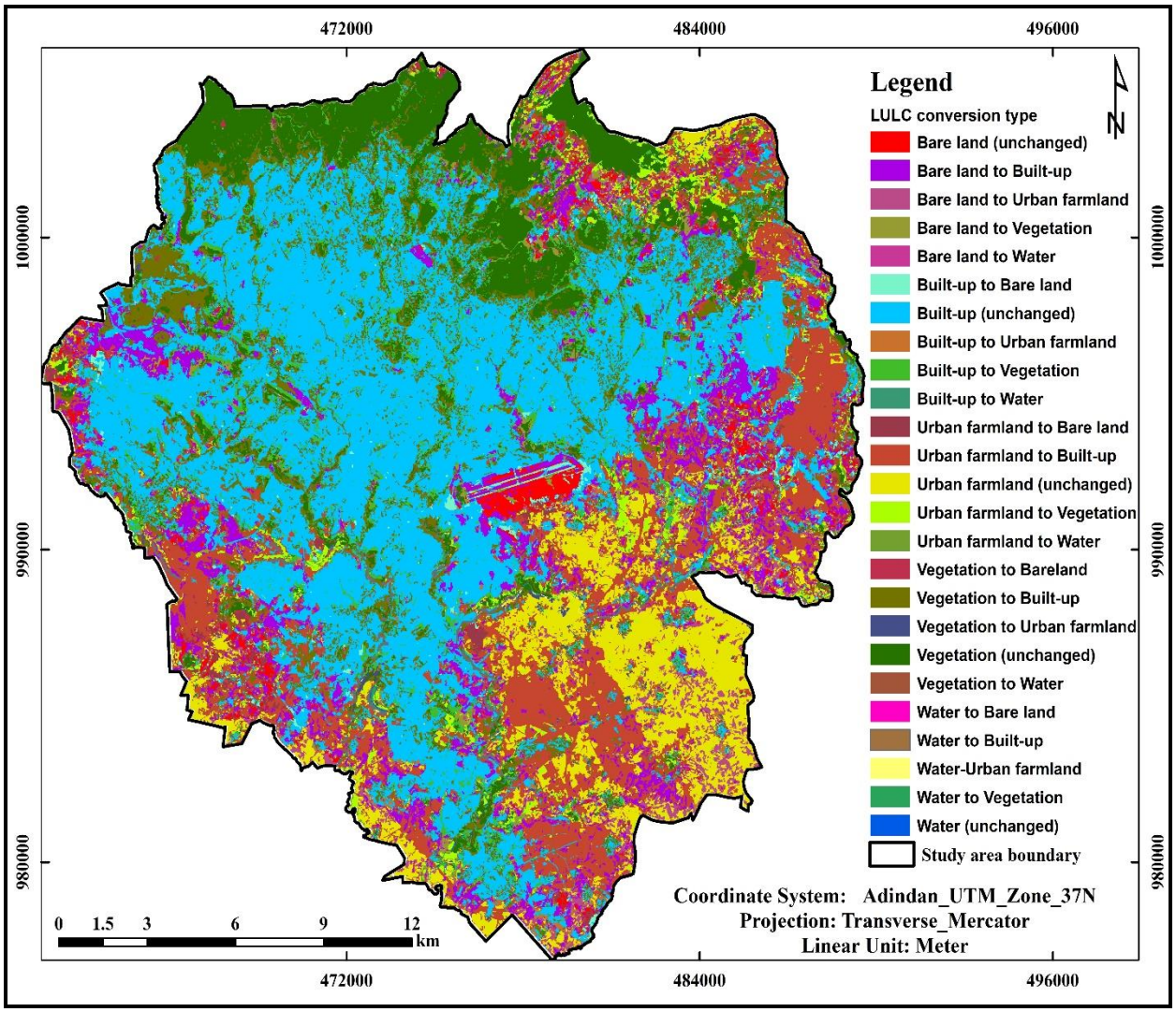

Appendix 7: Map of ground control points A) in 2006, B) in 2016 and C) in 2021